DEPARTAMENTO DE ASTROFÍSICA

Universidad de La Laguna

Understanding the outskirts of disc galaxies

Memoria que presenta
D. Alejandro Serrano Borlaff
para optar al grado de
Doctor por la Universidad de La Laguna.

INSTITUTO Đ ASTROFISICA Đ CANARIAS
octubre de 2018

Examination date: October, 2018
Thesis director: John E. Beckman and Mª del Carmen Eliche-Moral
Thesis tutor: Joan Font Serra

Dedicado a Ro,
Mamá, Papá, Saúl y Yuri

Summary

The outskirts of galaxies contain multiple clues about the formation processes that shaped galaxies into the current morphological scheme, and their evolution. Nevertheless, the analysis of the low surface brightness regions around galaxies is limited by the depth of our current imaging surveys and the presence of various types of systematic effects (i.e., projection effects, PSF contamination, sky over subtraction). In this PhD thesis we focus on the properties of the outskirts of disc galaxies, combining simulations, models and observations of disc galaxies with new methods and statistical tools to avoid systematic biases.

In the first part of this thesis (Borlaff et al. 2016) we focus on the effect of the increase of the disc scale-height of stellar discs as a function of the galactocentric radius on the surface brightness profiles of edge-on disc galaxies. This phenomenon (also named flaring) has been detected in the stellar discs of simulated and real galaxies, including the Milky Way. We use realistic 3D models based on observations to demonstrate that flares can create down-bending surface brightness profiles when observed at high inclinations. Contrarily, flares have no effect on the profiles of face-on galaxies, partially explaining the relatively high abundances of Type-II breaks in edge-on galaxies. Moreover, the distribution of inner-to-outer scale-length ratio of the resulting exponential profiles matches the observed distribution of breaks (Martín-Navarro et al. 2012), previously associated with radial star formation thresholds. In addition, we found that flares explain the weakening of the breaks with the vertical distance from the plane found by Pohlen et al. (2007) and Martinez-Lombilla et al. (2018).

In Borlaff et al. (2017, 2018) we analyse the properties of the Type-III (antitruncated) profiles of lenticular galaxies beyond the local Universe. We aim to study if the structural and photometric scaling relations found previously in Borlaff et al. (2014) in the Type-III S0 galaxies at $z = 0$ are compatible with a sample objects of the same type beyond the local Universe. In Borlaff et al. (2017) we identify a sample of red sequence galaxies from the GOODS-N field and classify them morphologically, according to their shape, surface brightness profile, and the star formation rate (SFR). Afterwards, we decompose and correct their images for PSF effects. Finally we identify 14 Type-III S0 galaxies between $0.2 < z < 0.6$. In a second paper (Borlaff et al. 2018), we analyse the structural and photometric properties of the identified sample, compared to the local Type-III S0 galaxies. We found that the general structure of Type-III S0 galaxies does not present a significant change, although they do show a general dimming of $\Delta\mu \sim 1.5$ mag arcsec^{-2} since $z \sim 0.6$. We compare the results to a grid of Single Stellar Population (SSP) models, in order to obtain an estimate of the age of the dominant stellar population. We find that if the star formation history (SFH) if similar to that of an SSP, this cannot have happened earlier than $z \sim 1.2$. Otherwise, the SFH has to be more extended in time or present multiple SFR bursts.

The last chapter of the PhD is focused on the near infrared (NIR) observations of the *Hubble Ultra Deep Survey* (HUDF). In order to continue the analysis of the outskirts of disc galaxies to higher z, NIR observations become mandatory. Nevertheless, the limiting

surface brightness of most ground and space-based surveys is dominated by systematic effects, rather than the signal-to-noise ratio. Sky over-subtraction, PSF contamination, NIR persistence, and flat field residuals generate irreversible biases on the final combined mosaics and the science products. Mitigation of these effects requires a careful and robust treatment of the science exposures. For instance, it has been shown that the low surface brightness structure around the galaxies of the WFC3/IR HUDF (see XDF, Illingworth et al. 2013; HUDF12, Koekemoer et al. 2013) was significantly removed by the reduction process because of background over-substraction. In a recent paper (Borlaff et al. submitted)[1] we test a number of techniques to improve the reduction pipeline of the WFC3/IR HUDF. These methods include the creation of sky flat fields, correction of NIR persistence, residual background removal, careful sky level matching and robust co-adding. As a result, we successfully recover the removed structure in the outskirts of galaxies, increasing the depth of the images by reducing the systematic biases. We obtained a new version of the WFC3/IR HUDF mosaics which preserves the properties of the objects at all angular scales and intensity ranges, valid for the study of the low surface brightness Universe.

[1]The ABYSS HST Ultra Deep Imaging Project: http://www.iac.es/proyecto/abyss/

Resumen

Las regiones externas de las galaxias contienen múltiples pistas sobre los procesos de formación que dieron lugar a los distintos tipos morfológicos observados en la actualidad y su evolución. Sin embargo, el análisis del Universo a bajo brillo superficial esta limitado por la profundidad de las imágenes actuales y la presencia de diversos tipos de efectos sistemáticos; efectos de proyección, contaminación por función de dispersión de punto (PSF), sobre-substracción de nivel de cielo, entre otros. En esta tesis doctoral nos centramos en el estudio de las propiedades de las partes externas de las galaxias de disco, combinando simulaciones, modelos y observaciones con nuevos métodos y herramientas estadísticas para evitar efectos sistemáticos.

En la primera parte de esta tesis (Borlaff et al. 2016) nos centramos en el efecto del incremento de la escala vertical de disco como función del radio galáctico sobre los perfiles de brillo superficial de galaxias de canto. Este fenómeno (llamado *flaring*) ha sido detectado en el disco estelar de simulaciones de galaxias y en galaxias reales, incluyendo la propia Vía Láctea. Mediante el uso de modelos de galaxias 3D realistas basados en observaciones, demostramos que los *flares* pueden producir truncamientos en los perfiles de brillo superficial de galaxias con muy alta inclinación. Por otro lado, los *flares* no producen ningún efecto en galaxias a baja inclinación, lo cual explica parcialmente la relativa alta frecuencia de detección de truncamientos en galaxias de canto. Además, nuestros modelos reproducen la distribución del cociente entre la escala de disco interna y externa al truncamiento (Martín-Navarro et al. 2012), previamente asociada a una caída brusca en la tasa de formación estelar. Finalmente, observamos que los *flares* explican la caída en la intensidad de los truncamientos a mayores distancias del plano galáctico observada por Pohlen et al. (2007) y Martinez-Lombilla et al. (2018).

En Borlaff et al. (2017, 2018) analizamos las propiedades de los discos antitruncados de galaxias lenticulares a distancias cosmológicas. El objetivo es comprobar si las relaciones de escala en estructura y fotometría descubiertas previamente en Borlaff et al. (2014) en galaxias lenticulares con perfil Tipo III a $z = 0$ son compatibles con una muestra de objetos del mismo tipo fuera del Universo local. En Borlaff et al. (2017) identificamos una muestra de galaxias de la secuencia roja en el campo cosmológico GOODS-N, clasificándolas morfológicamente por su forma aparente, perfil de brillo superficial y la tasa de formación estelar (SFR). Después, descomponemos y corregimos las imágenes de efectos de PSF. Generamos perfiles de brillo superficial y los clasificamos en los distintos subtipos mediante el uso de herramientas estadísticamente robustas desarrolladas por nosotros con este objetivo. Finalmente identificamos 14 galaxias S0 con perfiles Tipo III a $0.2 < z < 0.6$.

En el segundo artículo de la serie (Borlaff et al. 2018), analizamos las propiedades estructurales y fotométricas de los discos antitruncados de esta muestra, comparándolas con una muestra de objetos del mismo tipo en el Universo local. Los resultados muestran que la estructura general de los discos antitruncados en galaxias lenticulares no ha cambiado significativamente desde $0.4 < z < 0.6$, aunque su brillo en la banda R ha disminuido en $\Delta\mu \sim 1.5$ mag arcsec^{-2} desde $z \sim 0.6$. Comparamos los resultados con

una red de evolución de modelos de población estelar única (SSP) con el objetivo de obtener una estimación sobre la época de formación de la población estelar dominante en las galaxias S0 Tipo III. Los modelos muestran que, si la historia de formación estelar (SFH) de las S0 Tipo III puede aproximarse como un único brote de población estelar, este brote tuvo que tener lugar a $z < 1.2$. En cualquier otro caso, la SFH debe ser más extendida en el tiempo o presentar diversos brotes de formación estelar.

El último capítulo de la tesis esta dedicado a las observaciones en infrarrojo cercano (NIR) del *Campo Ultra Profundo de Hubble* (HUDF). Para continuar el análisis de las partes externas de galaxias de disco hacia rangos mayores de desplazamiento al rojo son necesarias observaciones en el rango espectroscópico del NIR. Sin embargo, el limite de brillo superficial de la mayor parte de las exploraciones desde telescopios en tierra o espaciales esta dominada por efectos sistemáticos, en lugar del cociente de señal a ruido. Los efectos de sobre-sustracción de cielo, contaminación de PSF, persistencia en el NIR y residuos de corrección de campo plano generan desviaciones irreversibles en los mosaicos finales y por lo tanto en los resultados científicos. Mitigar estos efectos requiere un tratamiento cuidadoso y robusto de las exposiciones individuales. Se ha observado que la estructura de bajo brillo superficial de los mosaicos de HUDF obtenidos usando la cámara WFC3/IR del *Hubble Space Telescope* (ver XDF, Illingworth et al. 2013; HUDF12, Koekemoer et al. 2013) fue significativamente sobre sustraída durante el proceso de reducción de los datos. En Borlaff et al. (submitted)[2] probamos una serie de técnicas para mejorar el proceso de reducción de datos de WFC3/IR en el HUDF. Estos métodos incluyen auto-calibración de campo plano, corrección de persistencia, corrección de gradientes residuales y ajuste del nivel de cielo relativo de las exposiciones, así como combinación robusta de las imágenes. Como resultado de estas mejoras, recuperamos la estructura externa de las galaxias presentes en los mosaicos, aumentando la profundidad de las imágenes debido a la reducción de los efectos sistemáticos. La nueva versión de los mosaicos NIR del HUDF preserva mejor las propiedades de los objetos a todas las escalas angulares y de intensidad, permitiendo de esta manera el estudio del Universo a bajo brillo superficial mediante todas las técnicas actuales y propuestas.

[2]El proyecto ABYSS de imagen ultra-profunda con HST: http://www.iac.es/proyecto/abyss/

Contents

List of figures not included in articles

1

From the exponential disc to the outer haloes.

Из опыта моей жизни:
Если хочешь, чтобы самое маленькое дело было
решено успешно - приложи к этому самое
большое усилие!

From my life experience:
If you want the smallest thing to be solved
successfully, make the greatest effort!
— Alexei Leonov - USSR Cosmonaut.
Dedicated to the IAC on the visitors book during
Starmus 2016.

1.1 Disc galaxies on the Hubble sequence

Once we overpass the surface brightness of the darkest night sky ($\mu = 22$ mag arcsec^{-2}) we are able to detect a reasonable fraction of the structure of the galaxies that surround us. The number and variety of galaxies rapidly increases with the apparent size and luminosity. Galaxies present a large diversity of shapes and properties. Based on Hubble (1922), the Hubble Sequence (Hubble 1926) was the first attempt to classify them based on its apparent shape and structural complexity. Although it was later revised by de Vaucouleurs (1959a) and Sandage (1961), it is still one of the fundamental pillars of astronomy (see in Fig. 1.1 the original diagram published in Hubble 1936).

In an early general view, galaxies were divided into several classes:

1. Elliptical galaxies, with spheroidal shapes and generally an axisymmetric smooth light distribution without any visible disc or spiral substructure. They are classified from 1 to 7 by its increasing ellipticity[1] e.

2. Spiral galaxies, with a disc structure and a noticeable spiral pattern, usually populated with blue knots of active star formation. They are divided into two parallel branches, barred and non-barred, with three sub-types (a, b and c) depending on the tightness of the spiral pattern and the brightness of its bulge component.

3. Irregular galaxies. This class includes all the objects without clear shapes or patterns that do not match into any other classes.

It is not until Spitzer & Baade (1951) that the lenticular galaxies or S0s were identified as the hypothetical intermediate class of galaxies between the elliptical and the spiral galaxies theorised by Hubble (1926, 1936). Lenticular galaxies present clear smooth disc structure, sometimes with dust lanes (Annibali et al. 2010; Finkelman et al. 2010) but they do not show any signs of spiral pattern and present very low star formation rates (SFR). Although later studies have proved that galaxies do evolve between types along the Hubble diagram, it is worth noting that many authors have incorrectly claimed that this proposed classification system was supposed to imply an evolutionary path or direction, despite the explicit note in Hubble (1927)[2].

The colours and spectral properties present a continuous variation along the Hubble Sequence (Holmberg 1958; de Vaucouleurs 1959a, 1963) suggesting that this early morphological classification is deeply linked to the real formation and evolution of galaxies. In fact, elliptical galaxies tend to be red, massive and they show little or low SFR, while the spirals are less massive, bluer and present higher SFR. Due to their usual smooth structure, lenticular galaxies are difficult to classify using only photometric information (Bernardi et al. 2010), as they are easily confused with elliptical galaxies when in face-on orientations (Emsellem et al. 2007; Cappellari et al. 2011; Krajnović et al. 2011). It is for these reasons that new classification schemes have been proposed where lenticular form a parallel sequence to that of the spirals (van den Bergh 1976). Some authors (King 1992; Djorgovski 1992) announced the need for more physically motivated alternatives to the Hubble sequence, a claim that was addressed by more recent studies, taking into account the internal dynamics of the galaxies (Emsellem et al. 2007; Cappellari et al. 2011; Laurikainen et al. 2010; Kormendy & Bender 2012). These studies have shown that the slow rotators are morphologically assigned to a mix of E and S0 galaxies. Lenticular and spiral galaxies enclose all classes of disc galaxies (with the exception of dwarfs, which we will not address in this work). In this PhD thesis we will focus on the properties of the outskirts of disc galaxies, paying special attention to the lenticular galaxies.

[1] The number corresponds to the first decimal of $e = 1 - b/a$ where a and b are the minor and the major axis

[2] In Hubble (1927), the author noted: *"This nomenclature, it is emphasised, refers to the position in the sequence, and temporal connotations are made at one's peril. The entire classification is purely empirical and without prejudice to theories of evolution"* (see Baldry 2008, for a detailed discussion about this).

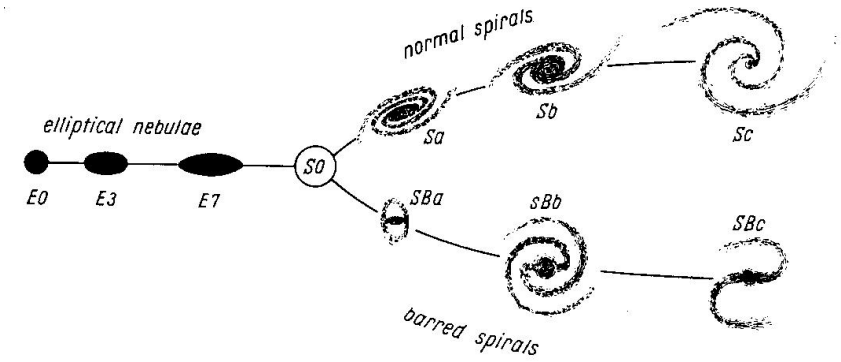

Figure 1.1: Hubble's original tuning-fork diagram as published in 1936 in The Realm of the Nebulae (Hubble 1936). From left to right: elliptical galaxies (E), lenticulars (S0), and spirals (S). The top branch of spirals represent the sequence of bar-less (normal) spiral galaxies and the bottom, its parallel sequence of barred spirals.

1.2 Evolution of disc galaxies: spirals and lenticulars

Motivated by their disc structure, there have been multiple studies looking for evolutionary connections between the spiral and S0 galaxies. It has been observed that the number density of S0 galaxies has increased since $z \sim 1$, at the expense of spiral galaxies (Dressler 1980; Dressler et al. 1997; Poggianti et al. 2009; D'Onofrio et al. 2015). This effect has been observed in clusters and groups. As a consequence, S0s have become numerically dominant at the characteristic L^* of the luminosity function ($L \sim L^*$, Schechter 1976) in the local Universe over other morphological types in both environments (Marzke et al. 1994; Bernardi et al. 2010). It is then clear that a significant fraction of S0s were spirals in the past, although the mechanisms that drive this evolution are still a matter of debate. Their morphological transformation had to take place either through internal processes which removed the gas, the spiral structure and quenched the star formation in their discs, or through interactions with other galaxies. It has been generally thought that disc galaxies are too fragile to survive or reconstruct their structure after a merger (Toth & Ostriker 1992; Kormendy & Kennicutt 2004). In that scenario, spiral galaxies would have been transformed into S0s after their star formation was cut-off (Aragón-Salamanca et al. 2006), either through gas stripping in the disc (Gunn & Gott 1972; Bekki et al. 2002; Laurikainen et al. 2010), removal of their gas halo reservoirs (starvation or strangulation, Larson et al. 1980), harassment (Moore et al. 1996), or strong and sustained star formation in the central regions of the galaxies (Kormendy & Kennicutt 2004).

Pseudobulges present relatively flat shapes and with a significant degree of rotational support (Kormendy 1993; Laurikainen et al. 2006; Graham 2013), contrary to the classical spheroidal kinematically-hot bulges. Their presence in S0 galaxies is often considered as a proof of their secular origin (Laurikainen et al. 2010; Vaghmare et al. 2015), because it is considered difficult to explain the properties of such structures after violent processes such as major mergers. Some studies claim that structures related to minor and major mergers such as shells, ripples (Malin & Carter 1980) and polar rings (Schweizer et al. 1983) appear in S0 galaxies, although they are not very common (in Sect. 1.5 we will demonstrate that current measurements of the relative frequency of such structures may be strongly biased due to the limiting depth of the images). Similar arguments have been applied to other structures such as lenses (Laurikainen et al. 2011). Despite this, alternative simulation studies based on minor and major merger processes have been proposed to create pseudobulges and lenses (Eliche-Moral et al. 2012, 2013; Querejeta et al. 2015a; Eliche-Moral et al. 2018). In addition, there are observations of galaxies which contain both classical and pseudobulges (Erwin et al. 2015), proving that structures associated with very different formation mechanisms can coexist in the same galaxy.

The processes behind the transformation of spiral galaxies to lenticulars that are related to the environment of the galaxies may only play a significant role in the formation of intermediate-to-low mass S0 galaxies (Ravikumar et al. 2006; Bernardi et al. 2011a,b; Barway et al. 2013; Cerulo et al. 2017) located in clusters (Vollmer et al. 2005, 2012; Crowl et al. 2005; Rodríguez Del Pino et al. 2014). In fact, some authors suggest that this transformation may be more efficient in low density clusters than in high density ones (Fasano et al. 2000). Nevertheless, half of the S0 galaxies reside in groups or on the field, with very few cases of isolated S0s (Huchra & Geller 1982; Berlind et al. 2006; Crook et al. 2007; Wilman et al. 2009; Khim et al. 2015).

Contrary to widespread belief, many studies prove that major mergers can produce well-defined disc remnants (Bekki & Kenji 1998, 2001; Bekki & Couch 2011; Bournaud et al. 2005, 2007; Bournaud et al. 2011; Governato et al. 2007, 2009; Hopkins et al. 2009a,b; Hopkins et al. 2013; Eliche-Moral et al. 2018) or even spiral galaxies (Athanassoula et al. 2016; Rodionov et al. 2017; Peschken et al. 2017). In fact, bulge/disc decompositions of the lenticular galaxies by Barway et al. (2009) suggest that the low-luminosity lenticulars were formed by secular evolution processes, while the bright (more massive) lenticulars may have been formed through major merger processes. Thus, lenticular galaxies may approach their morphology from different initial states by moving along multiple evolutionary paths (van den Bergh 1990). Many questions arise from these studies: how can processes of such different nature end up creating systems of similar apparent morphology as the lenticular galaxies? How stable – from the evolutionary point of view – are the structures of the galactic discs? Are there significant differences between the structure of stellar discs at different redshifts?

1.3 The surface brightness profiles of galaxy discs

1.3.1 Type I or pure exponential discs

One of the first surface brightness profile analysis was published by Reynolds (1913). This author found a rapid decrease of the surface luminosity of M31 as a function of radius (see Fig. 1.2), which was associated with the interaction of the light from a hypothetical inner central star with the surrounding nebulous material of the spiral. Reynolds also discussed the alternative hypothesis that M31 could actually be a distant galaxy made of stars, arguing that in that case, it would be very improbable that the composed surface brightness profile of the stars would follow the observed curve. The discovery of Cepheids in M31 and M33 a decade later by Hubble (1925) proved that such possibility was in fact correct.

Later on, Patterson (1940) determined that the luminosity distribution along the galactocentric radius of M33 was nearly exponential. This result was later confirmed by de Vaucouleurs (1959b) using photometric data in three optical bands (U, B and V). Sérsic (1963) pointed out that the variation of the surface brightness is a consequence of the stellar density decline as a function of galactocentric radius. Since then, an increasing number of observational studies confirmed the exponential nature of the galactic discs using larger samples of galaxies (Freeman 1970; Kent 1984; de Jong 1996). The shape of the surface brightness profile of a galaxy is a proxy of its surface mass density and thus its study is extremely useful for the analysis of the gravitational potential of galaxies. Freeman (1970) compared HI rotation curves with the predicted rotation curves from the observed optical exponential discs of NGC300 and M33, concluding that there should be an unknown amount of undetected additional matter – as large as the mass of the detected galaxy – with a very different distribution from the observed exponential disc. This was one of the first suggestions[3] of the presence of dark matter in galaxies, tightly linked to the structure of the exponential disc.

Despite the observational limits, all exponential discs profiles must present some type of deviation from their trend at some radius. Either a truncation (see Sect. 1.3.2) or a transition to a external component (i.e, the stellar halo). Nevertheless, even using the current observational capabilities, some objects present very extended light profiles that do not seem to end, maintaining a single exponential disc down to very low-surface brightness limits ($\mu = 30$ mag arcsec^{-2}) and large radius ($\sim 9 - 10$ scale-lengths). Examples of such objects are NGC5383 (Barton & Thompson 1997), NGC4123 (Weiner et al. 2000), or NGC300 and NGC7793, analysed by Bland-Hawthorn et al. (2005) and Vlajić et al. (2009, 2011) using star count methods.

[3] Oort (1940) already observed discrepancies between the structure and dynamics of NGC3115: *"It may be concluded that the distribution of mass in the system must be considerably different from the distribution of light. [..] The most remarkable feature is that the mass density appears to remain practically constant outside $a = 10$", though the light-intensity falls off steeply. The strongly condensed luminous system appears embedded in a large more or less homogeneous mass of great density."*

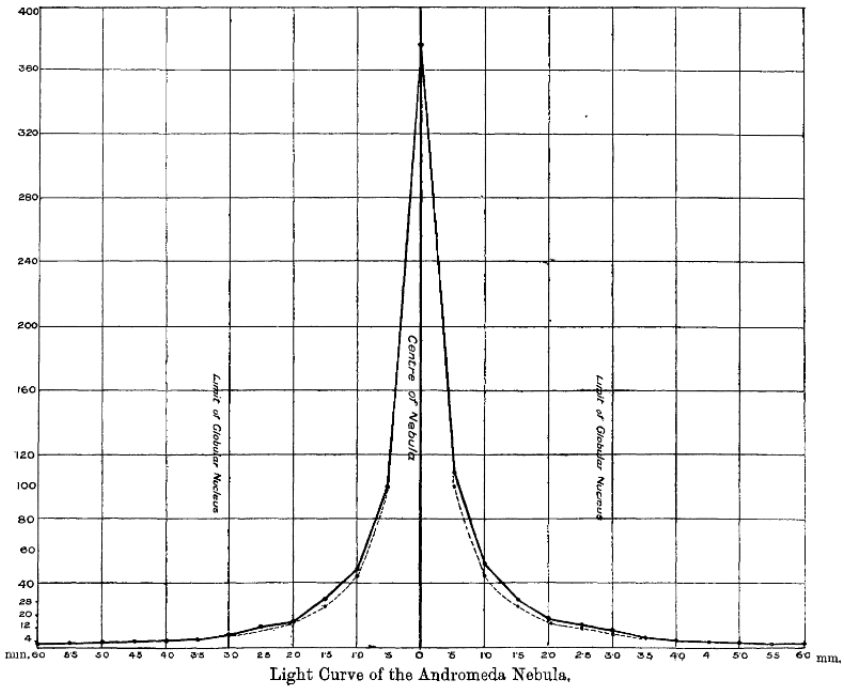

Light Curve of the Andromeda Nebula.

Figure 1.2: M31 original surface brightness profile reproduced from The light curve of the Andromeda nebula (NGC 224) by Reynolds (1913). In the vertical axis, light intensity (arbitrary units). The horizontal axis represents the spatial dimension (in mm, where 1 mm = 69"). Solid line represents the observed values, while the dotted line represents a fitted law $(x + I)^2 y = C$, where x is the radius, y is the intensity and I and C are constants.

The mechanisms for the formation of such exponential profiles that extend out to $\sim 9-10$ scale-lengths are still unknown. Early models (Mestel 1963; Gunn 1982) show that exponential profiles could be generated by the collapse of a uniformly rotating gas sphere. Nevertheless, these authors found also that the resulting disc is only exponential over ~ 3 scale-lengths, which can partially explain down-bending profiles (see Sect. 1.3.2), but such models cannot explain the presence of exponential discs that extend for almost 10 scale-lengths. Moreover, Efstathiou (2000) showed that in order to reproduce exponential profiles for so many scale-lengths through angular momentum conserving collapse, the initial halo should present an abrupt, and physically implausible, upturn of the rotation curve at some radius. In addition to the collapsing halo models, Hohl (1971) proposed

that bars and spiral instabilities could form exponential profiles through scattering. Other models suggest that exponential profiles appear when the viscous flow rate of the gas equals the star formation rate (Lin & Pringle 1987; Yoshii & Sommer-Larsen 1989; Ferguson & Clarke 2001).

Nevertheless, not all galaxies with exponential discs present spiral arms, bars or bulge-like remnants of dissipated bars that could have scattered the stars. In addition, such models cannot explain the prevalence of exponential discs in dwarf galaxies, which do not suffer from shear or present obvious spirals or bars (Hunter et al. 2011). Finally, it is not clear that the exponential profile can be reconstructed after interactions in a reasonable time-scale (Struck & Elmegreen 2017). More recently Elmegreen & Struck (2013, 2016) found that orbiting or transient stellar scattering cores (such as clumps, holes or transient dark matter halos) can form exponential profiles in two dimensional simulations with a fixed halo potential if there is an slight inward bias in the scattering direction probability. Such scattering in simulations of dwarf irregular galaxy discs produce exponential surface density profiles in the stellar population from an initial uniform distribution in ~ 1 Gyr (Struck & Elmegreen 2017). Despite the number of models proposed, the exact mechanism or mechanisms that form exponential discs and the reason for this profile is still a problem to be solved.

1.3.2 Type II: breaks and truncations

Nevertheless, not all galaxies present pure exponential profiles along their observable radius. In Freeman (1970), the author identified two different types of discs according to their surface brightness profiles. The first type of profiles were well modelled with a single exponential for the whole detectable radius. The second type presented a surface brightness deficit in the outer parts of the disc with respect to the extrapolated trend of the inner regions. It was later observed by van der Kruit (1979) and van der Kruit & Searle (1981a,b), that the profiles of some edge-on galaxies apparently showed sudden cut-offs of their surface brightness profiles in the form of a sharp end or "truncation". As mentioned in Sect. 1.3.1, Mestel (1963) proposed gravitational collapse of a uniformly rotating, constant-density gas sphere as a possible explanation for the formation mechanism of the exponential galactic discs. Interestingly, the surface density profiles of collapsing models with initial halo density distributions produce compatible results, creating truncated profiles with break radius at $\sim 2-4h$, where h is the scale-length of the inner disc, similar to the observations (Gunn 1982; van der Kruit 1987; Dalcanton et al. 1996; Bullock et al. 2000). The observational prevalence and ubiquity of the truncated profiles was in apparent agreement with the cosmological point of view that the main formation mechanism of disc galaxies was the collapse of a rotating gas halo with a certain amount of angular momentum, which defined the break radius.

Later studies of face-on galaxies by Naeslund & Joersaeter (1997), Byun (1998), de Grijs et al. (2001), and Pohlen et al. (2002) pointed out that the down-bending breaks were not as sharp as those found by van der Kruit (1987) in edge-on galaxies, finding a steeper but noticeable outer profile beyond the truncation. As an alternative to the halo collapsing models, Kennicutt et al. (1989) suggested that truncations could be explained

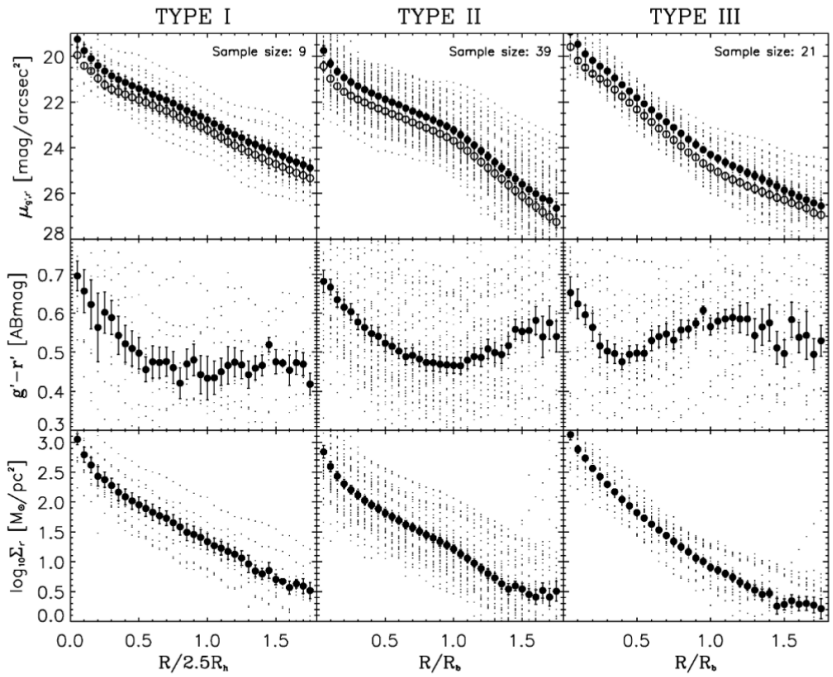

Figure 1.3: *Top row:* mean scaled surface brightness profiles of 9 Type-I (left column), 39 Type-II (central column) and 21 Type-III (right column) spiral galaxies in the SDSS r-band (filled circles) and g-band (open circles). Small dots represent the individual profiles. *Central row:* SDSS $g-r$ mean colour profiles. *Bottom row:* surface stellar mass profiles calculated using the colour-to-M/L conversion from Bell et al. (2003). Taken from Bakos et al. (2008)

if there is a critical limit on the gas surface density, so that beyond which the star formation could not occur. Moreover, Battaner et al. (2002) proposed that if large scale galactic magnetic fields created significant forces over the ionised gas component (Nelson 1988; Battaner et al. 1992a,b) and if those were in equilibrium with the gravitational and centrifugal forces, the magnetic forces would be suppressed after the interstellar gas is transformed into stars. Stars beyond a certain radius would then escape, creating a deficit of stars that could explain the truncation.

It has been observed that the Type-II galaxies present U-shaped colour profiles, following a bluening with the galactocentric radius and a turn-over beyond the break (Azzollini et al. 2008a; Bakos et al. 2008). This suggests a minimum age of the stellar population at the break radius and redder colours at the outer disc. This result is compatible with the observations from Radburn-Smith et al. (2012), who found that beyond the break radius, the profile is steeper for younger populations. Bakos et al. (2008) also found that the down-bending surface brightness profiles present nearly exponential surface mass density profiles, showing less signs of the Type-II break in the stellar mass profile than in the surface brightness profile (see Fig. 1.3). These results strongly contrast with the halo collapsing models, which can partially explain the observed down-bending profiles, but they cannot reproduce the presence of an outer steeper exponential disc made of old stars beyond the break radius (Naeslund & Joersaeter 1997; Byun 1998). Roškar et al. (2008a,b) associated this feature with increasing levels of SFR (stimulated by the bar or the spiral arm structure) with the galactocentric radius combined with scattering of old stars towards larger radii, beyond the break radius. This is partially supported by observations with the Hubble Space Telescope (HST) on deep cosmological fields which revealed that the break radius of Type-II discs has increased by a factor of 1.3 ± 0.1 since $z \sim 1$ (Perez 2004; Azzollini et al. 2008a), suggesting a moderate inside-out growth formation of discs (Thilker et al. 2004; de Paz et al. 2005; Muñoz-Mateos et al. 2006; Thilker et al. 2007).

Some authors found that the break occurs at the same radius regardless of the age of the stellar population and the height above the disc, being sharpest in the midplane and nearly disappearing at large heights (de Jong et al. 2007). This result was also found by Pohlen et al. (2007), measuring a significant weakening of the breaks with increasing distance from the plane for both inner and outer profiles. Based on the galactocentric radius and the change of slope of the profile, Martín-Navarro et al. (2012) revised the definitions for breaks and truncations, identifying them as physically different features. They associate the former (less strong and typically at lower galactocentric radius) with star formation thresholds and the latter (sharper and at higher galactocentric radius) with the maximum angular momentum of the galaxy, measured through the maximum rotation velocity according to previous models (Mestel 1963; Gunn 1982; van der Kruit 1987; Dalcanton et al. 1996; Bullock et al. 2000). In a recent paper, Martinez-Lombilla et al. (2018) used the U-shape NIR$-r$ colour profile and the vertical distribution of the truncations to measure an upper limit for the growth rate of two Milky Way-like galaxies, NGC4565 and NGC5907. These observations point to a combination of star formation thresholds and radial migration as the origin of a certain fraction of Type-II profiles. In Chapter 2 of this thesis we also analyse if some of the breaks in edge-on disc galaxies can be caused by the combination of flares (increase of the scale-height of the stellar disc with the galactocentric radius) with the projection effects at high inclinations (published in Borlaff et al. 2016).

1.3.3 Type III: antitruncations

For some time it was taken for granted that all galaxies had down-bending breaks at their edges (see Pohlen et al. 2004, for a review on the topic), until Erwin et al. (2005) presented a sample of spiral and lenticular galaxies with the opposite behaviour. They called them "antitruncations". The surface brightness profiles of these objects present exponential profiles that become shallower beyond a certain radius, showing an excess of light above the outward projection of the inner exponential profile. Following this work, Pohlen & Trujillo (2006) and Erwin et al. (2008) revised the stellar disc classification of galaxies expanding the one presented by Freeman (1970) and classified the galaxies into three main types according to the shape of their surface brightness profile (see Fig. 1.4):

1. Type-I disc galaxies (or pure exponentials) present profiles that are well modelled with a single exponential profile, up to the their observable radius.

2. Type-II galaxies present a down-bending profile, that is, the profile of the disc steepens sharply beyond a certain radius with respect to the extrapolated trend of the inner regions. This type includes the breaks and truncations, as previously commented.

3. Type-III or antitruncated surface brightness profiles. These profiles present an up-bending shape, becoming shallower outside the break radius.

Erwin et al. (2005) found two different sub-types of antitruncations, those that maintain the ellipticity of their isophotes beyond the break radius ("d", standing for disc) and those which present a gradual transition towards rounder isophotes ("s", standing for spheroidal). While the former ones are associated to outer exponential discs, the latter suggest that the inner disc is embedded into an spheroidal component such as the outer extent of the bulge or a separate stellar halo. The authors found that most Type-III profiles ($\sim 70\%$) are associated with an outer disc component, which sometimes show spiral arms. Maltby et al. (2012) found a similar fraction ($\sim 85\%$) of Type-III "d" profiles, concluding that the extrapolation of the bulge component is insufficient to explain the excess of light in the outer regions in most cases, in favour of an external disc origin.

Many models have been proposed to explain the Type-III profiles. Most of them can be classified into three different classes according to their main driving mechanism: 1) star-formation, 2) secular radial migration, and 3) gravitational interactions. Elmegreen et al. (2005) proposed radial variation of the SFR as a cause for different types of surface brightness profiles. Nevertheless, it has been observed that Type-III profiles are not associated with a change in colour, and they do appear in the surface mass density profiles (Bakos et al. 2008; Azzollini et al. 2008a; Zheng et al. 2014), in partial contradiction to the observations of galaxies with Type-II profiles. In addition, Erwin et al. (2012) found a significant lack of Type-II profiles in the lenticular galaxies of the Virgo Cluster, whereas Type-III seemed independent of the local density (see also Pranger et al. 2017, for a less significant but similar result).

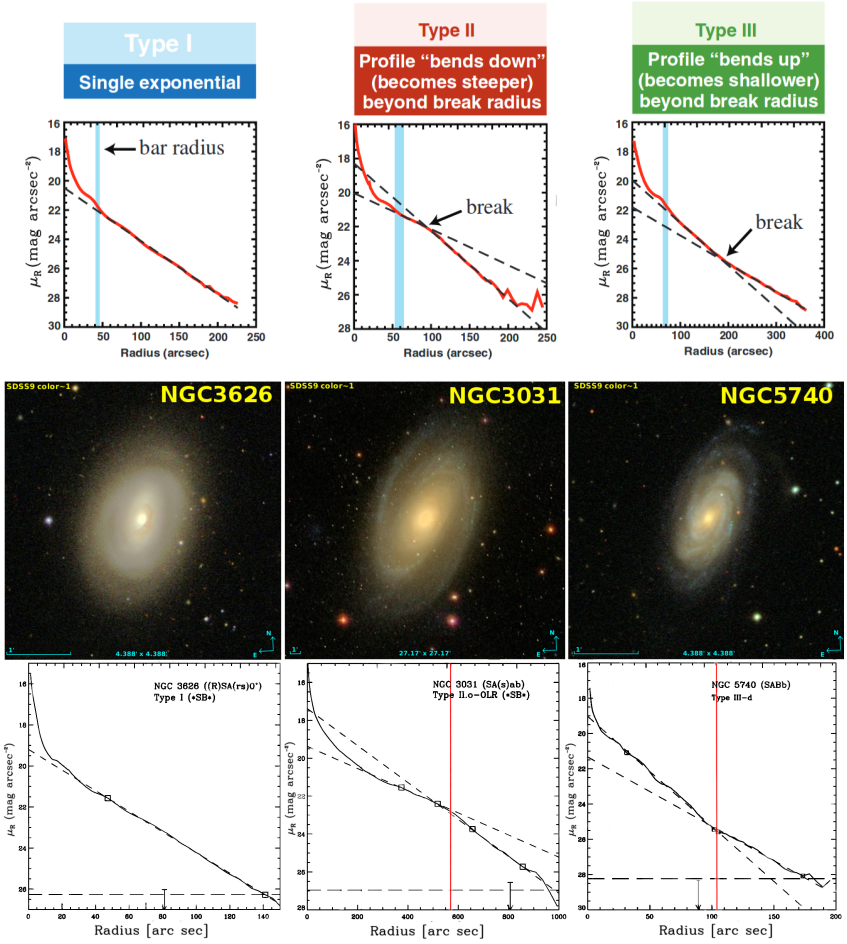

Figure 1.4: Examples of disc profiles. *Columns from left to right:* Type I (exponential profile, NGC3626), Type II (down-bending profile, NGC3031), Type III (antitrucated profile, NGC5740). *Top row:* Break classification scheme, from Erwin et al. (2008). *Central row:* SDSS DR9 RGB colour images (using the SDSS *gri* filters, Ahn et al. 2012) of NGC3626, NGC3031, and NGC5740. *Bottom row: R*-band surface brightness profiles of NGC3626, NGC3031, and NGC5740, as obtained by Erwin et al. (2008, NGC5740) and Gutierrez et al. (2011, NGC3626 and NGC3031). Diagonal dashed lines represent the fits for the inner and outer profiles. Vertical solid red lines represents the break radius for the Type-II and Type-III profiles. The dashed horizontal line represents the limiting magnitude for the surface brightness profile in each case. Figures taken from Erwin et al. (2008) and Gutierrez et al. (2011).

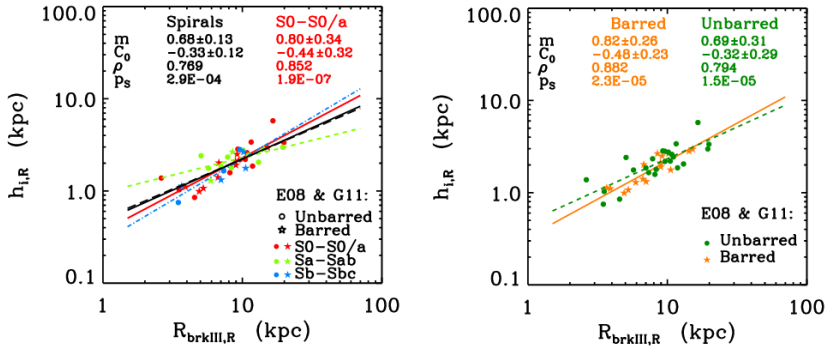

Figure 1.5: Distribution of the scale-length of the inner disc ($h_{\rm i}$) as a function of the break radius ($R_{\rm break}$) of galaxies with Type-III R-band surface brightness profiles from Erwin et al. (2008) and Gutierrez et al. (2011). *Left panel:* Comparison for different morphological types (red thick solid line: S0–S0/a, grey thin solid line: all spirals, green dashed line: Sa-Sab, blue dash-dotted line: Sb–Sbc). *Right panel:* Comparison of the trends for barred (orange solid line) and unbarred (green dashed line). The results of the linear fits performed are indicated at the top of each panel. See the legend on each plot. Reproduced from Eliche-Moral et al. (2015).

These results suggest that: 1) antitruncated profiles are not caused by star formation or different stellar population profiles, and 2) Type-II and Type-III profiles are probably caused by totally independent phenomena.

The increase of the stellar disc velocity dispersion due to the effects of in-plane, smooth gas accretion has been proved to be a viable mechanism to produce Type-III profiles on simulations (Minchev et al. 2012). Some authors argue that bars could scatter stars to the outskirts of the galaxies (Brunetti et al. 2011), creating the up-bending profiles (Ruiz-Lara et al. 2017; Herpich et al. 2017). This effect could be strengthened by low-spin halos (Herpich et al. 2015). Wang et al. (2018) found that low spin HI-rich galaxies are more prone to host up-bending profiles. Nevertheless, Type-III profiles appear in galaxies both with and without bars (Erwin et al. 2008; Gutierrez et al. 2011). In addition, the lack of significant structural and photometric differences between the Type-III profiles of barred and unbarred galaxies (see Fig. 1.5, reproduced from Eliche-Moral et al. 2015), suggests that either bars are not the only way to produce Type-III profiles or that they survive the disappearance of the bar. Interestingly, Comerón et al. (2012) found that at least half of the Type-III profiles are genuine multi-component structures, caused by a superposition of a thin and a thick discs with different scale-lengths while the rest are associated with only thin discs.

Nevertheless, most of the proposed mechanisms for the creation of Type-III profiles are based on different kinds of gravitational interactions. Erwin et al. (2005) pointed out that many Type-III galaxies present asymmetries in their outskirts. This result was supported by the observations of Pohlen & Trujillo (2006), who found Type-III galaxies associated with possible remnants of interactions. Earlier studies from Laurikainen & Salo (2001) reported that N-body simulations of M51-like pairs presented long-lasting shallow outer profiles, that could be identified as Type-III surface brightness profiles. The authors found out that this was a consequence of the stripping of gas and stars from the galaxies inner discs. Based on numerical simulations, Peñarrubia et al. (2006) proposed that the outer extended discs of M31-like galaxies are composed of the disrupted material of dwarf galaxies that merge in coplanar prograde orbits into the disc. Younger et al. (2007) tested using simulations of interactions that the mass redistribution of the stellar disc caused by minor mergers can create Type-III profiles, specially if the gas fraction of the disc is large enough and the encounter occurs in a prograde direction. Kazantzidis et al. (2009) found that the bombardment of a Milky Way-like galaxy by dark matter subhalos can create extended mass density excesses beyond $\sim$ 5 scale-lengths, which can be associated with the observed Type-III profiles in real galaxies. In Sect. 1.4, we describe in detail the work published in Borlaff et al. (2014) –which was the basis of this PhD project– showing that the remnants from major mergers with S0-like morphologies created with hydrodynamic simulations can reproduce the properties of real Type-III S0 galaxies too.

1.4 Antitruncated stellar discs resulting from major mergers

In Borlaff et al. (2014), the authors investigated whether major mergers could reproduce the properties of Type-III galaxies. The main strategy was to analyse the surface brightness profiles of realistic images created using a set of hydrodynamic simulations of major mergers whose remnants have S0-like morphologies. Then, the authors compared the simulated $R-$band surface brightness profiles with those from a sample of local S0 Type-III galaxies observed by Erwin et al. (2008) and Gutierrez et al. (2011). In order to do that, the authors took advantage of the GalMer database[4] (Chilingarian et al. 2010).

The GalMer database is a library of hydrodynamic N-body simulations of galaxy mergers which contains $\sim$ 1000 simulations of galaxy encounters (including 876 major merger encounters). The simulations consider progenitors with different morphologies (E0, S0, Sa, Sb, Sd) and sizes (g: giant, i: intermediate, d: dwarf). The orbital parameters vary in inclination (0, 45, 75, 90 degrees) and initial relative velocity, considering both retrograde and direct encounters. Each progenitor galaxy is modelled as a spherical non-rotating dark-matter halo, a gaseous disc (with the exception of the E0 and S0 progenitors) and a central non-rotating bulge (excluding the the Sd progenitors). The stellar and gaseous discs follow the Miyamoto-Nagai density profile (Miyamoto & Nagai 1975).

[4]The GalMer database is part of The Horizon Project and it is publicly available at http://galmer.obspm.fr/

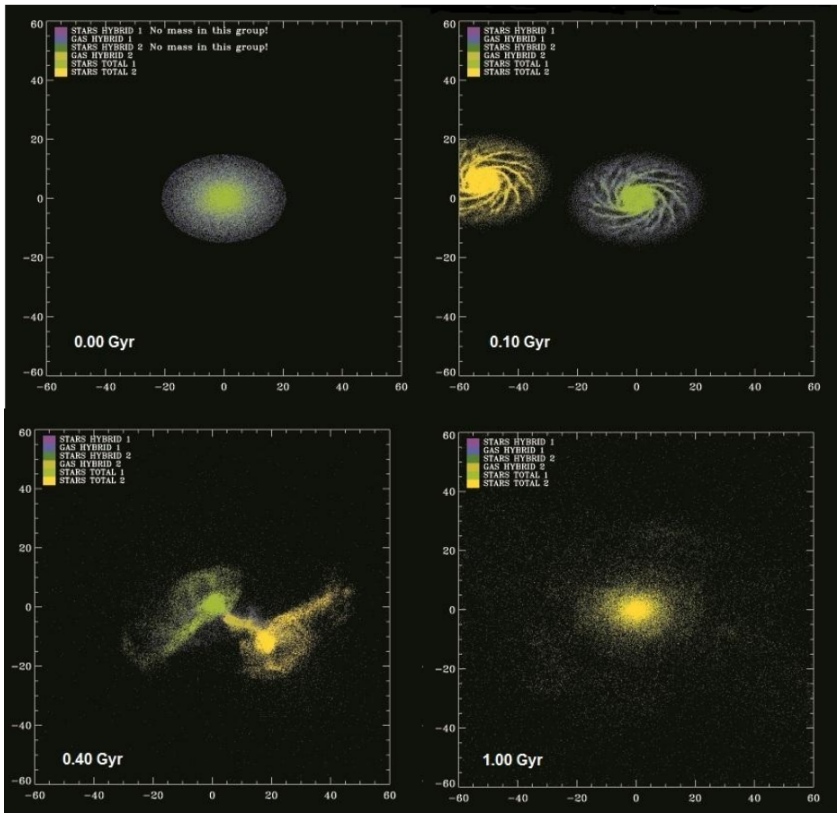

Figure 1.6: Time evolution of the baryonic material in a GalMer major merger simulation. The two progenitors are gSd galaxies (model ID gSdgSdo23). Simulation time is given in the bottom left corner of each frame. Particles belonging to different galaxy components in the two merging galaxies are coded with different colours according to the legend in the panels. The label "Star total" refers to the collisionless stellar content of each progenitor (i.e. the "old stars"). Adapted from Borlaff et al. (2014)

The simulations consider three types of particles: 1) dark matter particles, 2) stellar particles, and 3) hybrid particles. Stellar and dark matter particles only interact gravitationally. The hybrid particles simulate the gaseous component of galaxies, following the method described in Mihos & Hernquist (1994). These particles contain information about the total mass of the particle and its remaining fraction of gas. Each hybrid par-

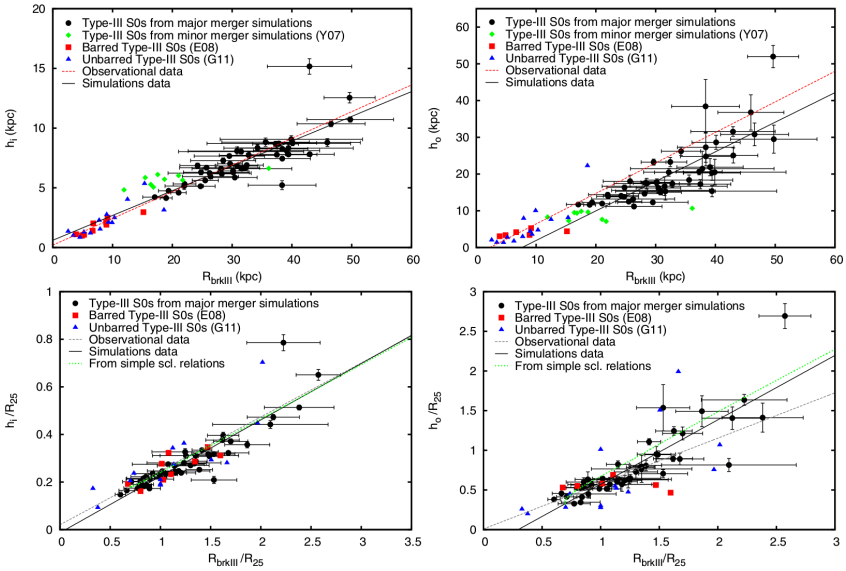

Figure 1.7: Structural scaling relations of the inner ($h_{\rm i}$, left panels) and outer ($h_{\rm o}$, right panels) scale-lengths vs. the break radius ($R_{\rm break}$) for the Type-III profiles from major merger simulations (Borlaff et al. 2014, black dots), minor merger simulations (Younger et al. 2007, green rhombuses) and observations of local Type-III S0 galaxies (Erwin et al. 2008; Gutierrez et al. 2011, red squares and blue triangles, see the legend). We represent the scaling relations normalising the parameters by its relative size (measured as R_{25}, bottom panels) and without normalising (top panels). Solid black line: linear fits to the simulated data. Dashed red line: linear fits to the observational data. Dotted line: expected relations derived from the simple observational scaling relations $h_{\rm i}$ α $R_{\rm break}$, $h_{\rm o}$ α $R_{\rm break}$, and $\mu_{\rm break}$ α $R_{\rm break}$ (we refer the reader to Sect. 3.6 from Borlaff et al. 2014).

ticle contains its own SFR and when the gas fraction falls below a 5%, the particle turns into a stellar particle and its remaining gas is dispersed among its neighbours. The total number of particles for the giant-giant major merger simulations used in Borlaff et al. (2014) is 240,000 (120,000 per progenitor galaxy for the three types of particles), with a total stellar mass of $\sim 0.5 - 1.5 \cdot 10^{11} M_{\odot}$, depending on the morphological type. The total simulation time is $3 - 3.5$ Gyr per experiment. The code uses a hierarchical tree method and the gas evolution is simulated by smoothed particle hydrodynamics, with a softening length of $\epsilon = 280$ pc in the analysed encounters. In addition to star formation, the simulations consider also pressure gradients, gas viscous forces and radiative forces. For more details on the simulations, we refer the reader to the original paper (Chilingarian et al. 2010). We show an example of one of the simulations in Fig. 1.6.

The authors analysed the complete set of giant-giant 876 simulations, classifying 67 as dynamically relaxed with E/S0-S0 morphologies, hosting a significant disc component Eliche-Moral et al. (2018). In order to do that, realistic photometric images were created for the face-on and edge-on orientations, using five broad bands (B, V, R, I and K), assuming stellar population synthesis models (Bruzual & Charlot 2003). For the stellar particles, the authors assumed a fixed age of 10 Gyr (Sil'chenko et al. 2012), adopting the predictions of stellar population evolutionary models which assumed the star formation histories (SFH) characteristic of the morphological type of the progenitor the particle originally belonged to, following Eliche-Moral et al. (2010). Finally, noise was added to the images to an equivalent limiting magnitude of $\mu_{R,lim} = 27.5$ mag arcsec^{-2}. The final resolution of the images was FWHM= 0.7", and the assumed distance to the remnants was $D = 30$ Mpc, corresponding to the maximum distance in the Erwin et al. (2008) and Gutierrez et al. (2011) sample.

Once the realistic images were generated, the authors created one dimensional surface brightness profiles of the relaxed remnants using the R-band images. The surface brightness profiles were then classified in three types by their apparent shape (Type I, Type II and Type III) and their disc profiles (inner and outer separately, if necessary) were fitted to exponential profiles, carefully avoiding the bulge region, mimicking the method used by Erwin et al. (2008) and Gutierrez et al. (2011). For the Type-III profiles, we calculated the break radius ($R_{\rm break}$) and its surface brightness ($\mu_{\rm break}$), the central surface brightness of their inner and outer discs ($\mu_{0,\rm i}$ and $\mu_{0,\rm o}$) and their scale-lengths ($h_{\rm i}$ and $h_{\rm o}$).

The authors found several interesting results:

1. A total of 47 out of 67 relaxed S0-like remnants from major mergers ($\sim 70\%$) host Type-III surface brightness profiles detectable in their R-band images.

2. The scale-lengths of the inner and outer profiles ($h_{\rm i}$ and $h_{\rm o}$) present tight correlations with the break radius ($R_{\rm break}$). These correlations are found in both simulated and real Type-III S0 galaxies (see Fig. 1.7).

3. The surface brightness profiles at the break radius ($\mu_{\rm break}$) and the central surface brightness of the inner and outer profiles ($\mu_{0,\rm i}$ and $\mu_{0,\rm o}$) also correlate with $R_{\rm break}$ in both simulated and real Type-III S0 surface brightness profiles.

4. Due to the size of the simulated progenitors, the Type-III S0 models lie at the high end of the extrapolations of the trends shown by real data towards brighter magnitudes and higher break radii ($h_{\rm i}$, $h_{\rm o}$, $\mu_{\rm break}$, $\mu_{0,\rm i}$ and $\mu_{0,\rm o}$ vs. $R_{\rm break}$). However, simulations and observations overlap completely when weighting $R_{\rm break}$, $h_{\rm i}$ and $h_{\rm o}$ with the relative size of the galaxy, measured as the mean radius of the $\mu_B = 25$ mag arcsec^{-2} isophote (R_{25}). In such scale-free diagrams, the simulated and observed Type-III profiles overlap completely, satisfying the same trends.

5. The presence of bars in some of the real Type-III S0 galaxies does not appear to have any effect or imply a deviation from the observed scaling relations. This

result was later extended to all morphological types by Eliche-Moral et al. (2015) who found no statistical evidence for a difference in the properties of antitruncated stellar discs found in spirals or S0s, barred and unbarred galaxies, both in the R and 3.6 μm bands (see Fig. 1.5).

The authors concluded that the observed distributions of the structural ($h_{\rm i}$, $h_{\rm o}$, $R_{\rm break}$) and photometric parameters ($\mu_{0,{\rm i}}$, $\mu_{0,{\rm o}}$ and $\mu_{\rm break}$) of the surface brightness profiles of simulated Type-III S0-like models resulting from major mergers are compatible with those of the observed galaxies of the same type, taking into account their relative sizes. After a complete destructive event, some models not only reconstructed disc-like structures compatible with the morphologies and kinematics of real S0 galaxies (Querejeta et al. 2015a,b; Tapia et al. 2017; Eliche-Moral et al. 2018), but they also showed Type-III surface brightness profiles. Moreover, the authors found unexpected scaling relations between the break radius and the photometric and structural parameters of the inner and outer profiles of observed Type-III S0 galaxies from Erwin et al. (2008) and Gutierrez et al. (2011), that were well-reproduced by the Type-III S0-like simulated remnants. This demonstrates that major mergers are a viable mechanism for producing Type-III S0 galaxies.

In order to study the origin and evolution of the antitruncated stellar discs and discriminate between the mechanisms explained here it is necessary to identify and compare samples of Type-III galaxies of the same type at different intervals of z. In two of the papers included in this thesis (Borlaff et al. 2017, 2018, see Chapters 3 and 4) we continue the work presented in this introduction, obtaining a sample of Type-III S0 galaxies in a significant range of distances ($0.2 < z < 0.6$) in order to investigate if there is an evolution in the structural and photometric properties and the scaling relations of the Type-III profiles found in Borlaff et al. (2014) with z.

1.5 The outskirts of galactic discs in the local universe and beyond

Driven by the realisation that all the knowledge that we have about galaxies is extremely biased by the shape of their surface brightness profiles, Disney (1976) accurately stated: "galaxies are like icebergs and what is seen above the sky background may be no reliable measure of what lies underneath". As the quality of the photographic plates improved, the astronomers started to discover new structures in the outskirts of otherwise apparently relaxed and "normal" galaxies. One of the first examples is Malin & Carter (1980). In this paper, the authors discovered giant shell-shaped stellar structures around "normal" elliptical galaxies (see the original image of NGC1344 in the left panel of Fig. 1.8). Malin & Carter discussed several scenarios for the formation of such shells, from an explosive event in the nucleus that displaced the old stars to the outskirts, to a powerful shock wave that propagated the star formation through the intergalactic medium, and finally the hypothesis that the stellar shells were in fact the relic of a galactic merger. Although the latter scenario was supported by contemporary theories of galactic interactions (Toomre 1978; White 1978; Aarseth & Fall 1980), this hypothesis was discarded due to the apparent lack of irregularities in their nuclei that could be identified as a sign

of a recent galactic collision. Nevertheless, later models (Quinn 1984; Dupraz & Combes 1986; Hernquist & Quinn 1988) and observational studies (Ebrova 2013; Carlsten et al. 2017) found that such arc-like structures were in fact clues of past mergers that shaped the outskirts of such galaxies. In fact, deep explorations of the outskirts of apparently undisturbed spiral galaxies often reveal large tidal tails and shell-like structures (see NGC4651, right panel of Fig. 1.8).

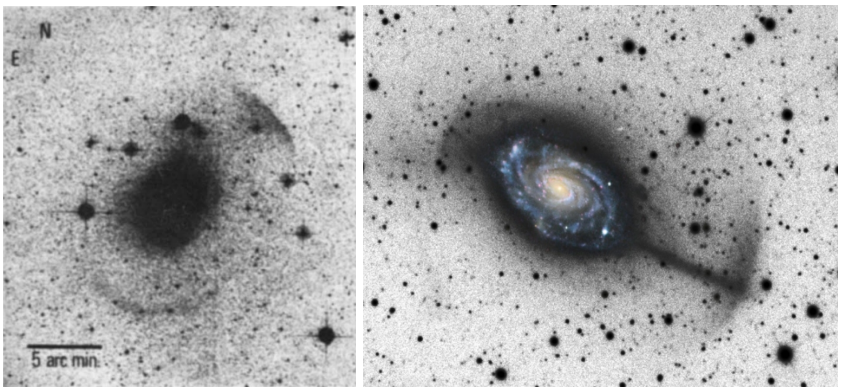

Figure 1.8: Examples of observations of merging remnants in the outskirts of galaxies. *Left panel:* Shell structures around the elliptical galaxy NGC1344, detected with the UK Schmidt Telescope in a IIIaJ photographic plate (reproduced from Malin & Carter 1980). *Right panel:* Umbrella shaped tidal debris around the spiral galaxy NGC4651. LRGB (luminance, red, green and blue) image composition (reproduced from Martínez-Delgado et al. 2010).

Consequently, the outskirts of disc galaxies also contain valuable information about their formation pathways. As previously discussed in Sect. 1.2, detailed imaging of the outskirts of disc galaxies allowed the identification of important features of galactic discs, such as breaks and truncations (Freeman 1970; van der Kruit 1979), which are tightly related to the formation of the exponential disc itself and possibly to the amount of angular momentum of the initial halo. Deep imaging is the key to unveiling the nature of the extended surface brightness profiles of Type-III galaxies in the local Universe (Pohlen & Trujillo 2006; Erwin et al. 2005) and beyond (see Borlaff et al. 2017, 2018, included in this thesis, in Chapters 3 and 4). Increasing image depth also allowed the detection of old stellar thick discs in edge-on disc galaxies (Burstein 1979; Tsikoudi 1979; Dalcanton & Bernstein 2002; Comerón et al. 2014; Elmegreen et al. 2017) and stellar warps (Sanchez-Saavedra et al. 1990; Reshetnikov & Combes 1999; Reshetnikov et al. 2016). The observed flares – increases of the vertical scale of the discs with the galactocentric radius (see Sect. 1.3.2 and Chapter 2) – have been both detected on HI

and stellar discs (de Grijs 1998; Kregel et al. 2002; Narayan & Jog 2002), and have been proved to be a possible cause of the ubiquitous appearance of Type-II profiles on edge-on galaxies (see Borlaff et al. 2016, included in this thesis in Chapter 2). In addition to these effects, it is known that the light distribution of the outskirts of $\sim 30\%$ of disc galaxies present significant deviations from axisymmetry, known as lopsided asymmetries (Block et al. 1994; Rix & Zaritsky 1995; Jog & Combes 2009). Such an effect is not always related to interactions, but in some cases it could be caused by the triaxial shape of the host dark matter halo (Zaritsky et al. 2013). Moreover, the study of tidal tails in ongoing satellite accretion processes (Forbes et al. 2003; Martínez-Delgado et al. 2008, 2009, 2010) and stellar and gas bridges (Toomre & Toomre 1972; Smith et al. 2007) provide valuable information about the transformation processes that define the structure, photometry, star formation and metallicity of a galaxy during accretion and interactions processes. These features are rarely bright but appear in many deep images of apparently relaxed galaxies. In fact, numerical simulations predict that half of the galaxies would show at least a tidal structure in their outskirts if explored down to a limiting magnitude $\mu_{lim} \sim 30$ mag arcsec^{-2} (Bullock & Johnston 2005; Johnston et al. 2008). Finally, tightly connected to the previous cases, stellar halos (Ibata et al. 2007; Martínez-Delgado et al. 2010; Trujillo & Fliri 2016; Buitrago et al. 2017) give us information about the past accretion history of galaxies and the shape of the dark matter halo, providing an observational test for the ΛCDM cosmological scenario. These studies prove that probably most of the extensions of galaxies are still buried under the noise of the current astronomical images, keeping a fossil record of the past and present of the formation of disc galaxies.

In addition to this, deep, high-resolution observations allow us to detect such structures at cosmological distances, helping to understand the evolution and origin of the outskirts of galaxies. An important factor to take into account is that in an expanding Universe, the energy flux that an observer receives from a distant source is reduced because the Universe expanded since its departure. At the same time, the energy of the photons is reduced because of z, while the apparent angular size of the object is larger because the observer-source distance was smaller when the light departed. If we take into account all these effects together, we obtain that the observed surface density of intensity gets reduced by a factor $I_{obs} = I_{rest-frame} \cdot (1+z)^{-4}$, which in magnitudes translates to:

$$\mu_{obs} = \mu_{rest-frame} + 10 \cdot \log_{10}(1+z) \tag{1.1}$$

This effect is known as the surface brightness cosmological dimming (Tolman 1930, 1934) and affects significantly all the observations of extended sources beyond the local Universe. In the top panel of Fig. 1.9 we show how the limiting magnitude of several reference studies varies with z because of this effect, and we compare with the typical surface brightness magnitude of a number of structures. At $z = 1$, our rest-frame magnitude limit is ~ 3 magnitudes brighter than in the local Universe. Beyond that redshift, it would be impossible to detect stellar halos as bright as those from the local Universe with the deepest astronomical images ever created to date (the Hubble Ultra Deep Field, HUDF hereafter). Nevertheless, galaxies were brighter in the past (Bruzual & Charlot

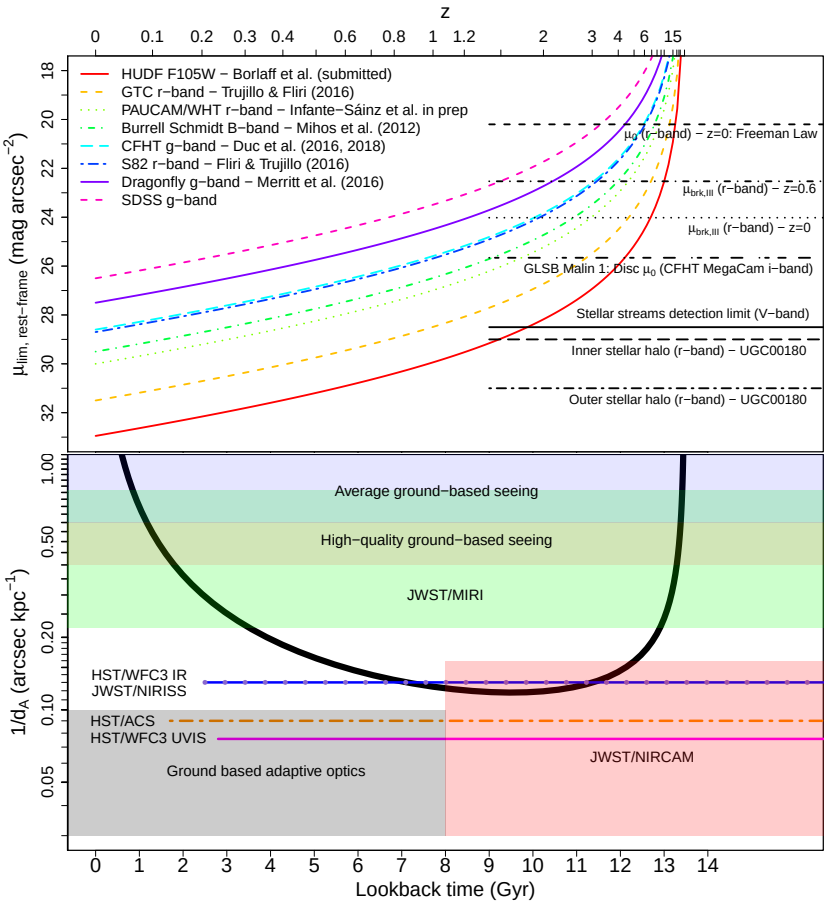

Figure 1.9: *Top panel:* Dependence of the limiting magnitude of several reference studies as a function of z (in colour lines, see the legend in the panel for reference), due to the cosmological dimming (Tolman 1930, 1934). In black lines we represent the typical surface brightness of different galactic structures for reference. 1) Median central surface brightness of a disc galaxy (r-band, dashed line, Fathi 2010). 2) Median surface brightness at the break radius for Type-III S0 galaxies at $z = 0.6$ (dashed-dotted line, Borlaff et al. 2017, 2018). 3) Median surface brightness at the break radius for Type-III S0 galaxies in the local Universe (r-band, dotted line, Borlaff et al. 2017, 2018). 4) Central surface brightness of the Giant Low Surface Brightness galaxy Malin 1 (CFHT Megacam i-band, Bothun et al. 1987; Boissier et al. 2016). 5) Stellar stream detection limit (V-band, solid line, Bullock & Johnston 2005). 6) Inner and 7) outer stellar halo detection limit (r-band, dashed-dashed line, Trujillo & Fliri 2016). *Bottom panel:* Dependence of the inverse angular scale ($1/d_A$) as a function of the lookback time. For comparison, the horizontal lines and coloured areas represent the limiting resolution for ground-based observations (with and without adaptive optics) and the imaging instruments aboard HST (WFC3 and ACS) and JWST (NIRISS, NIRCAM and MIRI).

2003) partially compensating this effect. In fact, there is a ~ 1.5 mag arcsec^{-2} difference between the surface brightness at the break radius for Type-III S0 galaxies at $z = 0$ and $z = 0.6$ (Borlaff et al. 2018, see Chapter 4). Note that the cosmological dimming is probably the most important limitation to the study of the high-z low surface brightness Universe, imposing a steep variation of the rest-frame limiting magnitude with redshift. We quantified this problem for the detection of Type-III surface brightness profiles in Borlaff et al. (2018, see Sect. 3.6.1), which is based on deep HST/ACS observations of the GOODS-N cosmological field (Giavalisco et al. 2004; Skelton et al. 2014).

Once we identified the first sample of anti-truncated stellar discs out to $z \sim 0.6$ (Borlaff et al. 2017, 2018), the next natural step is to continue the exploration to $z \sim 1$ and beyond. At $z = 1$, the angular scale is $d_A \sim 8$ kpc arcsec^{-1} (see Fig. 1.9, bottom panel). Thus, in order to resolve the structure of the discs at $z \sim 1$, high-resolution (FWHM < 0.1 arcsec) and ultra-deep imaging ($\mu_{lim} > 30$ mag arcsec^{-2}, 3σ measured on 10×10 arcsec boxes) data is necessary. In addition, in order to observe high-redshift objects at similar rest-frame wavelengths compared to the local galaxies (which usually are studied in the optical $R-$band or similar wavelengths, Erwin et al. 2008; Gutierrez et al. 2011), the observations must cover the near-infrared region of the spectrum ($\lambda = 1.0 - 1.6\,\mu m$). With a limiting magnitude of ~ 32.5 mag arcsec^{-2} (3σ measured on 10×10 arcsec boxes) and a resolution of 0.06 arcsec, the WFC3/IR Hubble Ultra Deep Field (Koekemoer et al. 2012; Illingworth et al. 2013) provides the best observations for our purposes. Located in the southern hemisphere (α=3h 32m 39.0s, $\delta = -27; 47; 29.1$, J2000), in the Fornax Constellation, it is inside the Chandra Deep Field South (Giacconi et al. 2002) and the GOODS-South Field (Giavalisco et al. 2003) and it covers an area of 2.2×2.4 arcmin^2. Multiple follow-up projects have expanded the observations of the HUDF at very different wavelengths from radio (VLA, Rujopakarn et al. 2016 and ALMA, Dunlop et al. 2016; Aravena et al. 2016b,a; Walter et al. 2016), to infrared (Spitzer/IRAC, Labbe et al. 2015), optical and near-infrared (NIR) spectroscopy (VLT/MUSE, Bacon et al. 2017), ultraviolet (WFC3/UVIS, Teplitz et al. 2013), and X-rays (Chandra, Xue et al. 2011; Luo et al. 2016), (XMM-Newton, Comastri et al. 2011), providing ancillary data to make of this field the best candidate to study the shape of the disc galaxies at $z \sim 1$ and beyond.

Three main reduced versions of the WFC3/IR HUDF data have been published up to now, adding subsequently more exposure time to the final mosaics: HUDF09 (Bouwens et al. 2009), HUDF12 (Koekemoer et al. 2012) and XDF (Illingworth et al. 2013). The reduction process of such ultra deep fields is an extremely challenging task. Although space may provide better stability to the observation conditions, due to the lack of atmospheric changes (temperature, humidity, less contamination by stray light), in-orbit observations present a large number of problems compared to ground-based observations, such as the difficulty of creating accurate flat-fields or the rapid variation of the infrared sky-background in orbit. One of the largest problems is the sky-background and residual gradients subtraction. While XDF is the lastest version of the HUDF mosaics and the one that includes more exposure time, their sky subtraction procedure was extremely aggressive, artificially over-subtracting the outskirts of the largest objects in the field.

The result is the presence of regions with negative counts around the largest objects. We must note that while this strategy may be suitable for the analysis of small, unresolved sources at high-z (which was the primary objective of the observations), it produces a systematic bias in the outer regions of the extended objects. We will address this problem in Chapter 5, where we present a dedicated version of the HUDF WFC3 mosaics for the study of the low surface brightness limits of the extended objects, in particular the outskirts of galaxy discs up to $z \sim 1$ (Borlaff et al. submitted).

2

Type-II surface brightness profiles in edge-on galaxies produced by flares

Observation: You couldn't see a thing.
Conclusion: dinosaurs.
— Carl Sagan, *Cosmos: A Personal Voyage*

In this chapter we study one of the possible causes for the presence of down-bending surface brightness profiles in edge-on galaxies: galactic disc flares. In Borlaff et al. (2016) we investigate if the apparent ubiquity of Type-II profiles in edge-on galaxies could be a projection effect, due to the variation of the vertical scale-height of the stellar disc. Most surface brightness profiles of such objects are performed by using slits of a fixed width along the major axis of the galaxy. This technique allows the observer to analyse the profile at different heights in order to avoid the dust extinction of mid-plane regions, for example. Early studies considered that the vertical scale-height (h_z) of disc galaxies was independent of radius (van der Kruit & Searle 1981a,b, 1982; Kylafis & Bahcall 1987; Shaw & Gilmore 1990; Barnaby & Thronson 1992). In contrast, later studies reported that h_z actually increases with the galactocentric radius in some galaxies (de Grijs & Peletier 1997; Bizyaev et al. 2014), making the galactic discs thicker in the outskirts when compared to the inner regions. This effect is called flaring, and it reduces the local density of stars in the galactic plane at high galactocentric radii. Strong flaring has been found in the disc of the Milky Way (López-Corredoira et al. 2002; López-Corredoira & Molgó 2014; Kalberla et al. 2014), and in fact, cosmological based simulations predict that flaring in the edges of old stellar discs may be a common feature for most galaxies (Minchev et al. 2015).

The surface brightness profile of an edge-on disc galaxy with a flare measured along an fixed width slit is dimmer at the outskirts than in the case of an equivalent galaxy that does not not suffer from flaring (see the scheme in Fig. 2.1). This is because the density of stars in the galactic plane is smaller in a galaxy with a flare than in the non-flared case, reducing the observed intensity. In most cases, the shape of the flare

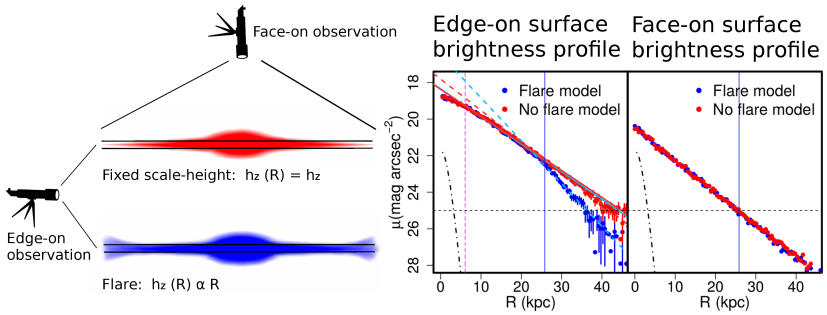

Figure 2.1: Projection effects of a flare on the outskirts of surface brightness profiles of disc galaxies. The red galaxy presents a fixed scale-height to all radius, while the blue galaxy present an obvious flare. In the right section of the diagram, we represent the edge-on (left) and face-on (right) surface brightness profiles from a model. The mid-plane density of stars is smaller in the outskirts of the galaxy with a flare, resulting in a down-bending profile in an edge-on view (see panels on the right). This effect would not be detectable in face-on galaxies (see the right panels). Adapted from Borlaff et al. (2016)

would not be directly detectable on the images. The excess of light above and below the galactic plane at high galactocentric radius can be buried deeply into the noise level, making it undetectable on the images and it would only create a noticeable effect on one-dimensional surface brightness profiles. Interestingly, if we were able to travel fast enough through space to observe the same galaxies in a face-on orientation, we would find that the surface brightness profile of both galaxies (the one with a flare and the one with a fixed h_R) is exactly the same. The reason for this is that while the density in the galactic plane gets smaller with higher h_R, the integrated density along the vertical direction remains the same, yielding equal surface brightness profiles.

Kregel et al. (2002) briefly analysed with numerical models if this effect could create the observed truncations of the old stellar discs of a sample of 34 edge-on galaxies, concluding that flares could not create the down-bending profiles observed in real edge-on galaxies. However, these authors underestimated the strength of real flares according to more recent studies (López-Corredoira et al. 2002; López-Corredoira & Molgó 2014; Kalberla et al. 2014). In Borlaff et al. (2016) we thoroughly revisited this topic using 10,000 realistic 3D models for the bulge and the disc, paying special attention to the shape and strength of the flare as a function of the morphological type and stellar mass. We found that flares can produce intermediate-to-low strength Type-II profiles in edge-on galaxies, in agreement with the observations. Moreover, our models explain the observed inner to outer scale-length ratio distribution of breaks found by Martín-Navarro et al.

(2012) in a sample of edge-on galaxies. These breaks were interpreted by the authors as an effect of star formation thresholds at some galactocentric radii. In addition, we found that flaring can easily explain the observed weakening of the breaks with the increasing distance from the plane reported by Pohlen et al. (2007). We conclude that Type-II discs produced by flares reproduce the properties of real Type-II edge-on discs with intermediate-to-low break strengths. The work presented in this Chapter was published as a Letter to the Editor in *Astronomy & Astrophysics* the 21st of June of 2016, in the Volume 591, with article number L7, under the title **"Type-II surface brightness profiles in edge-on galaxies produced by flares"**.

A&A 591, L7 (2016)
DOI: 10.1051/0004-6361/201628868

Astronomy & Astrophysics

Letter to the Editor

Type-II surface brightness profiles in edge-on galaxies produced by flares

Alejandro Borlaff[1,3], M. Carmen Eliche-Moral[2], John Beckman[1,3,4], and Joan Font[1,3]

[1] Instituto de Astrofísica de Canarias, C/ vía Láctea, 38200 La Laguna, Tenerife, Spain
e-mail: asborlaff@iac.es
[2] Departamento de Astrofísica y CC. de la Atmósfera, Universidad Complutense de Madrid, 28040 Madrid, Spain
[3] Facultad de Física, Universidad de La Laguna, Avda. Astrofísico Fco. Sánchez s/n, 38200 La Laguna, Tenerife, Spain
[4] Consejo Superior de Investigaciones Científicas, Spain

Received 6 May 2016 / Accepted 30 May 2016

ABSTRACT

Previous numerical studies had apparently ruled out the possibility that flares in galaxy discs could give rise to the apparent breaks in their luminosity profiles when observed edge-on. However the studies have not, until now, analysed this hypothesis systematically using realistic models for the disc, the flare, and the bulge. We revisit this theme by analysing a series of models which sample a wide range of observationally based structural parameters for these three components. Using observational data, we have considered realistic distributions of bulge-to-disc ratios, morphological parameters of bulges and discs, vertical scale heights of discs and their radial gradients defining the flare for different morphological types and stellar mass bins. The surface brightness profiles for the face-on and edge-on views of each model were simulated to find out whether the flared disc produces a Type-II break in the disc profile when observed edge-on, and if so under what conditions. Contrary to previous claims, we find that discs with realistic flares can produce significant breaks in discs when observed edge-on. Specifically a flare with the parameters of that of the Milky Way would produce a significant break of the disc at a $R_{\rm brkII}$ of ∼8.6 kpc if observed edge-on. Central bulges have no significant effects on the results. These simulations show that flared discs can explain the existence of many Type-II breaks observed in edge-on galaxies, in a range of galaxies with intermediate to low break strength values of $-0.25 < S < -0.1$.

Key words. galaxies: formation – galaxies: fundamental parameters – galaxies: evolution – galaxies: structure – Galaxy: disk – Galaxy: structure

1. Introduction

Disc galaxies often do not show a single radial exponential surface brightness profile (Freeman 1970). Pohlen & Trujillo (2006) and Erwin et al. (2008) classified the discs of galaxies into three classes according to the shape of their profiles. Type-I discs are well modelled with a single exponential profile. Type-II discs present a down-bending profile, i.e. a brightness deficit in the outer parts of the disc with respect to the extrapolation of the inner profile outside a given "break radius". Finally, the profiles of Type-III discs are shallower outside the break radius than the extrapolation of the inner exponential profile (antitruncation). In the present study we focus on Type-II profiles.

Sharp truncations in galaxy disc profiles were first reported in edge-on galaxies (van der Kruit 1979). Owing to projection effects, edge-on galaxies present a larger number of truncations and Type-II breaks than their face-on counterparts (Pohlen et al. 2007). Recent studies associate sharp truncations with stellar density cut-offs and inner down-bending breaks to different stellar formation thresholds (Martín-Navarro et al. 2012). Laine et al. (2014) found an interesting correlation between the break in Type-II profiles and the characteristic radii of structures in the galaxy: lenses, rings or pseudorings. This means that these morphological features may be associated with the break in some Type-II profiles. Previous studies also explored the possibility that flares (i.e. an increase in the scale height of the stellar disc with galactocentric radius) may be responsible for the down-bending profiles detected in highly inclined galaxies. More than a decade ago, Kregel et al. (2002) performed 2D decompositions of 34 edge-on late-type galaxies; 60% of them showed Type-II profiles. The authors studied whether a linear radial increase in the scale height of the disc could produce some of the detected truncations if the discs were observed at high inclination. They created a set of artificial images (∼50 simulations) using a random uniform distribution covering the observed range of values of the disc central surface brightness (μ_0), disc scale length (h_R), disc scale height (h_z), bulge effective surface brightness (μ_e), bulge effective radius (r_e), and bulge axial ratio (q) of their data. They also restricted the bulge-to-disc ratio to $B/D < 2$. Finally, they concluded that values of the radial gradient of the scale height larger than 1 h_z per h_R are needed – according to their models – to reproduce the characteristics of the observed truncations. However, this gradient in late-type galaxies is typically very low ($\nabla_R h_z \sim 0.1\ ^{h_z}/_{h_R}$, see de Grijs & Peletier 1997), so Kregel et al. concluded that flaring is a very unlikely explanation for the breaks observed in late-type galaxies.

Radial variations of the scale height of galaxy discs are difficult to measure (Mosenkov et al. 2015), but as better and deeper data are obtained, higher values of the radial gradient of the scale height ($\nabla_R h_z$) are being derived even for late-type galaxies (Bizyaev et al. 2014). The Milky Way (MW, which is thought to be an SBbc galaxy) exhibits a thin+thick disc structure, both affected by a particularly strong flare ($\nabla_R h_z \sim 0.15$ at 20 kpc for the thick disc; López-Corredoira et al. 2002; López-Corredoira & Molgó 2014; Kalberla et al. 2014). Cosmological simulations also predict much stronger flares for old stellar discs than current

A&A 591, L7 (2016)

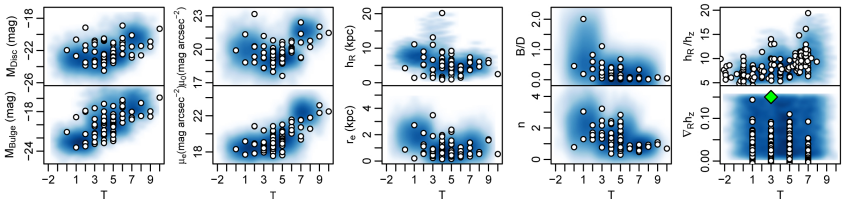

Fig. 1. Photometric and structural parameter distributions for the simulations. Density clouds represent the parameter distributions of the 10 000 3D simulations of realistic bulge + flared disc light distributions created from the observations as a function of the morphological type, T. Dots represent the observations from Graham (2001), Kregel et al. (2002), Bizyaev et al. (2014) and Mosenkov et al. (2015). *Upper row, from left to right*: disc absolute magnitude $M_{\rm abs,disc}$, disc central surface brightness μ_0, disc scale length h_R, bulge-to-disc ratio B/D, and disc radial-to-vertical scale-lengths ratio h_R/h_z. *Lower row, from left to right*: bulge absolute magnitude $M_{\rm abs,bulge}$, bulge surface brightness at the bulge effective radius μ_e, effective radius r_e, bulge Sérsic index n, and the radial gradient of h_z, $\nabla_R h_z$. The green diamond represents the MW.

data reveal (Minchev et al. 2015). These authors have pointed out that the phenomenon may be unavoidable on the outskirts of galaxies. Consequently, the effects of flares on the disc profiles of edge-on galaxies may have systematically been underestimated in previous studies.

No study has analysed systematically whether flares can produce Type-II profiles in highly inclined discs, using realistic models for the bulge, the disc, and (especially) the flare. So we have revisited this question to quantify the possible effects of realistic flares on the generation of breaks in edge-on disc profiles. To this end, we used observations for different morphological types and masses to create 3D models of disc galaxies assuming distributions of B/D, bulge and disc photometric parameters (μ_0, h_R, μ_e, r_e, Sérsic index n), scale heights of the discs, and their trend with the galactocentric radius. To properly sample the complete range of parameters, we performed 10 000 simulations of realistic flared disc galaxies. We derived edge-on and face-on surface brightness profiles for the resulting flared galaxy models. The surface brightness profile of each galaxy model was analysed to find out whether the flare produces a significant break in the disc in the edge-on view compared with the face-on view.

2. Methods

We created 10 000 3D models of galaxies, each with an exponential disc plus a Sérsic bulge. We adopted the following functional form for the exponential disc (López-Corredoira et al. 2002):

$$\rho(R,z) = \rho_0 \cdot \exp\left(\frac{-R}{h_R}\right) \cdot \exp\left(\frac{-|z|}{h_z(R)}\right) \cdot \frac{h_z(R)}{h_z(0)}. \quad (1)$$

Following the observations, we explored the effect of a linear increase in the vertical scale height, as follows:

$$h_z(R) = \begin{cases} h_z(0) & \text{if } R \le R_{\rm flare} \\ h_z(0) + \nabla_R h_z \cdot R & \text{if } R > R_{\rm flare}. \end{cases} \quad (2)$$

Graham (2001) analysed a sample of 86 face-on disc-dominated galaxies previously selected by de Jong & van der Kruit (1994). This author performed a bulge + disc decomposition for 69 galaxies in the I-band, correcting for the effects of the internal extinction, Galactic extinction, inclination, and cosmological dimming (Graham 2003), that we used as a reference for our models. We estimated stellar masses using the relationship between the V-band mass-to-light ratio of galaxies and their dust-corrected rest-frame colours derived by Wilkins et al. (2013). According to these authors, for $z < 0.1$ the optimal observed colour is $(B - V)$, so we have estimated this colour for the 69 galaxies of Graham (2003) from HyperLeda data[1], and estimated the stellar mass of each galaxy using the relations in Wilkins et al. For those objects without $(B - V)$ available in HyperLeda, we estimated them from their SDSS $(g - r)$ colour following the transformations published in Jester et al. (2005). To simulate realistic images of the disc galaxies, we adopted the observational I-band distributions of Graham (2001, 2003) for the photometric parameters (r_e, Sérsic index n, h_R, μ_0, μ_e, B/T, the absolute magnitudes of the disc $M_{\rm abs,disc}$ and the bulge $M_{\rm abs,bulge}$), and four morphological type bins (S0–Sa, Sb–Sbc, Sc–Scd and Sd–Sdm), in three mass bins ($10 < \log_{10} M/M_\odot < 10.7$, $10.7 < \log_{10} M/M_\odot < 11$ and $\log_{10} M/M_\odot > 11$) in order to explore realistic mass distributions for the morphological type bins. In Fig. 1 we represent the distributions of the structural and photometric parameters from which we created the models and compared them to the observations they are based on. For each morphological type bin we randomly chose the ratio of scale height to scale length (h_z/h_R) from the observational range of values corresponding to each type reported by Kregel et al. (2002) and Mosenkov et al. (2015) in the I-band, as shown in Fig. 1.

We explored the range of $\nabla_R h_z$ values derived by recent observational studies for galaxies of different types (see also Fig. 1) in the I-band: $0 < \nabla_R h_z < 0.15$ (Bizyaev et al. 2014; Mosenkov et al. 2015). These values agree with those measured in the MW by several authors (Alard 2000; López-Corredoira et al. 2002; Momany et al. 2006; Hammersley & López-Corredoira 2011; López-Corredoira & Molgó 2014; Kalberla et al. 2014, and references therein). Mosenkov et al. (2015) argued that the scale heights derived from 1D decompositions may be biased to higher values than reality owing to bulge contamination (up to 10% in galaxies with $B/T \sim 0.4$). Therefore, we restricted the sample from which we obtain the scale-height gradients to objects with $B/T < 0.4$ to avoid bulge contamination. The radius at which the flare starts ($R_{\rm flare}$) is randomly chosen following a uniform distribution between 2 and 5 times the scale length of the disc. The lowest value is set to avoid bulge contamination from the inner regions of the profile (de Grijs & Peletier 1997), while the highest value is the typical maximum radius where the limiting magnitude of both edge-on and face-on images is reached: $\mu_{\rm lim} = 25$ mag arcsec^{-2}. At higher radial distances the flare would not have any significant effect on our profiles. Finally, once a set of parameters describing a realistic galaxy model is

[1] HyperLeda database available at: http://leda.univ-lyon1.fr/

created, we check that the chosen values of $M_{\rm abs,disc}$ and $M_{\rm abs,bulge}$ provide a B/T ratio within the observed distribution of B/T values for the stellar mass and morphological type of the galaxy. We created a non-flared analogue of each flared model in order to compare their edge-on profiles. The 3D models of luminosity distribution in the I-band have a spatial resolution of 1 arcsec, with a total size of 301 arcsec in each direction. The adopted resolution is similar to the typical FWHM achieved with ground-based seeing-limited observations. We assumed a distance of 100 Mpc to the simulated object, which is the upper limit of the distance distribution of the galaxies in Graham (2001). Owing to the increase in the thickness of the disc in the flared models, the simulations might suffer from flux loss because of the limited box size. To prevent this, we automatically removed any models with differences greater than 1% in total flux between the flared and non-flared models. We created face-on and edge-on density images by integrating along the line of sight. The images are then convolved with a Gaussian kernel of $\sigma = 1$ arcsec. The surface brightness profile for each galaxy model has been derived for edge-on and face-on views, by locating a 1 arcsec wide single slit along the major axis in the first case and with the `ellipse` task in IRAF in the second. We included Poissonian noise across the whole profile. We assumed *Planck* cosmology when required ($\Omega_{\rm M} = 0.31, \Omega_\Lambda = 0.69$, $H_0 = 67.8$ km s^{-1} Mpc^{-1}; Planck Collaboration XIII 2015).

We took the model of the MW presented in López-Corredoira & Molgó (2014) as reference. These authors fitted SDSS-SEGUE MW data to a flared thin+thick disc model, obtaining compatible and deeper results than previous studies (López-Corredoira et al. 2002). They provide the 3D distribution, h_z distribution, as well as the fitted parameters for the thin and thick discs and both flares. We built up this model following the described procedure. For this model, we also created a non-flared analogue MW model by assuming the scale height at the sun's radius to be constant for the whole disc.

3. Results and discussion

In Fig. 2 we present one example of the realistic flared and non-flared models that we have created. The top and middle panels represent the simulated images for the flared and non-flared model of a galaxy with a stellar mass of 10^{10} $M_\odot$ and type Sd–Sdm, for edge-on and face-on views. The lower panels show the surface brightness profiles for the two models and for both inclinations (see the caption for details). The main result is that there is no significant difference between the flared and non-flared models in face-on orientation, either in the images or in the surface brightness profiles. On the contrary, when we compare the models in edge-on orientation, we clearly detect a break in the surface brightness profile of the flared model that does not appear in the non-flared analogue. We have found detectable breaks in the edge-on profiles of ∼42% of all our models including a flare, with a mean strength[2] of $S = -0.15$, and 98% of them with $-0.21 < S < -0.11$. We obtain higher detection rates in brighter discs (i.e. higher masses), and in those models with values for $\nabla_K h_z$ greater than ∼0.05. This is expected if a fixed limiting magnitude and spatial resolution is assumed. This means that realistic flares can frequently produce noticeable Type-II breaks in highly inclined galaxies, contrary to previous claims.

[2] The strength of a disc break is defined as $S = \log_{10}(h_{\rm o}/h_{\rm i})$, with $h_{\rm i}$ and $h_{\rm o}$ the scale lengths of the inner and outer discs.

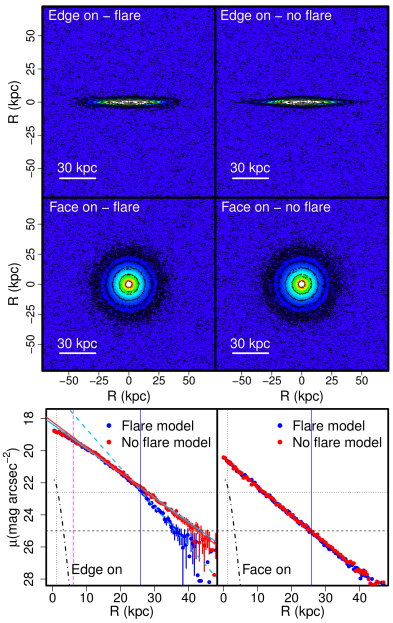

Fig. 2. *Top panels*: edge-on I-band images for the flared and non-flared models. *Intermediate panels*: the same for the face-on discs. *Bottom panels*: surface brightness profiles in the major axis of the galaxy for edge-on (*left*) and the face-on (*right*) views of the two models (red: non-flared model, blue: flared model). Blue vertical solid line: flare radius $R_{\rm flare}$. Black dot-dashed line: bulge component. Solid blue and red lines: linear fits performed to the inner regions of the disc for the flared and non-flared models. Dashed blue and red lines: the same for the outer regions of the disc. Black dotted lines: bulge $r_{\rm e}$ and $\mu_{\rm e}$values. Horizontal dashed black line: limiting magnitude $\mu_{\rm lim} = 25$ mag arcsec^{-2}. Vertical dashed magenta line: inner limit for the inner profile. We note that the disc profile in the flared case exhibits a clear Type-II break in the edge-on view, whereas the non-flared model keeps the exponential profile that both models exhibit in the face-on view. See the legend for details.

Concerning the MW reference model, we find a significant drop in its surface brightness profile at $8.58^{+0.43}_{-0.31}$ kpc in the edge-on profile in the flared model, which is not observed either in the face-on profile or in the edge-on profile of its non-flared analogue. We obtained a break strength $S = -0.22$ for the break of the MW flared model. Therefore, we conclude that a flare such as the one reported for the MW in many studies, would produce a Type-II profile if the MW were observed edge-on.

In Fig. 3 we represent the ratio between the break radius and the scale length of the inner disc ($R_{\rm brkII}/h_{\rm i}$) vs. the break strength (S). The flared models reproduce the observations by Laine et al. (2014) in the lower break strength part of the real distribution ($-0.25 < S < -0.1$). We note that our 3D models are dust-free by construction. We can compare them because the authors use data in the K and 3.6 microns bands; these data are negligibly

A&A 591, L7 (2016)

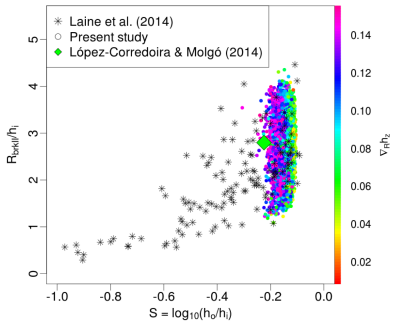

Fig. 3. Break radius normalized by the inner disc scale length vs. the break strength S. Our simulations are plotted with colour-coded circles according to $\nabla_R h_z$. The edge-on MW model is overplotted with a green diamond. The asterisks represent the Type-II breaks observed by Laine et al. (2014) from the S^{4}G survey. See the legend in the figure.

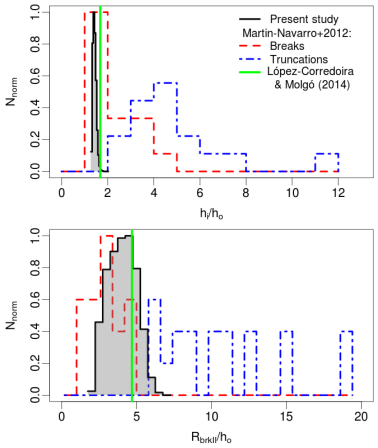

Fig. 4. Histograms comparing the distribution of Type-II profiles from the present study and Martín-Navarro et al. (2012), as a function of the ratio between the inner and the outer scale length h_i/h_o (*upper panel*) and of the break radius normalized by the outer scale length R_{brkII}/h_o (*lower panel*). The vertical green lines mark the values for the MW reference model. See the legend in the figure.

affected by dust extinction. We find a significant correlation between S and $\nabla_R h_z$ ($\rho_{Spearman} = -0.32$, p-value $< 10^{-5}$), which is not found between S and the morphological type (see Fig. A.1).

In Fig. 4, we compare characteristics of the Type-II profiles from the observational sample by Martín-Navarro et al. (2012) with those of our flared models. These authors identify two types of Type-II profiles: the breaks, which appear as down-bending transitions, and the truncations, much steeper and located much further out. In order to reproduce the latter type, often classified as sharp truncations, we would require significantly greater values of $\nabla_R h_z$ than those reported in galaxies by current observational studies, including the MW. This contrasts with the breaks, whose distribution can be partially reproduced by flared discs, as demonstrated by our models.

We have also studied the surface brightness profiles as a function of the distance from the galactic plane in the flared models that exhibit breaks in their edge-on profiles. We find an increase in the values of h_i and h_o with z equal to factor of $1.15^{+0.23}_{-0.12}$ for the inner disc and $2.19^{+1.21}_{-0.72}$ for the outer disc up to a maximum height of $z/h_z \leq 5$, such that h_o becomes closer to h_i. This agrees with the results of Pohlen et al. (2007), where the authors found a significant weakening of the breaks with increasing distance from the plane for both inner and outer profiles, with factors of 1.1−1.4 and 1.4−2.4, respectively. So we can conclude that the Type-II discs produced by flares in our simulations can reproduce the global properties of real edge-on Type-II discs with low to intermediate break strengths.

4. Conclusions

The present realistic 3D models of flared disc galaxies demonstrate that, contrary to previous claims, flares can produce Type-II profiles in galaxies when viewed edge-on, especially for breaks with intermediate to low strength ($-0.25 < S < -0.05$). We also find a significant weakening of the breaks with the distance from the plane, which agrees with observations. We do not find any correlation between the existence of a significant bulge component and the presence of a Type-II break.

Acknowledgements. The authors thank to the anonymous referee for the useful criticisms that helped to improve this publication significantly and Martín López-Corredoira for his kind support with the MW models. This research has been supported by the Ministerio de Economía y Competitividad del Gobierno de España (MINECO) under project AYA2012-31277, and by the Instituto de Astrofísica de Canarias under project P3/86. We acknowledge the usage of the HyperLeda database (http://leda.univ-lyon1.fr). This research has made use of the NASA Astrophysics Data System and NASA/IPAC Extragalactic Database (NED) and the *R* environment for statistical computing.

References

Alard, C. 2000, ArXiv e-prints [arXiv:astro-ph/0007013]
Bizyaev, D. V., Kautsch, S. J., Mosenkov, A. V., et al. 2014, ApJ, 787, 24
de Grijs, R., & Peletier, R. F. 1997, A&A, 320, L21
de Jong, R. S., & van der Kruit, P. C. 1994, A&AS, 106
Erwin, P., Pohlen, M., & Beckman, J. E. 2008, AJ, 135, 20
Freeman, K. C. 1970, ApJ, 160, 811
Graham, A. W. 2001, AJ, 121, 820
Graham, A. W. 2003, AJ, 125, 3398
Hammersley, P. L., & López-Corredoira, M. 2011, A&A, 527, A6
Jester, S., Schneider, D. P., Richards, G. T., et al. 2005, AJ, 130, 873
Kalberla, P. M. W., Kerp, J., Dedes, L., & Haud, U. 2014, ApJ, 794, 90
Kregel, M., van der Kruit, P. C., & de Grijs, R. 2002, MNRAS, 334, 646
Laine, J., Laurikainen, E., Salo, H., et al. 2014, MNRAS, 441, 1992
López-Corredoira, M., & Molgó, J. 2014, A&A, 567, A106
López-Corredoira, M., Cabrera-Lavers, A., Garzón, F., & Hammersley, P. L. 2002, A&A, 394, 883
Martín-Navarro, I., Bakos, J., Trujillo, I., et al. 2012, MNRAS, 427, 1102
Minchev, I., Martig, M., Streich, D., et al. 2015, ApJ, 804, L9
Momany, Y., Zaggia, S., Gilmore, G., et al. 2006, A&A, 451, 515
Mosenkov, A. V., Sotnikova, N. Y., Reshetnikov, V. P., Bizyaev, D. V., & Kautsch, S. J. 2015, MNRAS, 451, 2376
Planck Collaboration XIII. 2015, A&A, submitted [arXiv:1502.01589]
Pohlen, M., & Trujillo, I. 2006, A&A, 454, 759
Pohlen, M., Zaroubi, S., Peletier, R. F., & Dettmar, R.-J. 2007, MNRAS, 378, 594
van der Kruit, P. C. 1979, A&AS, 38, 15
Wilkins, S. M., Gonzalez-Perez, V., Baugh, C. M., Lacey, C. G., & Zuntz, J. 2013, MNRAS, 431, 430

Appendix A

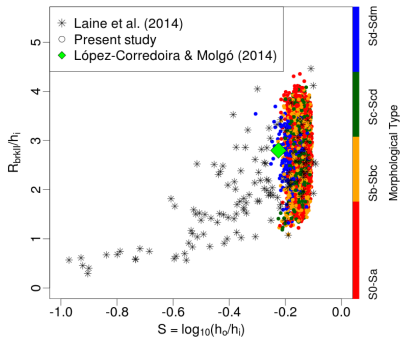

Fig. A.1. Break radius normalized by the inner disc scale length vs. the break strength S. Our simulations are plotted with coloured circles, colour-coded according to the morphological type of the object simulated. The edge-on MW model is overplotted with a green diamond. The asterisks represent the Type-II breaks observed by Laine et al. (2014) from the S^{4}G survey. See the legend in the figure.

3

Evolution of the anti-truncated stellar profiles of S0 galaxies since $z = 0.6$ in the SHARDS survey: I. Sample and methods

The probability of success is difficult to estimate;
but if we never search, the chance of success is zero.
— Philip Morrison, MIT professor

In this Chapter we continue the work presented in Borlaff et al. (2014) on the properties of antitruncated stellar profiles of S0 galaxies. We focus on S0 galaxies for two main reasons: 1) Type-III profiles are more abundant in lenticular galaxies, and 2) the surface brightness distributions of their discs are less dominated by stellar formation effects, being a more accurate proxy of the true stellar mass surface density. The main objective of Borlaff et al. (2017) is to identify a sample of Type-III S0 galaxies beyond the local Universe ($0.2 < z < 0.6$) in order to investigate if there is an evolution of the structural and photometric parameters and their scaling relations with respect to the objects of the same type at $z \sim 0$. The detailed analysis of the profiles will be presented in Chapter 4 (Borlaff et al. 2018, included in this thesis).

In order to obtain a significant sample of Type-III S0 galaxies at $0.2 < z < 0.6$ we require high spatial resolution imaging with a significant survey area. In addition, to perform a quantitative morphological classification of the initial S0 candidates, we need additional ancillary data, particularly precise measurements of the SFR and the total stellar mass of the galaxies in order to ensure that the morphological classification is correct, avoiding dust reddened spirals, for example. By doing so, we also ensure that the stellar masses of the local and the intermediate-z samples are comparable. The observations of HST/ACS in the GOODS-N cosmological field (Dickinson et al. 2003; Giavalisco et al. 2004) are excellent for this purpose. In addition, we made use of the Survey for High-z Absorption Red and Dead Sources data (SHARDS, Pérez-González

et al. 2013). The SHARDS survey obtained data in the GOODS-N field between 5000 Å and 9500 Å for galaxies down to magnitudes $m < 26.5$ AB mag, in 25 medium band filters with a full width at half maximum (FWHM) of $\sim$ 170 Å. The authors then combined all the available data in the field to analyse the spectral energy distributions (SEDs) from UV (GALEX) to NIR (Herschel). Finally, they made the stellar masses and SFRs available through the Rainbow Database (Barro et al. 2011a,b).

The analysis presented in this paper can be summarised as follows:

1. First, we selected 150 candidates of red-sequence galaxies from a $(U-V)$-$(V-J)$ colour-colour diagram (Whitaker et al. 2011, 2012), between $0.2 < z < 0.6$. We selected 150 red-sequence galaxies in this step.

2. Secondly, we made a morphological classification of the candidates based on their two-dimensional light distribution and the shape of the surface brightness profile. We found 50 S0-E/S0 galaxies within our initial red-sequence sample, 40 post-starburst objects, 32 diffuse galaxies, nine elliptical galaxies, nine objects with signs of being in interaction with others, seven "green peas" (Cardamone et al. 2009) and three spiral galaxies (see Sect. 2.2 of Borlaff et al. 2017, for more details on the morphological classification).

3. Thirdly, to avoid contamination in the outskirts of the galaxies due to the point spread function (PSF) of the mosaics (Sandin 2014, 2015), we performed two-dimensional models using `GALFIT3.0` (Peng et al. 2002, 2010) for each one of the S0-E/S0 galaxies and used the models to correct the original images for PSF effects, following the procedure described in Trujillo & Bakos (2013) and Trujillo & Fliri (2016). In order to do that, we created a hybrid PSF model for the GOODS-N images, using the core of a median stacked star (from 3D-HST, see Skelton et al. 2014) and the wings from a Tiny Tim model (Krist et al. 2011).

4. Next, we created accurate surface brightness profiles using elliptical apertures. We corrected them for Galaxy dust extinction, cosmological dimming, and K-correction.

5. Finally, we analysed the surface brightness profiles with `Elbow`, an automatic statistical method presented in this paper to determine whether a possible break is significant or not and its type. We made this method publicly available on `GitHub`[1]

We found 14 lenticular galaxies with antitruncated surface brightness profiles ($\sim$ 30 of the total sample of S0-E/S0 galaxies, similarly to the fraction found on the local Universe). This is the first sample of Type-III profiles in S0 and E/S0 galaxies at $0.2 < z < 0.6$ corrected by PSF effects. We found that one third of the Type-III surface brightness profiles were false positives due to the effect of the PSF in the outskirts of the discs. In addition, we found two galaxies with significant Type-II profiles that

[1] `Elbow:` a program for automated break analysis of disc surface brightness profiles is publicly available at GitHub (https://github.com/Borlaff/Elbow)

showed pure exponential profiles in the PSF uncorrected images. Finally, we reported that the structural parameters of the Type-III profiles at $0.2 < z < 0.6$ ($R_{\rm break}$, $h_{\rm i}$ and $h_{\rm o}$) present similar distributions to their local counterparts, while the photometric parameters ($\mu_{\rm break}$, $\mu_{0,\rm i}$ and $\mu_{0,\rm o}$) appear to be $\Delta\mu \sim 1.5$ mag arcsec^{-2} brighter than the local sample. In Borlaff et al. (2018, see Chapter 4) we investigate this apparent dimming of the stellar populations with time, taking into account the stellar masses of the samples and their colour profiles. In addition, we compare there the scaling relations of the parameters of S0 galaxies with Type-III profiles in both the local Universe and at $0.2 < z < 0.6$.

The work presented in this Chapter was published in *Astronomy & Astrophysics*, the 24th of August of 2017, in the Volume 604, with article number A119 under the title **"Evolution of the anti-truncated stellar profiles of S0 galaxies since $z = 0.6$ in the SHARDS survey I. Sample and methods"**.

Important note: Pages from 23 to 71 of the paper presented in this Chapter contain Appendices that have been moved to Chapters A, B, and C in this thesis in the benefit of clarity.

A&A 604, A119 (2017)
DOI: 10.1051/0004-6361/201630282

Astronomy & Astrophysics

Evolution of the anti-truncated stellar profiles of S0 galaxies since $z = 0.6$ in the SHARDS survey

I. Sample and methods

Alejandro Borlaff[1,2,3], M. Carmen Eliche-Moral[1,2], John E. Beckman[1,3,4], Bogdan C. Ciambur[5], Pablo G. Pérez-González[2], Guillermo Barro[6], Antonio Cava[7], and Nicolas Cardiel[2,8]

[1] Instituto de Astrofísica de Canarias, C/ Vía Láctea, 38200 La Laguna, Tenerife, Spain
e-mail: asborlaff@iac.es
[2] Departamento de Astrofísica y CC. de la Atmósfera, Universidad Complutense de Madrid, 28040 Madrid, Spain
[3] Facultad de Física, Universidad de La Laguna, Avda. Astrofísico Fco. Sánchez s/n, 38200 La Laguna, Tenerife, Spain
[4] Consejo Superior de Investigaciones Científicas, 28006 Madrid, Spain
[5] Centre for Astrophysics and Supercomputing, Swinburne University of Technology, Hawthorn, VIC 3122, Australia
[6] University of California, 501 Campbell Hall, Berkeley, CA 94720, Santa Cruz, USA
[7] Observatoire de Genève, Université de Genève, 51 Ch. des Maillettes, 1290 Versoix, Switzerland
[8] Instituto de Física de Cantabria (CSIC – Universidad de Cantabria), Avenida de los Castros s/n, 39005 Santander, Spain

Received 18 December 2016 / Accepted 14 May 2017

ABSTRACT

Context. The controversy about the origin of the structure of early-type S0–E/S0 galaxies may be due to the difficulty of comparing surface brightness profiles with different depths, photometric corrections and point spread function (PSF) effects (which are almost always ignored).
Aims. We aim to quantify the properties of Type-III (anti-truncated) discs in a sample of S0 galaxies at $0.2 < z < 0.6$. In this paper, we present the sample selection and describe in detail the methods to robustly trace the structure in their outskirts and correct for PSF effects.
Methods. We have selected and classified a sample of 150 quiescent galaxies at $0.2 < z < 0.6$ in the GOODS-N field. We performed a quantitative structural analysis of 44 S0–E/S0 galaxies. We have corrected their surface brightness profiles for PSF distortions and analysed the biases in the structural and photometric parameters when the PSF correction is not applied. Additionally, we have developed `Elbow`, an automatic statistical method to determine whether a possible break is significant – or not – and its type. We have made this method publicly available.
Results. We find 14 anti-truncated S0–E/S0 galaxies in the range $0.2 < z < 0.6$ (~30% of the final sample). This fraction is similar to the those reported in the local Universe. In our sample, ~25% of the Type-III breaks observed in PSF-uncorrected profiles are artifacts, and their profiles turn into a Type I after PSF correction. PSF effects also soften Type-II profiles. We find that the profiles of Type-I S0 and E/S0 galaxies of our sample are compatible with the inner profiles of the Type-III, in contrast with the outer profiles.
Conclusions. We have obtained the first robust and reliable sample of 14 anti-truncated S0–E/S0 galaxies beyond the local Universe, in the range $0.2 < z < 0.6$. PSF effects significantly affect the shape of the surface brightness profiles in galaxy discs even in the case of the narrow PSF of HST/ACS images, so future studies on the subject should make an effort to correct them.

Key words. methods: observational – methods: statistical – galaxies: fundamental parameters – galaxies: structure – galaxies: elliptical and lenticular, cD

1. Introduction

The origin and evolution of lenticular (or S0) galaxies is still a matter of debate. Traditionally they were classified as the natural transition between the elliptical galaxies and more complex galaxy types; spirals, in the Hubble morphological sequence (de Vaucouleurs 1959; Sandage 1961). The cause of this is that S0 galaxies usually appear without any spiral structure or signs of recent star formation in their discs. Freeman (1970) pointed out that the discs of spiral and S0 galaxies usually show surface brightness profiles that are (to first order approximation) reasonably well-fitted by an exponential function out to a certain radius, due to the stellar density decline as a function of galactocentric radius (Sérsic 1963).

Nevertheless, as deeper observations allowed the study of the outskirts of galactic discs, it was found that many lenticular galaxies do not follow a purely exponential profile along their whole observable radius (Sil'chenko 2009; Kormendy & Bender 2012; Ilyina & Sil'chenko 2012). Erwin et al. (2005) pointed out that a significant fraction of S0 galaxies present light excesses in the outskirts of the discs, which also show an exponential decline but with a shallower slope than their inner discs. Erwin et al. (2008, E08 hereafter) expanded the stellar disc classification of galaxies from Freeman (1970), according to the profile structure. Type-I discs are well modelled with a single radial exponential profile. Type-II galaxies present a down-bending profile, this is, a brightness deficit in the outer parts of the disc with respect to the extrapolated trend of the inner regions beyond a

Important note: Pages from 23 to 71 of the paper presented in this Chapter contain Appendices that have been moved to Chapters A, B, and C in this thesis in the benefit of clarity.

A&A 604, A119 (2017)

given break radius. Type-III discs becomes less steep outside the break radius than the extrapolation of the exponential trend of the inner parts (anti-truncation, see Pohlen & Trujillo 2006). E08 and Gutiérrez et al. (2011, G11 hereafter) showed that the fraction of anti-truncated discs was higher for S0 galaxies that for any other morphological type, increasing from ∼10−20% in Sc–Sd galaxies, up to ∼20−50% in S0–Sa galaxies (see also Ilyina & Sil'chenko 2012; Maltby et al. 2015). In the present study we will focus on the Type-III profiles.

A high fraction of the anti-truncated profiles are due entirely to disc structure, although ∼15% might be due to outer stellar haloes (Maltby et al. 2012). In some cases, transitions between the inner and outer profiles are associated with structural components of the galaxy such as rings or lenses (Laine et al. 2014). Some authors (e.g. Comerón et al. 2012) pointed out that these transitions might be caused by combinations of thin+thick discs with different radial scale-lengths. The role of environmental density in the formation of these structures is still a matter of debate. Some authors do not find a significant correlation between the presence of Type-III profiles and the environment (Maltby et al. 2012) while other authors do (Laine et al. 2014). A recent study (Pranger et al. 2017) found that the outer scale-lengths of both Type-II and Type-III profiles are ∼10% larger in the cluster environment compared to the field. These authors also suggest that the Type-I profiles would be an intermediate step in the transformation of Type-II into Type-III profiles. Nevertheless, Type-III profiles are ubiquitous regardless of their environment (Erwin et al. 2012; Pranger et al. 2017), and the observed suppression of Type-II profiles in the clusters argues against a common origin for both Type-II and Type-III profiles. On the contrary, this suggests that the two types of profiles are caused by completely different phenomena (Erwin et al. 2012; Roediger et al. 2012; Laine et al. 2014).

Radially varying profiles of star formation have been proposed as a cause for both Type-II and Type-III profiles (Elmegreen & Hunter 2006). However, most of the proposed mechanisms to explain Type-III profiles are based on different modes of gravitational interactions, such as close encounters (Peñarrubia et al. 2006), accretion of dark matter sub halos (Kazantzidis et al. 2009) or minor mergers (Younger & Bryan 2007). In addition, Herpich et al. (2015) also proposed radial mass redistribution as a cause for the different types of profiles due to different initial angular momentum of the host halo. Borlaff et al. (2014) tested whether major mergers can produce anti-truncated stellar profiles in S0 galaxies using hydrodynamical N-body simulations. They found that Type-III profiles of S0 remnants can be produced after a major merger event, and that those profiles obey similar scaling relations to those found in observed Type-III S0 galaxies. In a later paper, Eliche-Moral et al. (2015) reported that these relations are similar to those found in Type-III spiral galaxies, which suggests that fundamental processes must be responsible for the formation of these structures in disc galaxies along the whole Hubble Sequence. However, no study has analysed the properties of anti-truncated S0 and E/S0 galaxies beyond the local universe to learn about their possible evolution, because cosmological dimming efficiently moves these structures towards even fainter (and prohibitive) surface brightness levels.

The controversy that arises out of the comparison between different datasets may be due to the difficulty of comparing samples with different depths and surface brightness profile corrections. Measuring robust surface brightness profiles down to $\mu_{\rm lim} \sim 27-28$ mag arcsec^{-2} is a challenging task. de Jong (2008) showed that the detection of an apparent halo around the minor axis of an edge-on galaxy in the *Hubble* Ultra Deep Field can be largely explained by scattered light from the inner regions. This light spreading follows a point spread function (PSF) whose shape depends on the telescope, instrument, filter and even time (Sandin 2014, 2015). It modifies the true light distribution of the object as a convolution, "blurring" the resulting image. The PSF effect scales with the intensity of the source, and it usually becomes smaller rapidly with increasing radii. Nevertheless, the contribution of the outer wings of the PSF profile can be significant in the outskirts of galaxies, where the light intensity is very faint. This would produce apparent light emission excesses where they otherwise would not be found. Thus estimating and correcting the PSF effect is a crucial step for any study of surface brightness profiles in the outskirts of galaxies, especially when looking for Type-III profiles.

In order to estimate the surface brightness profile of an object, the observer must know the shape of the PSF out to (at least) 1.5 times the maximum size of the object in radius (Sandin 2014). To estimate precise measurements of the structural parameters of galaxies, it is not enough to simply scale the PSF profile to the central surface brightness of the profile (de Jong 2008). The observer must subtract the PSF contribution created by the whole 2D light distribution (or at least by a realistic model) not only by the innermost region but also from the outer regions of the object. Direct image deconvolution methods such as the Richardson-Lucy (Prato et al. 2012) are tempting, but inefficient (see Karabal et al. 2017, for a recent and less time-consuming method of direct deconvolution) and may lead to disruptions of the low surface brightness regions. In contrast to these, recent papers propose accurate methods for removing the PSF contribution by fitting 2D models of the galaxy taking into account the PSF (Trujillo & Fliri 2016). This method permits the derivation of reliable surface brightness profiles down to ∼31 mag arcsec^{-2}, according to these authors. In the present work we will follow a similar procedure, even though our profiles are limited to radii where the profiles are 3−4 mag arcsec^{-2} brighter, where the effects of the PSF are less significant.

In order to shed light on the evolution of these structures, we have selected a sample of galaxies from the red sequence and then we have identified the S0 and E/S0 galaxies at $0.2 < z < 0.6$ by studying their star formation rate, morphology and analysing their surface brightness profiles. We have quantified the properties of Type-III discs in this sample and compared them to the Type-III profiles from the samples at $z \simeq 0$. In this paper, we present the sample selection and describe in detail the statistical methods to trace the structure in their outskirts and correct for PSF effects. We will analyse the scaling relations at $0.2 < z < 0.6$ and compare them with their local counterparts in a forthcoming paper (Borlaff et al., in prep.).

The outline of this paper is as follows. The method is described in detail in Sect. 2. The results are presented and discussed in Sect. 3. The final conclusions can be found in Sect. 4. We tabulate the general properties of the initial red galaxy sample in Appendix A. Appendix B contains the profile classifications for the S0 – E/S0 sample and their structural and photometric parameters. Appendix C describes the final sample of anti-truncated S0 and E/S0 galaxies individually and shows the RGB images used for the morphological classification as well as the decompositions performed to the profiles. We assume a concordant cosmology ($\Omega_{\rm M} = 0.3, \Omega_{\Lambda} = 0.7, H_0 = 70$ km s^{-1} Mpc^{-1}, see Spergel et al. 2007). All magnitudes are in the AB system unless otherwise noted.

2. Methods

In order to study the properties of the surface brightness profiles of non-local S0 – E/S0 galaxies in the GOODS-N field at $z < 0.6$, first we had to create a sample of quiescent candidates, that must include S0 and E/S0 galaxies, by definition. The data used are presented in Sect. 2.1 and the selection of a sample of quiescent candidates with $z < 0.6$ is described in Sect. 2.2. Secondly, we performed a visual morphological classification based on the data available for the selected objects (2D structure, presence of AGN activity, star formation rate (SFR), total stellar mass and surface brightness profile), as described in Sects. 2.2 and 2.8. Thirdly, we modelled each object and corrected any possible PSF contributions to the surface brightness profiles. After this, we estimated the necessary corrections for dust extinction, cosmological dimming and K-correction for each S0 and E/S0 object (Sects. 2.5). This is explained in detail in Sects. 2.3–2.4 and 2.7. Finally, we performed the identification, characterisation and analysis of the structure of the components in the surface brightness profiles as described in Sect. 2.6. The efficiency and reliability of the PSF correction performed to the galaxies in our sample is checked in Sect. 2.7.

2.1. Data description

2.1.1. SHARDS and the Rainbow database

The Survey for High-z Absorption Red and Dead Sources (SHARDS, Pérez-González et al. 2013) is an ESO/GTC Large Program carried out with the OSIRIS instrument on the 10.4 m Gran Telescopio Canarias (GTC). This survey obtained data between 5000 Å and 9500 Å for galaxies in the GOODS-N field down to magnitudes $m < 26.5$ AB mag, in 25 medium band filters with a full width at half maximum (FWHM) of ∼170 Å. The main goal of this survey was to study the properties of stellar populations of massive galaxies in quiescent evolution at $z = 1.0$–2.3 through the pseudospectra resulting from the data of this photometric medium band filter system (the set is equivalent to low resolution integral field spectroscopy, $R \sim 50$) and deep ancillary broad-band data. The wavelengths include key absorption indexes such as Mg(UV) ($\lambda \sim 2800$ Å), essential for the study of high-z early-type galaxies. This technique allowed the SHARDS team to select quiescent objects, calculate star formation histories (SFH) and photometric redshifts with a precision better than $\Delta z/(1+z) \sim 0.007$ (Domínguez Sánchez et al. 2016). See Pérez-González et al. (2013) for a detailed description.

SHARDS data are available through the Rainbow Database (Barro et al. 2011a,b) in compilation with multiple photometric and spectroscopic data for several cosmological fields, such as GOODS-N and GOODS-S, COSMOS, or the Extended Groth Strip. The authors used all the available photometry to build spectral energy distributions (SEDs) from X-ray to radio. Using the SED fitting procedure, they derived photometric redshifts and estimates of parameters such as the stellar mass, the UV- and IR-based SFRs, the stellar population age and rest-frame magnitudes in different filters (Pérez-González et al. 2005, 2008, 2013).

In this study, we have selected a sample of GOODS-N galaxies included in the SHARDS survey, that: 1) have low star formation rates, compatible with being early-type galaxies; 2) have total stellar masses similar to those of the available local samples ($M \sim 10^9$–$10^{11}\ M_\odot$), and 3) have morphologies compatible with being S0 – E/S0 objects. We restricted the selection only to the objects with reliable SHARDS data because: 1) we wanted to ensure that the S0 and E/S0 galaxies included in the sample are really quiescent and have stellar masses comparable with the local sample; and 2) we aimed to create a sample of anti-truncated S0 and E/S0 galaxies that can be used in a forthcoming study to investigate the properties of the stellar populations, metallicities and star formation rates of their inner and outer profiles. We have used SHARDS data release 2 in the database (iDR2beta).

2.1.2. HST/ACS data in the GOODS-N field

We have derived, corrected and analysed the surface brightness profiles using the deepest images available in our dataset tracing the rest-frame V and R bands, that is, those in the *F775W* band of HST/ACS. The GOODS-N field is a large cosmological field with HST/ACS imaging centred on the *Hubble* Deep Field North (Dickinson et al. 2003). The spatial resolution of these images is 0.06 arcsec/px and the 1σ fluctuation level of the surface brightness on a area of 1 arcsec^2 is 27.7 mag. The average FWHM for the *F775W* filter mosaic is 0.11 arcsec (Skelton et al. 2014, see Table 6). In order to derive the surface brightness profiles for the SHARDS objects, we relied on the ACS *F775W* mosaic from the ACS V2.0 data release (HST Cycle 11, programme IDs 9425 and 9583, Giavalisco et al. 2004) available at the 3D-HST project webpage[1] (Skelton et al. 2014). The zeropoints of the images are available in Table 6 of Skelton et al., such that:

$$\mu_{F775W} = -2.5 \cdot \log_{10}(\mathrm{counts/area}) + 25.671. \quad (1)$$

The reduction process of the raw data was performed by using the CALACS software, available at the Space Telescope Science Institute site (Pavlovsky et al. 1999). This pipeline accounts for the bias subtraction, gain correction, and flat-fielding correction of each individual exposure. The corrected (flt.fits) individual images were then drizzled to the final mosaic through the Multidrizzle software package (Koekemoer et al. 2003), and corrected for geometric distortion at the same time, removing cosmic-rays and performing sky-subtraction. For more details on the process of reduction and the data, we refer the reader to Giavalisco et al. (2004).

We set the upper limit on redshift for the initial sample at $z = 0.6$, in order to cover; with the *F775W* filter from HST/ACS, a similar wavelength range as the local universe observations we wanted to compare with (usually, in the V or R bands). This band traces similar wavelengths as the R band from $z = 0.1$ to $z \sim 0.3$ and is equivalent to *F606W* (tracing approximately V) between $z = 0.2$ and $z = 0.6$. Thus, we selected the initial sample within $0.2 < z < 0.6$. In order to compare the surface brightness profiles between the local sample and ours, we also performed a photometric K-correction to our data to transform them into the rest-frame R filter (see Sect. 2.5).

2.2. Red sample selection and morphological classification

In the local universe and beyond, galaxies are divided into two main classes: star-forming galaxies and quiescent galaxies (van Dokkum et al. 2000; Willmer et al. 2006; Kodama et al. 2007; Williams et al. 2009; Brammer et al. 2011; Whitaker et al. 2011). These two populations of galaxies show very different distributions in rest-frame colour-magnitude diagrams: quiescent galaxies usually have high luminosities and red colours while the star-forming galaxies present lower luminosities and

[1] 3D-HST – A Spectroscopic Galaxy Evolution Survey with the *Hubble* Space Telescope: http://3dhst.research.yale.edu/Home.html

A&A 604, A119 (2017)

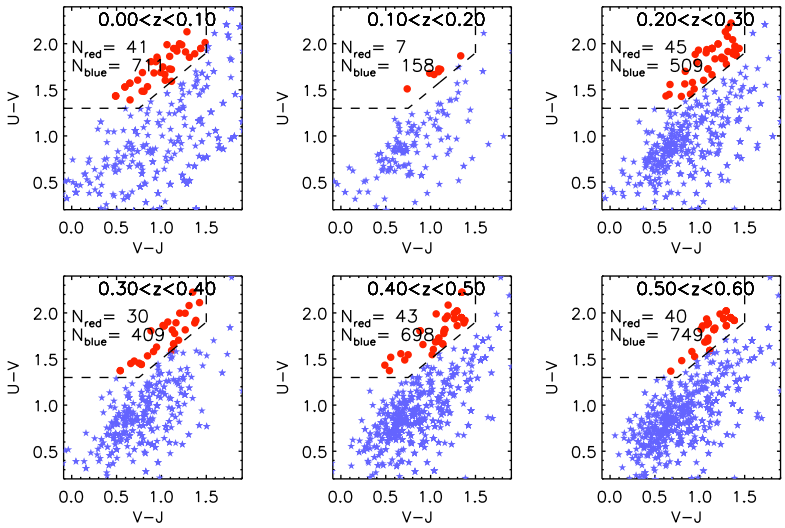

Fig. 1. Initial sample selection with the $(U-V)$ vs. $(V-J)$ colour-colour diagram by redshift intervals up to $z = 0.6$. Dashed line: Whitaker et al. (2011, 2012) boundaries for identifying the quiescent galaxy population and the star-forming galaxies (see Eqs. (2)–(4)). Red dots: quiescent galaxies from the initial SHARDS sample. Blue stars: star-forming galaxies from the initial SHARDS sample. The number of objects selected in each class and interval of redshift are given on the panels.

bluer colours. This means that the two populations of galaxies appear as two well separated sequences in the $(U-V)$ vs. $(V-J)$ colour-colour diagram, so we can select a quiescent sample (that includes S0 and E/S0 galaxies, in which we are interested) by using the following boundary-relations (Whitaker et al. 2011, 2012):

$$U - V > 0.8 \times (V - J) + 0.7 \quad (2)$$

$$U - V > 1.3 \quad (3)$$

$$V - J < 1.5. \quad (4)$$

The galaxies selected within these boundaries present very red colours, either because they depleted their gas reservoir and cannot create new stars or because they are extremely extinguished by interstellar dust. We selected all sources from the GOODS-N field in the SHARDS catalogue (excluding those classified as stars) which present redshifts $0.2 < z < 0.6$, and we have used the previous boundaries in the colour-colour diagram to select those in the red sequence. We have excluded objects with $z < 0.2$ in the catalogue because of the high uncertainties detected in the estimates of the photometric redshifts at these distances (Barro et al. 2011b). In addition to this, we used visual morphology classification as well as near-IR (NIR) and UV SFR to prevent reddened spiral and irregular galaxies from being included in the sample of quiescent galaxies (see Sect. 3.2). In Fig. 1 we show an example of this first selection process. Rest-frame U, V and J magnitudes as well as the redshifts and stellar masses were taken from the Rainbow Database (see Sect. 2.1.1). The panel shows those SHARDS objects within the red sample according to the criteria outlined previously. With blue stars, we represent the discarded objects. For the sake of completeness we show the diagrams corresponding to the interval $z = [0, 0.6]$ with $\Delta z = 0.1$. We removed eight objects with $0.2 < z < 0.6$: seven of them were artifacts and spurious detections (SHARDS10007608, SHARDS10009632, SHARDS10012462, SHARDS10012556, SHARDS20013873, SHARDS20001446 and SHARDS20009949) and one object was clearly affected by nearby star contamination (SHARDS20008526). Finally we identified 150 objects as "red" (mostly quiescent, as we will show in Sect. 3.2) in total between $0.2 < z < 0.6$. The sample presents median value of $z = 0.41$. We note that ∼75% of the objects have $z > 0.27$. The red objects in our sample and their main properties (coordinates, morphological type, photometric and spectroscopic redshifts, stellar mass, SFR, rest-frame absolute K and V magnitudes, extinction and K-correction for the *F775W* filter) are provided in Table A.1.

We have performed a visual morphological classification of the objects based on the HST/ACS images in the *F435W*, *F606W* and *F775W* bands, and a false colour combined image of these three ones. In Fig. 2 we present a summary of the morphological classification process by showing the available information of one object of each morphological class that we have considered, which we describe below. From left to right, the first three columns represent the images of each object in the three filters used for this analysis: *F435W*, *F606W* and *F775W*. We used the *F435W* filter to detect possible star formation regions that may not be detectable in the other redder filters. This allowed us to

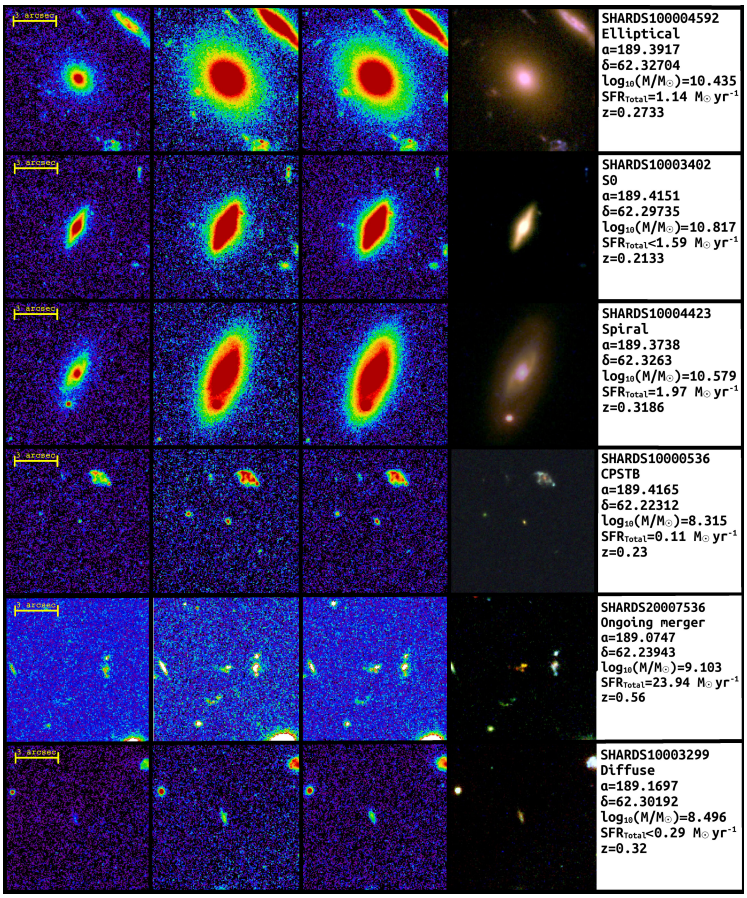

Fig. 2. *F435W*, *F606W* and *F775W* images of some objects from the initial selected red sample, used for the morphological classification. *Columns, from left to right:* 1) *F435W* image; 2) *F606W* image; 3) *F775W* image; 4) RGB colour image, using the previous filters for the blue, green and red colours, respectively; 5) information panel with the identifier of the object in the SHARDS data release 2, position (α, δ), total stellar mass, SFR and z.

discard from the red sample the dust-reddened spirals that had not been rejected using the colour-colour criteria, or contamination sources which were very bright in the bluer bands but difficult to identify in the redder bands, such as small satellites, tidal tails or minor mergers in the outskirts of the objects. The RGB images shown in the fourth column were created by the combination of the previous three filters. These RGB images were used for the morphological classification, together with the individual filter images. In addition, preliminary surface brightness profiles (i.e, without PSF correction) as well as some characteristic parameters of each object (see the right column of Fig. 2) were used for the classification process. The images used during the classification presented a field-of-view (FoV, hereafter) of $7\times R_{\rm kr}$ were $R_{\rm kr}$ is the Kron radius (Kron 1980) of the object (available from

A&A 604, A119 (2017)

the Rainbow Database, see Sect. 2.1.1). It was defined in this way to show a sufficient portion of the surrounding areas around the object to identify possible interactions, close companions or sources of diffuse light contamination.

We classified the objects of the initially selected red sample morphologically according to the following criteria (see an example of each morphological type in Fig. 2):

– A. Morphological types assigned to well-resolved galaxies:

1. *Elliptical galaxies (E)*: they do not present any signs of a disc component, but a smooth light distribution surrounding a bright compact core with very low ellipticity. The surface brightness profiles usually decrease with a steeper and non-constant slope when compared to an exponential profile. The surface brightness profiles are usually well-fitted with a single Sérsic profile with index $n \sim 3-5$. They do not show appreciable star formation signs, bars, or spiral arms.
2. *S0 – E/S0 galaxies*: they show a noticeable disc component with a smooth light distribution, without any signs of spiral structure or star-forming regions. For those objects where the dominant component is the disc, we have assigned the S0 classification. On the contrary, the objects with a dominant central bulge or halo were classified as E/S0. Some S0 galaxies at low inclination may be mistaken for elliptical galaxies in the visual classification. To avoid contamination between the types, we refined our visual classification by using the surface brightness profiles and the multi-component `GALFIT3.0` analysis, as detailed in Sect. 2.3.
3. *Spiral galaxies (Sp)*: they present a disc component and a spiral pattern with clear star-forming regions detected in the *F435W* band.
4. *Ongoing mergers (OM)*: these objects present highly irregular and distorted light distributions in the images. The progenitors can still be identified separately. Close pairs without clear signs of tidal interaction were not included in this category and we have classified them as two independent galaxies.

– B. Morphological types associated with low signal-to-noise ratio (S/N) or low resolution data:

1. *Compact post-starbursts (CPSTB) and green peas (GP)*: these are very compact objects. The spatial resolution is not enough to resolve their structure or different components. Some of these objects present recent merger signs. The CPSTBs present extremely red colours, possibly caused by extreme dust extinction. In contrast, the GPs usually present green colours in the false RGB images used to classify them. We adopted the green peas nomenclature following Cardamone et al. (2009), but in order to confirm the objects within this class as real GPs according to their definition we would require specific observations, which are beyond the scope of this paper.
2. *Diffuse galaxies (DF)*: we classify as diffuse galaxies those objects with very low S/N ratio, usually with elongated morphologies. Faint spirals or interacting disc galaxies are possible candidates to appear as diffuse galaxies. They fall into the red sequence probably because of dust extinction. The surface brightness profiles are too faint and noisy due to the low apparent luminosities.

As explained before, S0 galaxies can be confused with elliptical galaxies, especially those at low inclination. The discs of spiral and S0 galaxies usually show surface brightness profiles that follow an exponential law (Freeman 1970) out to a certain radius. In contrast, elliptical galaxies show a steeper surface brightness decline, usually well fitted by a $n \sim 4$ Sérsic profile (i.e. a de Vaucouleurs profile). We exploited these structural characteristics to distinguish S0 from E galaxies even at low inclination. Thus, for the elliptical, S0 and E/S0 galaxies identified visually, we refined the morphological classification using the surface brightness profiles, as well as the 2D decomposition, to ensure that we are not including elliptical objects in the final S0 – E/S0 sample (see Sect. 2.3). We found 50 S0 and E/S0 galaxies within our initial sample of 150 red galaxies (38 S0 and 12 E/S0). We could correct for PSF effects 44 out of these 50 S0 and E/S0 galaxies, as explained in Sect. 2.3. The remaining objects were removed from the final sample because they did not present stable bulge+disc 2D decompositions (SHARDS10001928, SHARDS10002901, SHARDS10005029, SHARDS10008552, SHARDS20000858 and SHARDS20004273). The morphologies of our red galaxy sample and their global properties are described in detail in Sects. 3.1 and 3.2. The final morphological classification for all objects in our red sample is provided in Table A.1. The RGB images of the objects finally classified as S0 and E/S0 that could be corrected for PSF effects are provided in Appendix C.

2.3. GALFIT modelling and PSF correction

In order to estimate and correct the amount of dispersed light by the PSF in the HST/ACS images, especially in the outskirts of the galaxies, we cannot simply perform a numerical deconvolution of the image, because it would affect the light distribution in the low surface brightness region (see Sect. 1). We have followed a similar procedure to that presented in Trujillo & Bakos (2013).

First, we performed careful masking in all the images, in order to avoid contamination by foreground objects, non-symmetric components such as satellites, compact bright regions or close stars or their PSF spikes. We created these masks in two steps. We performed an automatic masking by using SExtractor (Bertin & Arnouts 1996), which is later manually checked. We manually extended the masks of the largest foreground objects with circular masks in order to prevent the scattered light from contaminating the surface brightness profiles of the galaxies. We estimated the limits of each manual masking by analysing the isophotal map on smoothed images. We gradually increased the smoothing kernel from two up to eight to ten pixels, checking on each step the possible features that appeared. By using the isophotal contours, we checked the possible distortions due to contamination sources or extreme changes in the position angle and ellipticity in each object. Finally we used the masked images (centred on each object, with a FoV of 100×100 arcsec) to measure individually the sky noise distribution, which defines for each object the limiting magnitude of the profile. See some examples of isophotal maps and masked regions in the figures of Appendix C. The effects of PSF correction on the resulting profiles are analysed in Sect. 3.5.

We used `GALFIT3.0` (Peng et al. 2002) to fit two sets of models for each object within our sample of 50 S0 and E/S0 galaxies: a single free Sérsic model and a free Sérsic model + exponential profile. In this step, we discarded from the S0 and E/S0 sample those objects which: 1) cannot be fitted with a stable model, due to small size or irregularities; 2) are well fitted with a single (high n) Sérsic profile, so the profile corresponds to

an elliptical galaxy rather than an E/S0 or S0 (see Sect. 2.2); or 3) do not drastically reduce the residuals of the fit by adding a second component to the first one. This revision was performed individually by three co-authors, checking the differences between the modelled and the original profiles. In this phase we distinguished between the elliptical galaxies from face-on S0 galaxies by analysing their surface brightness profiles. In order to do that, we have estimated for all the objects two different 2D decompositions: 1) using a single Sérsic profile and 2) with a Sérsic bulge + exponential disc profile. We note that each 2D decomposition implies a different PSF deconvolution. We analysed the residual profile of each object, and identified those which do not drastically improve with the addition of a disc component and present a smooth decrease of the slope with the galactocentric radius. Finally we confirmed that the nine objects that visually presented elliptical morphologies really were ellipticals according to their surface brightness profiles. We show the surface brightness profiles, with the corresponding models and residual profiles, for the S0 and E/S0 galaxies with successful PSF correction in Appendix C.

We have estimated the errors of the parameters of each model by performing Monte Carlo simulations over the original images, varying each pixel value within the noise level and fitting sequentially. We note that we assume 1, 2 and 3σ limits as those values that enclose 68%, 95% and 99.7% of the probability distribution of the sample. In the case of the noise level of our images the sample are the sky-dominated pixels. We define as sky-dominated pixels any pixel that was not identified as part of a source in the masks generated before to create the `GALFIT3.0` models and the surface brightness profiles. We estimated the noise level as the upper 1σ fluctuation of the sky background distribution. This value is equivalent to the standard deviation if we assume that the sky background follows a nearly Gaussian distribution with a mean of zero and dispersion equal to the measured noise level. By providing `GALFIT3.0` a PSF model for the image, the programme tries to fit the best model that, after convolution with the PSF, matches the original image. This allows us to estimate the amount of diffuse light scattered into the outskirts of the image. We estimate the deconvolved image through the following image operation:

$$\text{Residuals} = \text{Image raw} - \text{PSF} * \text{Model}_{\text{GALFIT}}. \quad (5)$$

$$\text{Deconvolved final image} = \text{Model}_{\text{GALFIT}} + \text{Residuals}. \quad (6)$$

The 3DHST team provides a star-stacked PSF, but the model size is very small for our purposes (~4 arcsec in diameter) while we need at least a ~25 arcsec diameter PSF to perform any kind of PSF subtraction (Sandin 2014, 2015). Otherwise, the reconvolved model (i.e., the fitted PSF-free model, again convolved by the PSF) would systematically underestimate the amount of dispersed light at radii larger than half the diameter of the PSF. This limit in size was calculated by multiple iterations in the surface brightness profile fitting, and roughly corresponds to 1.5 times the limiting radius at $S/N = 3$ in the surface brightness profiles of the larger galaxies in our sample. We show an example of the deconvolution and modelling in Fig. 3. In the top panel, we represent the surface brightness profiles of the original and PSF-corrected image, as well as the profiles of the models used for the deconvolution. We note that the deconvolved profile is systematically biased towards brighter magnitudes in the centre and dimmer magnitudes in the outskirts. This effect is clear in the bottom panel, where we show the differences between the original and the PSF-corrected profiles (red dots). We also note that the original and reconvolved profile (black squares) are nearly

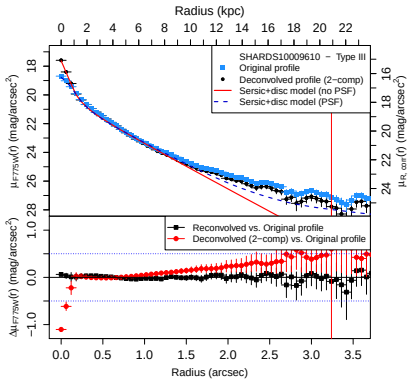

Fig. 3. *Top panel*: surface brightness profiles of the Type-III S0 galaxy SHARDS10009610. Blue squares: surface brightness profile of the original image. Black dots: the same for the PSF-corrected image (black). We represent the magnitude scale for the observed *F775W* band (*left axis*) and for the rest-frame *R* band (*right axis*). The red solid and blue dashed lines correspond to the models fitted during the deconvolution and used for checking the visual morphological selection (see the legend). *Bottom panel*: residuals between the original and corrected profiles. Red circles: difference between the original and the PSF-corrected profiles. We note that the PSF effects create a systematic upturn beyond ~1.0 arcsec. Black squares: difference between the original profile and the reconvolved PSF-corrected image profile. The vertical red line represents the limiting radius.

identical along the whole profile, showing that the PSF correction and the fit are adequate, under the assumption that the PSF model is robust and realistic (we demonstrate this in Fig. 4, see below).

GOODS-N is an extremely star-clean field, so PSF modelling using star stacking may lead to noisy and biased distributions in the outskirts of the profiles due to the lack of bright stars in the field. Instead, we have created a model of the PSF using the Tiny Tim software (Krist et al. 2011) for the PSF outskirts, combined with a GOODS-N stacked star PSF for the inner regions of the PSF provided by 3DHST. Tiny Tim is a modelling tool for generating HST model PSFs for multiple cameras and filters. The synthetic PSFs generated by Tiny Tim have been previously used in similar studies (See de Jong 2008; Trujillo & Bakos 2013). GOODS-N has a covering grid of 3×5 individual ACS pointings, with some overlap to check the photometric and astrometry consistency between individual pointings. There is a rotation of the field of 45º between the odd-numbered epochs and the even-numbered epochs. In order to approximate the effect of the combination of rotated images in the final mosaic, we combined two Tiny Tim PSF model images of 29 arcsec in diameter, rotated 45º degrees (Trujillo & Fliri 2016). After that, the centre of the resulting PSF model was replaced by the natural star PSF model of 3DHST, which is reliable only out to 4 arcsec. We measure a FWHM of our combined PSF model is 0.09 arcsec. As mentioned in Sect. 2.1.2, in Skelton et al. (2014) (see Table 6), the authors report an average FWHM of 0.11 arcsec for the *F775W* band mosaic of GOODS-N.

A&A 604, A119 (2017)

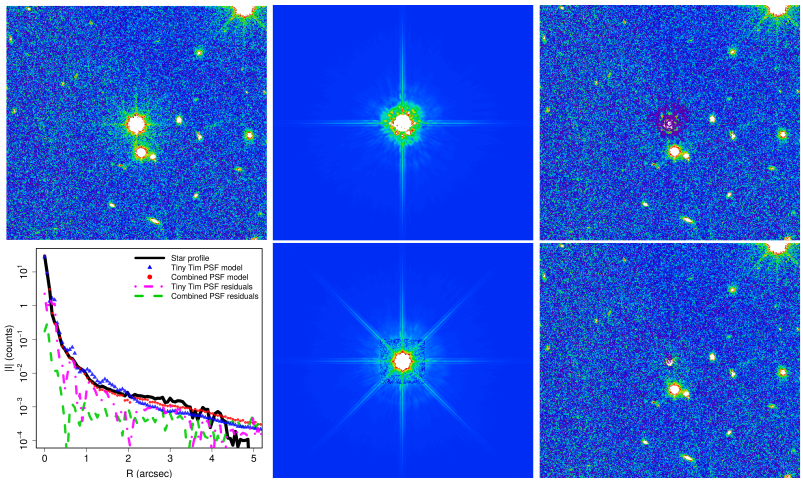

Fig. 4. Comparison of the subtraction of a star with `GALFIT3.0`, using a 15 arcsec Tiny Tim PSF (*upper row*) and our combined PSF (*lower row*). *Top left panel*: *F775W* image of a star. *Bottom left panel*: intensity profiles for the star, the PSF models and the residual images after the subtraction of the Tiny Tim PSF and after the subtraction using our combined PSF (see the legend for details). *Middle column*: PSF scaled models for the Tiny Tim model (*top*) and the combined PSF (*bottom*). *Right column*: residuals of the subtraction for the Tiny Tim model (*top*) and the combined PSF (*bottom*). We note that the residuals for the wings in case of using our combined PSF are smaller at all radii than those resulting from using the Tiny Tim PSF, despite the common central underestimate. The FoV of all the images is 24×24 arcsec^2. All images are in the same colour scale.

In Fig. 4 we show a quality test to show that our PSF model is robust and realistic. The upper panels show the test using a standard PSF created by Tiny Tim for the *F775W* filter, whereas the lower panels show the test using our combined PSF. We have fitted each PSF to a well-centred field star in the GOODS-N image, using `GALFIT3.0`. The residuals of the two cases are shown in the right panels, and the residuals profile in the bottom left panel. We find that our combined PSF model significantly reduces the residuals of the PSF modelling of the star when compared to the original Tiny Tim model. The success of the subtraction is significant especially for the intermediate and external parts where the characteristic spikes and rings of the HST PSF are removed almost completely. In addition, the remaining residuals in the centre do not show circular symmetry, which would introduce contamination in our azimuthally averaged profiles.

Additionally, in order to test on each object the validity of the PSF-deconvolved model obtained, we again convolve the PSF-deconvolved image by the PSF model (or reconvolved image), and compute the differences between the surface brightness profiles derived from the original and reconvolved images. We found that the differences between the original and the reconvolved profiles were less than 1σ in the surface brightness profiles up to the limiting radius in each case. Thus, we concluded that the applied PSF correction is robust and self-consistent.

2.4. Surface brightness profiles

We derived the surface brightness profiles by two different methods, depending on the inclination of the object. For the low inclined objects we relied on the `ellipse` task from IRAF. We fixed the position angle and ellipticity of the ellipses to the mean values obtained with SExtractor in the galaxy disc on the original image, with the limiting threshold set at 1σ. By doing so, we avoid unstable solutions for the position angle and ellipticity, especially common in the outskirts, where the S/N ratio is low (see E08) and where we will be centring our attention. As a side effect, the innermost parts of the profiles (the first five or six pixels in radius) may be slightly biased towards lower values, but we discarded this region in the vast majority of the cases, so it does not affect our results. On the other hand, the nearly edge-on objects were analysed by using `ISOFIT` (Ciambur 2015). This task replaces the angular parameter that defines quasi-elliptical isophotes in polar coordinates for the eccentric anomaly. By doing this, `ISOFIT` provides more accurate modelling of galaxies with non-elliptical shapes, such as disc galaxies viewed edge-on, and thus recovers more accurate surface brightness profiles. We have used free position angle and ellipticity in this case.

In order to separate the edge-on objects from the rest of the sample, we have used the results from the 2D decomposition models performed previously for the deconvolution process. The Monte Carlo simulations that we performed on the `GALFIT3.0` models provide the probability distribution for the axis ratio ($q = b/a$) of the disc component. We assumed an intrinsic axis ratio for the S0 galaxies of $q_0 \sim 0.25$ (Weijmans et al. 2014), with the exception of those objects with $q < 0.25$ where we used $q_0 = 0.1$, which is the lower limit of the q_0 distribution from Weijmans et al. (2014). We note that we apply this ratio only as a median value in order to

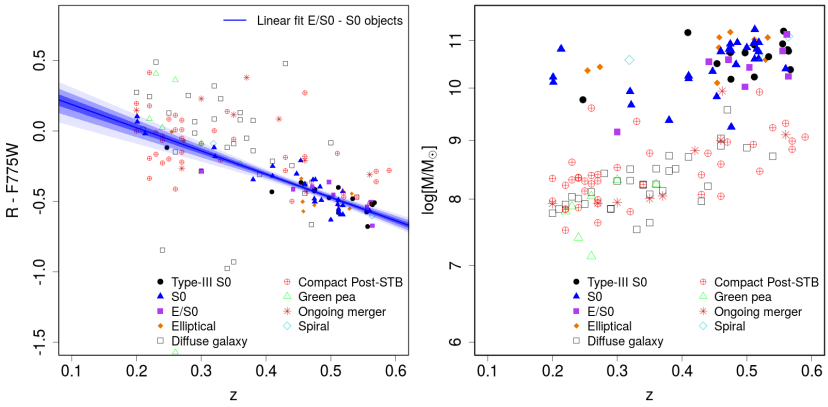

Fig. 5. *Left panel*: estimated K-correction for the *F775W* filters to the *R* band as a function of z. It is important to highlight that the linear fit applies to the observed correlation of the S0 and E/S0 galaxies of the sample. The intensity levels of the linear fit represent the 1, 2 and 3σ confidence regions of the fit. *Right panel*: stellar mass for the initial red sequence sample vs. z. Consult the legend in the figure for the morphological classification.

select objects with high inclinations, and it is not used to extract conclusions for single objects. The values of the inclination angle for each object are included in Table B.1. The median dispersion for these values are ±3 degrees. We identify five objects with $q_0 < 0.25$ as nearly edge-on galaxies (SHARDS10000845, SHARDS10001727, SHARDS20000827, SHARDS20003134 and SHARDS20011817). In addition to these, after visual classification, we added SHARDS10002351 and SHARDS10003402 to the edge-on sample. For them, the surface brightness profiles have been derived with `ISOFIT` instead of `ellipse`, as commented above.

We defined the outer limit of the profile on the major axis as the outermost elliptical bin with an integrated intensity with $S/N > 3$. The 1σ sky noise level was defined for each azimuthal bin as

$$\sigma_{\rm sky,bin} = \frac{\sigma_{\rm sky,pixel}}{\sqrt{N}} \quad (7)$$

where $\sigma_{\rm sky,pixel}$ represents the standard deviation of the background, measured on the masked images and N is the number of pixels included in each radial bin. The sky noise for each ellipse is then combined by addition in quadrature with the intrinsic dispersion along the azimuthal direction for each ellipse. The upper and lower limits of the magnitude values have been calculated by performing Monte Carlo simulations of the final noise distribution for each bin. The median limiting magnitude for our profiles is $\mu_{F775W,\rm lim} = 27.092^{+0.024}_{-0.032}$ mag arcsec^{-2} (the uncertainties refer to the percentiles 84.1 and 15.6, equivalent to ±1σ in a Gaussian distribution).

2.5. Photometric corrections

The rest-frame wavelength range for a filter varies as a function of z, so we need to apply a K-correction (Humason et al. 1956; Oke & Sandage 1968) to the photometry of our profiles. We have performed the K-correction directly by estimating the variation of the colour between the apparent magnitude estimated from the fitted SED in the rest-frame filter we want to compare with (*R* band) and the observed magnitude in the *F775W* filter. The rest frame (synthetic) *R* and the observed *F775W* apparent magnitudes for each object of our sample are available at the Rainbow Database. Rest-frame magnitudes have been calculated by direct integration over the best-fit SED for each object (Pérez-González et al. 2013). In the left panel of Fig. 5 we show the K-correction derived for the S0 and E/S0 galaxies of our sample, as a function of z. It nearly follows a linear relation for S0 and E/S0 galaxies, which we have fitted by using 10 000 bootstrapping simulations of a least squares fit, resulting in:

$$R - F775W = 0.340^{+0.033}_{-0.042} - 1.619^{+0.065}_{-0.072} \cdot z, \quad (8)$$

with a Spearman correlation coefficient of $\rho = -0.838$, and a Pearson test probability $p < 2.2 \times 10^{-16}$. We calculate the K-corrections for each object by using the previous linear relation, which applies a median correction as a function of z. The final K-corrections for each object are shown in Table A.1 in Appendix 4 (the median uncertainty for $R-F775W$ is ±0.060). Therefore, the final surface brightness profiles of our $0.2 < z < 0.6$ sample are in the rest-frame *R* band, as the available data on local Type-III S0s by E08 and G11.

In order to check the goodness of the Rainbow photometric redshift for our subsample of S0 and E/S0 galaxies at $0.2 < z < 0.6$, we have estimated the difference between the spectroscopic and the photometric redshifts for those objects where the former is available (47 out of the selected 50 S0 and E/S0 galaxies have spectroscopic redshift). We found an excellent overall agreement between the spectroscopic z and the photometric z with a median dispersion in our subsample of $\Delta z/(1+z) = 0.0024$, meaning that the photometric z estimated in Rainbow from SED fitting are very good for the galaxies of our sample. A notable exception is the object SHARDS10000845 ($z_{\rm photo} = 0.36$, but

A&A 604, A119 (2017)

$z_{spec} = 0.5123$). The spectroscopic redshift flag at the Rainbow Database is four, which means a very reliable value for z_{spec}. Nevertheless, this discrepancy does not affect the results, as the z_{spec} was used instead of the z_{photo} result in all the calculations when available. Only three S0 – E/S0 galaxies did not present available z_{spec} values (SHARDS10005029, SHARDS10008552 and SHARDS20011817). However, the two first cases were removed from the final sample (see the reasons in Sect. 2.2) and the last was finally classified as an S0 galaxy with a Type-I profile.

We corrected our profiles for Milky Way dust extinction too. To estimate the necessary corrections, we used the dust reddening maps from Schlegel et al. (1998), available through the NASA/IPAC Infrared Science Archive[2]. We extracted the extinction factor $E(B-V)$ for each object at its position. We assumed a Landolt V band extinction in magnitudes $A_V = 3.315 \times E(B-V)$, and the ratio $A_{F775W}/A_V = 0.65$ (Fitzpatrick 1999; Indebetouw et al. 2005). We corrected for the calculated extinction correction for each object in the sample. The values obtained are available in Table A.1.

Finally, we have corrected the profile for cosmological dimming, which entails a factor $\Delta\mu = -10 \times \log_{10}(1+z)$. We use the best z value for each object available in the Rainbow Database to perform this correction (see Table A.1).

2.6. Elbow: automated break analysis of disc surface brightness profiles

After the surface brightness profile calculation, we proceeded to classify the profiles into the three types described in Sect. 1, paying special attention to those objects showing a Type-III profile. We have performed this classification using two procedures: 1) simple visual classification and 2) an automated break analysis via an algorithm written by us in R[3] (R Core Team 2016) that we called `Elbow`. `Elbow` accepts as input the surface brightness profile and the errors in both magnitude and position of each bin, as well as minimum and maximum radial limits for the analysis. The tasks of the programme are: 1) to estimate the best double exponential fit to a surface brightness profile and 2) to calculate the probability that the slopes of the inner and outer fitted profiles are statistically different. The algorithm works by carrying out Monte Carlo + bootstrapping simulations on the input profile, using the uncertainties provided by the user for each data point in both radius and magnitude. This is a two-step process. First, for each simulation, `Elbow` generates a new profile by random re-sampling with replacement (bootstrapping). This implies that the new profile contains the same number of points as the original one, but some points are not included in each simulation. Secondly, we replace each data point with the values from a Gaussian distribution with a mean value equal to the original data point and σ equal to the original error (Monte Carlo). This is done for both variables (r and μ). We take advantage of the combination of the bootstrapping and Monte Carlo methods in order to take into account the different uncertainties associated to each point and obtain an accurate probability distribution of the parameters at the same time. One of the main benefits of the re-sampling methods is to avoid any assumptions of normality on the sample and hence obtain a more accurate distribution for certain statistics. In addition, the shape of the resulting probability distributions for the parameters give us information about the presence of outliers and irregularities. This method of fitting breaks in linear trends via bootstrapping was already tested in Cardiel et al. (1998) to detect changes in the slope of the line-strength gradients of Mg_2 and the λ4000 Å break as a function of the galactocentric radius in central cluster galaxies, and more recently by Marino et al. (2016) to detect breaks in surface brightness profiles.

We have avoided the inner parts of the profile – which are dominated by the bulge emission – by using the bulge model fitted with the `GALFIT3.0` and removing from the fit the section of the profile where the bulge dominates the emission over the exponential profile. For several objects this minimum limit was not enough to properly mask the central part of the profile (because of additional inner components), and it had to be set to a more restrictive and larger radius by visual inspection of the profile and the model decompositions. Similarly, we cut the profile of several objects before reaching the limiting radius, due to the presence of irregularities or possible contamination sources that we wanted to avoid in the final profile fit.

For each simulation, `Elbow` minimises the residual distances of the input observational profile to a broken profile modelled as

$$\mu(r) = \begin{cases} \mu_{0,\mathrm{i}} + \dfrac{2.5}{\ln(10)} \cdot \dfrac{r}{h_\mathrm{i}} & \text{if } r < R_\mathrm{break}, \\ \mu_{0,\mathrm{o}} + \dfrac{2.5}{\ln(10)} \cdot \dfrac{r}{h_\mathrm{o}} & \text{if } r > R_\mathrm{break}, \end{cases} \tag{9}$$

$$R_\mathrm{break} = h_\mathrm{i} \cdot h_\mathrm{o} \cdot \frac{\ln(10)}{2.5} \cdot \frac{\mu_{0,\mathrm{i}} - \mu_{0,\mathrm{o}}}{h_\mathrm{i} - h_\mathrm{o}} \tag{10}$$

hence we obtain the probability distribution of the characteristic parameters for both inner and outer profiles, as well as the R_break probability distribution. We estimate the maximum likelihood solution for h_i, $\mu_{0,\mathrm{i}}$, h_o and $\mu_{0,\mathrm{o}}$ (or best solutions) as the mode of the corresponding distribution. For each simulation, we calculate a value for R_break following Eq. (10). The best solution of R_break is defined as the value corresponding to the maximum likelihood solution for h_i, $\mu_{0,\mathrm{i}}$, h_o and $\mu_{0,\mathrm{o}}$. Thus, R_break is a dependent parameter of the inner and outer fits to the profile. In contrast to that, the corresponding μ_break values are calculated from the interpolation of the input profile at the break position $R = R_\mathrm{break}$.

`Elbow` estimates the probability density distributions (PDDs, hereafter) as the distribution of each parameter resulting from the simulations (~100 000 in our case). We used these PDDs to estimate the central values of each distribution (maximum probability values, which is the mode of the distribution, as mentioned above) and the uncertainty intervals (for 1, 2 and 3σ). We also used these PDDs to estimate the probability that the inner and outer profiles are significantly different. That is:

$$H_{0,1}: h_\mathrm{i} = h_\mathrm{o}, \tag{11}$$

$$H_{0,2}: \mu_{0,\mathrm{i}} = \mu_{0,\mathrm{o}}. \tag{12}$$

Our null hypothesis is that the two profiles are not different, so that the inner slope and the outer slope would be the same ($H_{0,1}$) or that the central magnitude of the inner profile is compatible with that of the outer profile ($H_{0,2}$). Thus the probability for this test consists of two estimators: 1) the fraction of simulations that gave an $h_\mathrm{o} > h_\mathrm{i}$ in the case of a Type-III profile (and $h_\mathrm{o} < h_\mathrm{i}$ in the case of a Type-II profile) and 2) the fraction of simulations that gave $\mu_{0,\mathrm{o}} > \mu_{0,\mathrm{i}}$ in the case of a Type-III profile (and $\mu_{0,\mathrm{o}} < \mu_{0,\mathrm{i}}$ in the case of a Type-II profile). These two p-values are extremely consistent and in most cases they present equivalent or equal results (see Table B.1). We note that this test does

[2] http://irsa.ipac.caltech.edu/applications/DUST/
[3] R: A language and environment for statistical computing http://www.R-project.org

not only take into account the presence of a noticeable excess of light in the outskirts of the galaxy, but it also would give negative results if this light distribution is not well fitted by a double exponential disc function. This was the case in several objects with irregularities in the outer regions of their profiles.

After that, we ran the simulations and identified those objects with significant breaks in their final profiles. Finally we visually checked the profiles and the fits, and classified all the objects in the three different classes (Type I, II or III). We assume a p-value of 10^{-2} as a the limit value beyond to accept a profile as a Type III, which corresponds to a 99% confidence level that the PDDs of the characteristic parameters of the profile are not compatible with a Type-I profile. The same was applied for the Type-II profiles.

In Fig. 6 we show three examples of the final break analysis performed to the deconvolved profiles. The top panels show the composed RGB images of each object with the limiting radius indicated. The intermediate panels of Fig. 6 represent the corresponding surface brightness profile in the R band corrected for dust extinction, cosmological dimming and K-correction of each object. We plot those radial bins that were included in the final break fit. We systematically avoided the innermost regions due the dominant bulge emission. We plot the best fits to the inner and outer regions, along with the best $R_{\rm break}$ and $\mu_{\rm break}$ respectively, with their 1σ confidence regions, also indicated. The best results obtained for the inner and outer fitted profiles along with their respective confidence intervals are indicated in the intermediate panels.

For the profile of the object in the first column of panels of Fig. 6 (SHARDS20002966) the confidence regions of the inner outer profiles completely overlap (see the left bottom panel). The p-value associated with this profile is $p = 0.224$, so the null hypothesis is not discarded and therefore, we do not find any difference between the inner and outer profiles, meaning that this galaxy has a Type-I profile. On the contrary, SHARDS10000845 (second column of panels) presents a clear Type-II profile. The associated p-value calculated with `Elbow` for this profile is $p = 3.4 \times 10^{-4}$, thus we can discard the null hypothesis and the break is statistically significant. A clear Type-III case is SHARDS10000327 (see the third column of panels in Fig. 6). The associated p-value for this Type-III break is $p = 3.0 \times 10^{-4}$, thus the break is statistically significant. The lower row of panels of Fig. 6 represents the 2D probability distribution (PDD) of the scale-length h and central surface brightness μ_0 for the three cases. The colour scale is linear and represents density of solutions of both inner ($\mu_{0,\rm i}$, $h_{\rm i}$) and outer profiles ($\mu_{0,\rm o}$, $h_{\rm o}$) in an arbitrary scale. These 2D histograms represent where the fitted solutions concentrate for each profile, in order to find the best central surface brightness and scale-length. In the case of SHARDS10000327 and SHARDS10000845 (which present a clear break) the solutions converge on a bimodal distribution with two maxima, marked with black crosses. On the contrary, the PDD of SHARDS20002966 only presents one clear maximum, meaning that it is a Type-I profile.

In Fig. 7 we show the PDDs for each parameter of the surface brightness profile of SHARDS10000327 ($h_{\rm i}$, $h_{\rm o}$ and $R_{\rm break}$ in the upper row, and $\mu_{0,\rm i}$, $\mu_{0,\rm o}$ and $\mu_{\rm break}$ in the lower row). We show the maximum likelihood solution for $h_{\rm i}$, $\mu_{0,\rm i}$, $h_{\rm o}$ and $\mu_{0,\rm o}$. The PDD for $R_{\rm break}$ shows the solution derived from these best-fit parameters following Eq. (10). Finally, we show the corresponding PDD for the $\mu_{\rm break}$ measured over the surface brightness profile with the best fit solution marked also with a vertical dashed-dotted line. As detailed before, SHARDS10000327 shows a Type-III surface brightness profile. This causes that the PDD for $h_{\rm i}$ is centred at a lower value that the PDD for $h_{\rm o}$. An analogous result is found for $\mu_{0,\rm i}$ and $\mu_{0,\rm o}$. As a consequence of this, the histograms for $R_{\rm break}$ and $\mu_{\rm break}$ show single-peaked and Gaussian-like PDDs, meaning that the break is well-defined and statistically significant.

The best fitting results for the 44 S0 and E/S0 galaxies at $z < 0.6$ within our sample, along with the confidence intervals and p-values, are available in Table B.1.

2.7. Efficiency and reliability of the PSF correction

We also tested the reliability and efficiency of the PSF correction process by including synthetic images of galaxies with intrinsic exponential profiles into the GOODS-N image convolved with our PSF. After that, we analysed the type of profile which is recovered following the same procedure that we have used with real ones. To do this, we generated nine synthetic galaxy models with bulge + pure Type-I exponential discs. We chose three different size ranges: small, medium and large, with $R_{\rm eff,bulge} = 0.06, 0.12$ and 0.18 arcsec and $h = 0.24, 0.42$ and 0.6 arcsec respectively. We used three different inclinations ($0^{\rm o}$, $45^{\rm o}$ and $90^{\rm o}$) in order to test the variation of the PSF effects and the dependence of the result of the deconvolution with disc inclination. The models were generated with `GALFIT3.0`.

The synthetic images were generated by convolving the models created with `GALFIT3.0` with our PSF model (see Sect. 2.3). After this, we included the resulting image in a region free of detections in the GOODS-N mosaic. We took into account: 1) the possible presence of background sources not resolved or with low S/N ratio that were not detected in the masking process; and 2) the noise distribution, which had to be similar to the one in the real images. We did not find any differences with the results described next when a pure Gaussian noise distribution was added to the images, which indicates that the sky level and the background sources were not affecting our profiles. After the synthetic galaxies are generated, we used the same procedure as in the case of the real images (see Sects. 2.4–2.6).

In Fig. 8 we show the surface brightness profiles of our synthetic Type-I models convolved (analogous to our original data) and not (i.e., the real profile) by the PSF of our data, and the surface brightness profiles of the deconvolved images, meaning the profiles recovered after using the same extraction and analysis procedures as in our real data. We also plot the radius at which $S/N = 3$. The surface brightness profiles of the PSF-affected models present clear excesses in the outskirts compared to the real (non-affected by the PSF) profiles, which systematically increases the radial region where the object has a $S/N > 3$. The main result is that, after the PSF correction, we successfully remove or reduce most of the scattered light, reconstructing the real shape of the profiles in the centre at the same time (see the differences between the real, original Type-I profiles and those recovered by our procedure in the corresponding subpanels, as a function of radius).

We also used `Elbow` to analyse whether the PSF wings can create apparent Type-III profiles in the synthetic Type-I galaxies that we have simulated. This test was also useful as a benchmark to test `Elbow` on a synthetic model. The results of the analysis are summarised in Table 1. In the table we show the p-values associated with the likelihood of each surface brightness profile to be well-represented by a single exponential profile. We find that:

- The amount of light scattered by the PSF to the outskirts of the synthetic objects is generally small, but it is detectable as

A&A 604, A119 (2017)

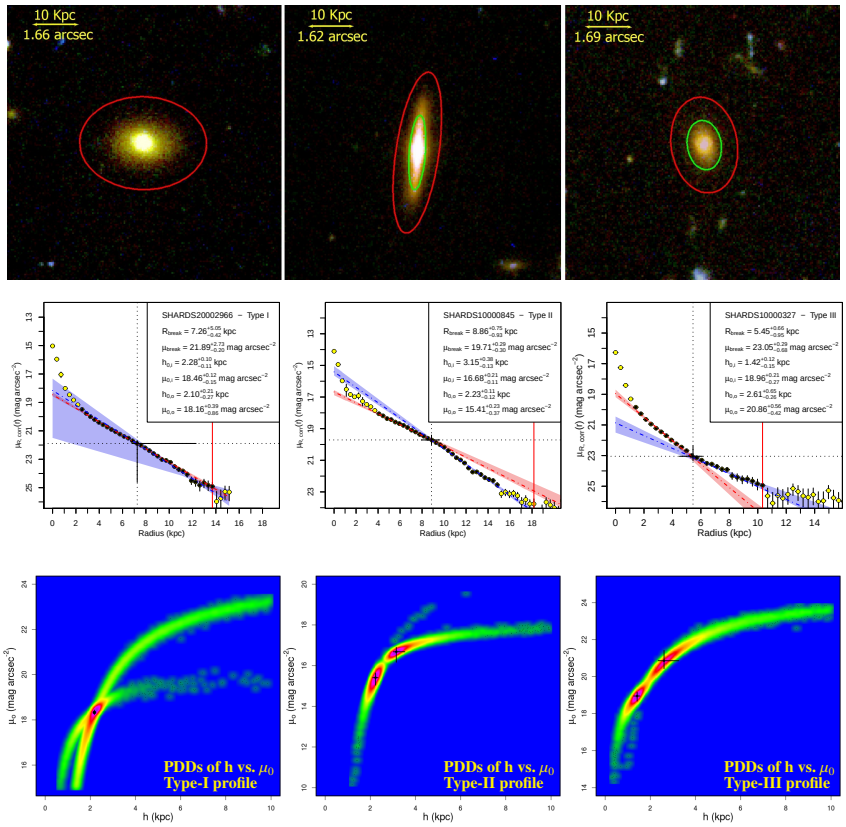

Fig. 6. Examples of the three kinds of disc profiles in our sample of S0 and E/S0 galaxies and their analysis. *Columns, from left to right*: 1) Type I: SHARDS20002966; 2) Type II: SHARDS10000845; 3) Type III: SHARDS10000327. *Upper row*: RGB composed images of the objects using the HST/ACS filters *F435W* (blue), *F606W* (green) and *F775W* (red). The total FoV is 10×10 arcsec^2. The red ellipse marks where the surface brightness profile presents a $S/N = 3$. The green ellipse indicates the location of the break if the profile is a Type II or III. The yellow bar represents 10 kpc in physical size. *Middle row*: surface brightness profiles in the rest-frame *R* band corrected for the dust extinction, cosmological dimming and K-correction of the corresponding objects. Only the black filled points where included in the final break fit. The yellow points were removed from the fit to avoid bulge light contamination or are outside the limiting radius. The red and blue dashed-dotted lines represent the best fits to the inner and outer regions of the disc, and the coloured uncertainty regions around them represent the 1σ confidence interval of each fit, respectively. The red vertical line represents the limiting radius for considering data points in the fit ($S/N = 3$). The dotted lines indicate the most probable break location in the profile (note the high uncertainty in the Type-I profile). *Lower row*: 2D probability density distributions (PDDs) for the scale-length h and central surface brightness μ_0 decompositions. We note that in the case of SHARDS1000327 and SHARDS10000845 the PDDs show two peaks where the inner and outer profiles are located, while in SHARDS20002966 the solutions for the two profiles peak around an unique point. The rainbow-like colour scale represents probability density, with redder colours indicating higher values.

a break by `Elbow` in PSF-uncorrected profiles (especially in the face-on and 45º inclination cases of the small objects).

– The PSF deconvolution procedure efficiently removes the scattered light in the outskirts and recovers the inner profile at the same time.

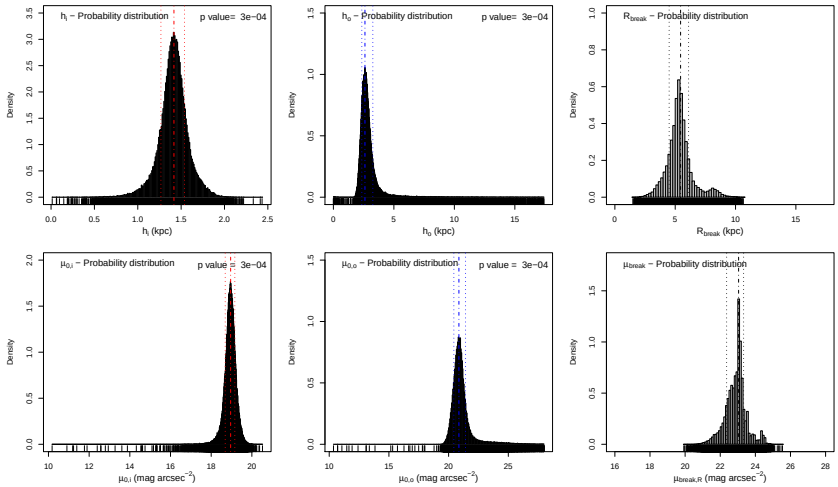

Fig. 7. Probability density distributions of the surface brightness profile fit for the Type-III S0 galaxy SHARDS10000327. *Upper row, from left to right*: scale-length for the inner disc profile h_i (kpc), scale-length for the outer profile h_o (kpc), break radius R_{break} (kpc). *Lower row, from left to right*: central surface brightness profile of the inner profile $\mu_{0,i}$ (mag arcsec^{-2}), central surface brightness profile of the outer profile $\mu_{0,o}$ (mag arcsec^{-2}), surface brightness at the break radius (μ_{break}). The dashed-dotted lines represent the best solutions for each parameter, and the dotted lines mask the limits of the 68% (1σ) confidence region.

Table 1. Likelihood (p-values) for the surface brightness profiles of the synthetic models, so that the PSF uncorrected images and the deconvolved models present a Type-I (pure exponential) profile.

Orientation	PSF	Large	Medium	Small
Face-on	Uncorrected	0.105	0.010	6×10^{-4}
	Deconvolved	0.199	0.499	0.120
45º	Uncorrected	0.119	0.013	2×10^{-4}
	Deconvolved	0.489	0.185	0.079
Edge-on	Uncorrected	0.009	0.131	0.085
	Deconvolved	0.365	0.230	0.496

Notes. The small, medium and large models present $R_{eff,bulge} = 0.18$, 0.12 and 0.06 arcsec and $h = 0.6$, 0.42 and 0.24 arcsec respectively. The models were deconvolved following the procedure described in Sect. 2.3, and analysed with `Elbow`.

Consequently, the deconvolved images are completely free of misclassified Type-III profiles in all ranges of sizes and orientations due to PSF effects. We can therefore conclude that the procedure that we have followed for extracting and correcting the surface brightness profiles for PSF effects is reliable and efficient for recovering the real profiles.

2.8. AGN in the initial sample

We detailed in the previous sections that the deconvolution procedure relies on the fact that the light distribution of the objects is sufficiently well approximated by a certain analytical function (in our case, different combinations of Sérsic profiles). For galaxies hosting a powerful active galactic nucleus (AGN), this may not be the case. The light distribution of the central regions of AGN host galaxies may be much brighter than those with no AGN emission. As a consequence of this, we may be systematically underestimating the PSF contribution in the outskirts.

Alexander et al. (2003) have identified X-ray emitters in the Chandra Deep Field North, which covers the entire GOODS-N field. They detected 503 sources in 7 X-ray bands between 0.5–8 keV. Barger et al. (2003) found optical and infrared counterparts for the objects identified by Alexander et al. (2003). In Bauer et al. (2004), the authors classified the 504 objects in the categories AGN, star-forming galaxies and Galactic stars by using their optical spectral classifications, radio morphologies, variability, X-ray-to-optical flux ratios, X-ray spectra and their intrinsic luminosities. In order to take into account the presence of AGN in our sample, we have cross-correlated our initial red sample with the AGN catalogues in GOODS-N. We used the optical coordinates from Barger et al. (2003) to find the matching sources within 1 arcsec of separation.

We found nine matching sources, four of which are classified as star-forming galaxy candidates (SHARDS10001344, SHARDS20000827, SHARDS20002935 and SHARDS20003134) and five of them classified as AGN

A&A 604, A119 (2017)

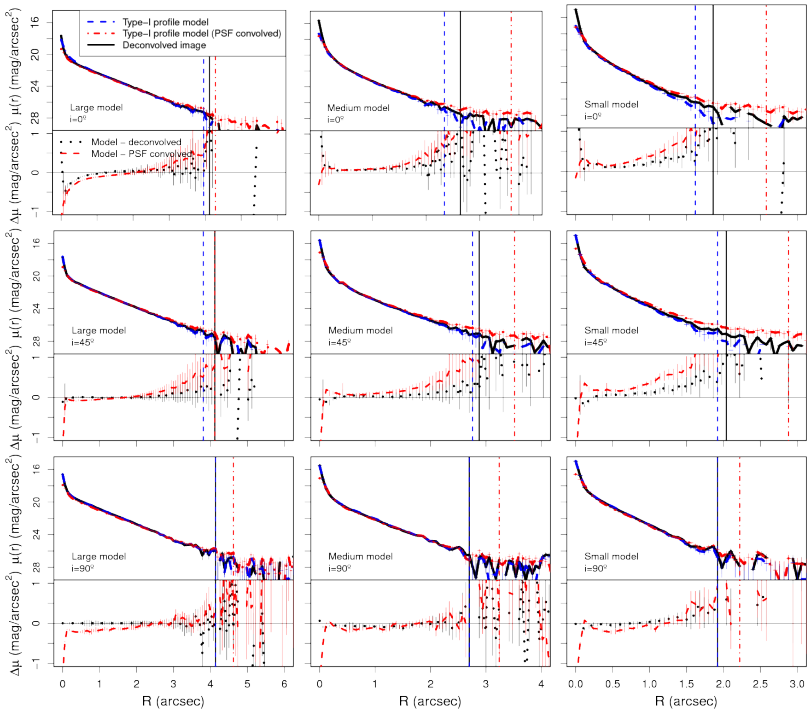

Fig. 8. Surface brightness profiles of the synthetic images of galaxies: *Top panels*: $i = 0°$. *Middle panels*: $i = 45°$. *Bottom panels*: $i = 90°$. *Left column*: large sized model. *Middle column*: medium sized model. *Right column*: small sized model. Blue dashed profile: non-PSF affected surface brightness profile (real profile). Red dashed-dotted profile: PSF-affected surface brightness profile (analogous to our original uncorrected data). Black solid profile: PSF-corrected surface brightness profile. The vertical solid lines represent the limiting radius of each profile (solid black line: PSF-corrected profile, dashed blue line: non-PSF affected model profile, dashed-dotted red line: PSF-convolved model profile). *Lower panels*: black dotted line differences between the non-PSF affected and the corrected surface brightness profile. Dashed line differences between the non-PSF affected and the PSF affected surface brightness profile.

(SHARDS10000827, SHARDS20002147, SHARDS20003119, SHARDS20003377 and SHARDS20004440). All nine sources are S0 or E/S0s in our classification, with the exception of SHARDS20003119, which was classified as a red spiral by us. The maximum distance between the matching sources in the Rainbow catalogue and the optical coordinates was less than 0.3 arcsec and we did not find any other possible counterparts until we increased the matching radius to 5 arcsec, well above the precision of the astrometry.

The emission of a source smaller than the pixel size of the detector would create a 2D light distribution equal to the PSF, by definition. To account for the possible optical emission of the AGN in these objects, we have added a PSF component to their `GALFIT3.0` model. Therefore, we fitted the AGN, the bulge component and the disc as the sum of a PSF, a free Sérsic and an exponential ($n = 1$) Sérsic profile. The model fitting was performed inside out, starting from a PSF + free Sérsic profile for the inner regions and then adding the disc component once a stable solution was reached for the inner regions. In some cases, we needed to fix several parameters alternatively, such as total fluxes or the centres of the components. Finally, we inspected the residuals and the solution, paying attention to the innermost regions. Due to unavoidable degeneracies between the PSF and the bulge total flux as a result of the limited spatial resolution, we have flagged the AGN objects in our sample in Table B.1, although we have kept them in the final sample of S0–E/S0 galaxies.

Furthermore, the classification of 4 S0 galaxies by Bauer et al. (2004) as star-forming galaxies appears to be in

contradiction with the results from the SFR calculated using the data in the Rainbow Database (see Sect. 3.2). We checked ancillary data for each one of these objects for signs of star-formation.

SHARDS20000827 was included in the sample from Treu et al. (2005) (Table 1, ID 1267). These authors do not report any [OII] or [Hδ] emission lines in a $S/N = 32.12$ spectrum and the galaxy was also classified as S0. This object was also studied in Georgakakis et al. (2007) (Table 1, ID 81). They do not find any IR emission excess above the stellar expectation. They pointed out that X-ray emission of this object may be due to hot gas and low mass X-ray binaries.

SHARDS10001344 was also classified as an IR-faint object in Georgakakis et al., (Table 1, ID 354). These authors propose a post-starburst classification (possibly due to a past merger event) as a cause for the observed X-ray emission, although the observed IR luminosity is compatible with those of early-type galaxies.

The observed wavelength of the Hα emission line for SHARDS20002935 is $\lambda_{H\alpha} \sim 9677$ Å ($z = 0.4745$), which is in the observable spectral window of the WFC3 grism in the NIR (G141). The Rainbow Database contains a G141 1D spectrum, which we analysed looking for any signs of emission lines. We found an Hα emission line candidate at $\lambda = 9692$ Å, with a total flux of $f_{H\alpha} = 1.61^{+1.61}_{-0.82} \times 10^{-16}$ erg cm^{-2} s^{-1}. This emission entails a total Hα luminosity in of $L_{H\alpha} = 1.34^{+1.36}_{-0.69} \times 10^{40}$ erg s^{-1}. Assuming the expression given by Kennicutt et al. (1994):

$$SFR_{H\alpha}\left(M_\odot\,\mathrm{yr}^{-1}\right) = 7.9 \times 10^{-42}\, L_{H_\alpha}\left(\mathrm{erg\,s}^{-1}\right), \quad (13)$$

we estimate a $SFR_{H\alpha} = 1.06^{+1.07}_{-0.54}\ M_\odot\ \mathrm{yr}^{-1}$. This value is very similar to the total SFR obtained by the combination of the NIR and 2800 Å emission and thus compatible with a quiescent galaxy ($SFR = 3.05\ M_\odot\ \mathrm{yr}^{-1}$ and $\log_{10} M/M_\odot = 10.92$, see Sect. 3.2).

The Team Keck Treasury Redshift Survey (TKRS, Wirth et al. 2004) has an available optical spectrum between 5000–10 000 Å of SHARDS20003134 (ID 4554). Simple visual inspection of the data was sufficient to discard any signs of emission lines associated with star formation.

Finally, Ptak et al. (2007) uses SED fitting procedures to estimate photometric redshift and separate galaxy types. According to their results the SEDs of SHARDS10001344, SHARDS20000827, SHARDS20002935 and SHARDS20003134 are compatible with those of early-type galaxies.

In conclusion, we have identified the objects and corrected the images and the profiles of the sources with possible AGN activity accounting for the central AGN light emission. In addition to this, the ancillary data studied supports our morphological classification, and confirms that the SFR levels of the objects included in our sample are compatible with those of early-type galaxies. Therefore, these four AGN with S0 morphology were finally kept in the final S0 – E/S0 sample.

3. Results and discussion

3.1. Statistics of the red galaxy sample by morphology

After the revision performed to the visual morphological classification by checking the images and the PSF-corrected surface brightness profiles, we find that, from the original sample of 150 red galaxies at $0.2 < z < 0.6$, 38 were finally classified as S0 (25.3%) and 12 as E/S0 (8.0%) – this is a total of 33.3% S0 and E/S0 objects in the red galaxy sample. Additionally, 40 sources were classified as compact post-starburst objects (26.6%), 32 objects have been classified as diffuse objects (21.3%), nine objects present clear signs of being in interaction with others (6.0%), seven are classified as "green peas" (4.7%), nine objects have been confirmed as E galaxies (6.0%), and we have also identified three spiral galaxies.

The results of the morphological classification of the red galaxy sample selected at $0.2 < z < 0.6$ within the SHARDS catalogue in the GOODS-N field and the following physical parameters are presented in Appendix A: position (α, δ), morphological type, photometric redshift (z_{phot}), spectroscopic redshift when available (z_{spec}), stellar mass, SFR, rest-frame absolute magnitude in the Johnson V (M_V) and K_s bands (M_K), the extinction correction (A_{F775W}) and the median ($R - F775W$) colours used for K-correction. In conclusion, from 150 objects from the red sample we have removed 100 objects and we have obtained a final sample of 38 S0s and 12 E/S0s (50 objects in total) from which to search for Type-III disc profiles.

3.2. Star formation rates and masses as a function of the morphology

The right panel of Fig. 5 represents the stellar masses of the objects of the red sequence sample vs. their redshift. We have used different symbols according to the assigned morphology, to compare the properties of our selected subsample of 50 S0 and E/S0 with those of all galaxies in the initial red sequence sample. The objects classified within the well-resolved high-S/N morphological types (see Sect. 2.2) present stellar masses two orders of magnitude higher than the low-S/N counterparts. The S0 and E/S0 galaxies have stellar masses between 10^9 and $10^{11}\ M_\odot$.

One of the fundamental characteristics of the S0 galaxies is their low SFR in the discs, by definition. We have selected our initial sample by using a colour-colour diagram that isolates the objects in the red sequence, which are good candidates for having old stellar populations and no recent star formation episodes (see Sect. 2.2). In order to confirm their quiescence, we have used the available data in the Rainbow Database to ensure that the SFRs of the selected S0 and E/S0 objects are low, coherently with their morphological type. In Fig. 9 we represent the SFR (top panels) and the specific SFR, defined as $sSFR = SFR/M_\star$ (bottom panels) for the objects of the initial red sequence sample, as a function of z (left column) and the stellar mass ($M_\star$, right column). We show the typical values for the SFR of different morphological types in the local universe (Thronson et al. 1989; Young & Knezek 1989; Young & Scoville 1991; Caldwell et al. 1994; Kennicutt 1998; Sansom et al. 2000; Wei et al. 2010a,b; Amblard et al. 2014). In the bottom panels we plot a conservative upper limit for the sSFR in quiescent galaxies ($sSFR = 0.2\ \mathrm{Gyr}^{-1}$, see Domínguez Sánchez et al. 2016), along with a higher value for this limit of quiescence ($sSFR = 0.32\ \mathrm{Gyr}^{-1}$, see Barro et al. 2013). The procedure to estimate the total SFR from the UV emission at 2800 Å (caused by young stars) and the total IR emission between 8 and 1000 μm (caused by dust re-emission) is fully detailed in Barro et al. (2013, and references therein).

The data available in the Rainbow database do not provide direct SFR values for most of our objects. In fact, 129 out of 150 only have upper limits for the SFR (represented by downpointing arrows, see the top panels in Fig. 9). We note that the observed correlation of the SFR upper limits is a systematic effect due to the detection limits in NIR and UV. Thus, for the objects at increasing z, we obtain higher upper limits. Nevertheless,

A&A 604, A119 (2017)

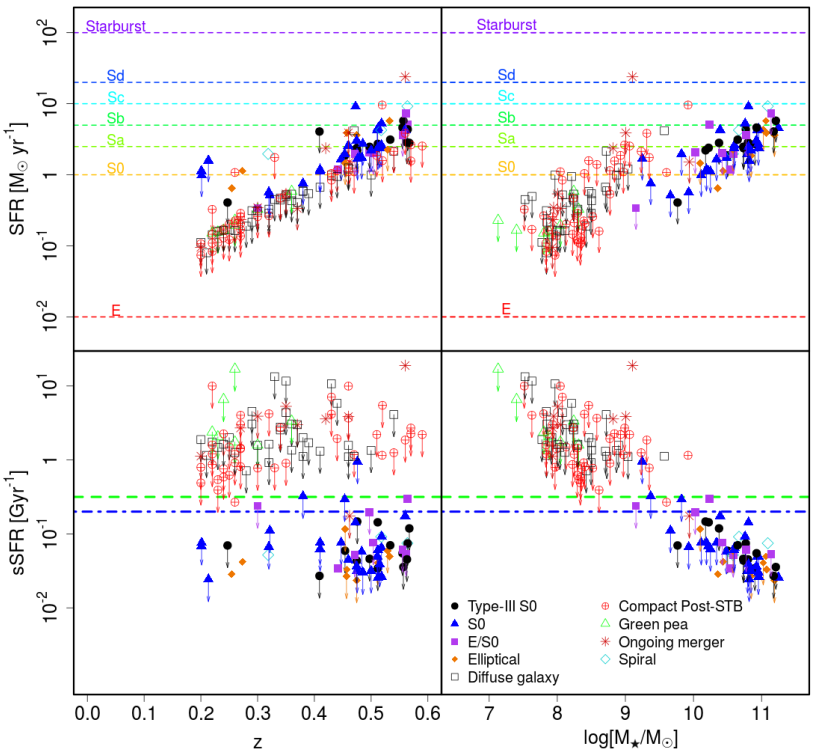

Fig. 9. SFR (*top row*) and sSFR (*bottom row*) for the objects of the initial red sequence sample, as a function of z (*left column*) and the stellar mass (*right column*), according to their morphological types. Arrows indicate upper limits for the SFRs. The horizontal dashed lines in *the top panels* represent the typical values for the SFR for different morphological types in the local universe (see references in the text). Note that these values change with z (see the text). The blue dash-dotted line and the green dashed line in the bottom panels correspond to two typical reference upper limits for the sSFR in early-type galaxies (see the text). Consult the legend in the figure for the morphological type.

this does not affect our aim, because we only needed to test whether the objects present low levels of star formation or not and the detection limits are low enough to do so. In the upper panels of Fig. 9, it is shown that the galaxies classified as S0 and E/S0 present SFR levels close to the typical values of local S0-Sa galaxies, as expected for the quiescent nature of S0s and E/S0s, corroborating the morphological classification that we have performed. Multiple studies indicate that galaxies were forming stars more actively in the past, regardless of their environment (Lilly et al. 1996; Schiminovich et al. 2005). The typical SFR of S0 and E/S0 galaxies increases from the local universe to $z = 0.8$ and it reaches values of 4 $M_\odot\,\mathrm{yr}^{-1}$ at $z = 0.6$ (Menanteau et al. 2001). This is in good agreement with the SFR distribution of our S0 and E/S0 sample ($\langle SFR\rangle = 2.4^{+1.0}_{-1.9}\ M_\odot\,\mathrm{yr}^{-1}$).

We also show that the sSFR of those objects classified as S0 and E/S0 is lower than -or close to- the typical values usually considered as the upper limit to identify quiescent objects in the bottom panels of Fig. 9. The only object that presents an upper limit for the sSFR higher than the reference values is SHARDS20002889 ($SFR < 1.68\ M_\odot\,\mathrm{yr}^{-1}$, $sSFR < 0.95\ \mathrm{Gyr}^{-1}$, $\log_{10} M/M_\odot = 9.25$). Careful visual inspection of the images reveals a close bright galaxy in the *F435W* band, which has a clumpy structure and could be a face-on spiral galaxy. Traces of star formation in the outskirts of our object by this spiral galaxy may be biasing the sSFR derived from Rainbow data towards higher values. We note that the objects classified as diffuse, green peas, and compact post-starburst galaxies show higher sSFR than the S0 and E/S0s, clearly above the limits of quiescence. Those

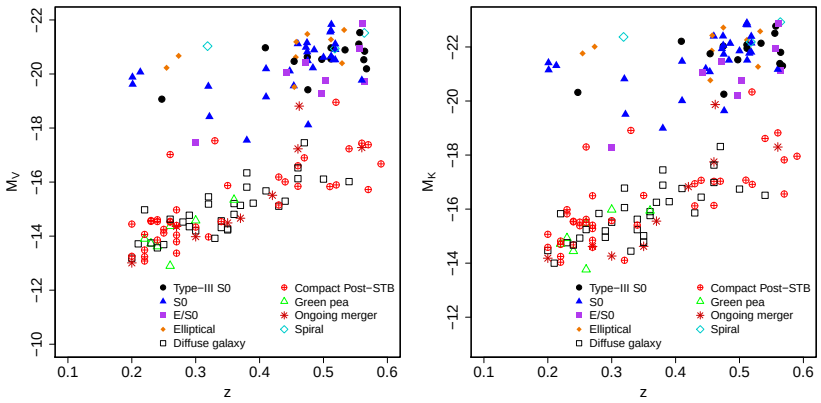

Fig. 10. Synthetic rest-frame absolute magnitude distribution of the objects in the red sample versus z, as a function of their morphological types. *Left panel*: Johnson V band rest-frame absolute magnitude. *Right panel*: K_s band rest-frame absolute magnitude.

objects present similar values for the total SFR as our S0s and E/S0s but much lower stellar masses, thus resulting in higher sSFR values.

In Fig. 10 we show the distribution of rest-frame absolute magnitudes in the Johnson V band and K_s band, as a function of their redshift and the morphological type. We find that the objects classified as S0 or E/S0 present absolute V band magnitudes between $-22 < M_V < -18$. Quiescent galaxies present colours with typical values of $(B-V) \sim 1.0$ (Kinney et al. 1996; Bell & de Jong 2001), so the objects classified as S0s and E/S0s in our sample, would present absolute magnitudes in the Johnson B band of $-17 > M_B > -21$. The available data on local Type-III S0 galaxies present a similar range of absolute magnitudes in the B band (Erwin et al. 2008; Gutiérrez et al. 2011), so the S0 and E/S0 galaxies in our sample at $0.2 < z < 0.6$ are analogous to those in the available local samples, enabling the direct comparison with them.

The right panel of Fig. 10 shows the same diagram as in the left panel, but for the rest-frame K_s absolute magnitude. We find that the S0 and E/S0 galaxies of our sample present values between $-19 > M_K > -23$. By using the stellar masses in the Rainbow database we find a mass-to-light ratio in the K band of $M/L_K = 0.68^{+0.43}_{-0.16}\, M_\odot/L_{K,\odot}$. Assuming $(B-V) \sim 1.0$, Bell et al. (2003) predict a mass-to-light ratio in the K_s band of $M/L_K \sim 0.85\, M_\odot/L_{K,\odot}$ for quiescent galaxies, which is compatible with the results found for the objects in our sample.

We conclude that the SFR and sSFR of the objects that we have identified visually as S0s and E/S0s are characteristic of quiescent objects at the corresponding redshifts of each galaxy, therefore supporting our morphological classification.

3.3. Types of disc profiles in the S0 sample

We created `GALFIT3.0` models for 44 objects from the sample of 50 S0 and E/S0s (~88%). We discarded the six remaining objects because they presented an apparent size too small and/or a `GALFIT3.0` solution too unstable for a bulge+disc model (SHARDS10001928, SHARDS10002901, SHARDS10005029, SHARDS10008552, SHARDS20000858, SHARDS20004273). The presence of significant breaks in the S0 – E/S0 sample was confirmed quantitatively by `Elbow`. Using automatic fitting classification, we classified the galaxies into three types: Type I (23 objects, 52% of the sample), Type II (seven objects, 16% of the sample) and Type III (14 objects, 32% of the sample).

Due to the limiting depth of the observations, we find three different cases where a Type-III profile may be detectable by the automated break analysis routine `Elbow`:

1. The outer profile is clearly resolved, usually associated with bright values of the $\mu_{\rm break}$ and low p-values of `Elbow` (e.g, SHARDS10000327).
2. The outer profile is not clearly resolved, because it presents low values of the h_o/h_i ratio or dimmer values of the $\mu_{\rm break}$, that usually result in smaller detectable radial zones to fit (e.g. SHARDS10003647).
3. The anti-truncation is observed on a bright region, but the outer profile presents irregularities or is not well represented by an exponential disc (e.g, SHARDS10001344).

In order to estimate the effects of the PSF on the profiles, we also analysed the original profiles without the PSF correction. We found that 6 anti-truncations detected in PSF-uncorrected images were removed from the profiles after the PSF correction (SHARDS10001269, SHARDS20002147, SHARDS20003377, SHARDS20003678, SHARDS20004440, and the apparent hybrid Type II+III profile, SHARDS10001847, which resulted to be a simple Type-II profile). Two Type-I profiles were classified as Type-II after the PSF subtraction (SHARDS10004777 and SHARDS20002995). None of the Type-II profiles was classified as Type I or Type III after PSF correction. Due to the shape of the PSF – that disperses light from the brighter and (almost always) inner parts of a source – this was an expected result, given that it is extremely unlikely for any object to present more light in the outskirts after PSF deconvolution.

A&A 604, A119 (2017)

Finally, we report that 14 out of a final sample of 44 S0 and E/S0 galaxies present anti-truncated surface stellar profiles once corrected for PSF effects. As explained above, this final sample of 44 objects only includes those S0 and E/S0 galaxies that were successfully corrected from PSF effects through 2D modelling and were not contaminated by FoV objects. We note that the p-values for the break test in SHARDS20003134 present very different values ($p_h = 2.0\times10^{-2}$ and $p_{\mu_0} = 7.6\times10^{-4}$). The profile clearly shows a Type-II break, although with an irregular inner profile, which could be the cause of the lack of agreement in this case. 13 out of the 14 the Type-III objects have z values equal or higher than 0.4, with the exception of SHARDS20000593, which has a spectroscopic redshift of $z = 0.247$. The lack of objects at the lower redshift range is expected since the 82.6% of the S0 and E/S0 sample have redshifts higher than $z = 0.4$. This means that we find a fraction of ∼30% of Type-III profiles in S0 and E/S0 galaxies at $0.4 < z < 0.6$. This fraction of Type-III profiles from the total S0 and E/S0 sample is slightly lower than the observed ratio of Type-III profiles in local S0 and E/S0 galaxies in E08 and G11 (∼50%), but compatible to the ∼20−30% detected in Laine et al. (2014, 2016).

The final profile classification is available in Table B.1. Comments on individual objects, RGB images and the piecewise fits to the PSF-corrected disc surface brightness profiles of the 44 S0 and E/S0 galaxies in our PSF-corrected sample are available in Appendix C.

Finally, we compare the surface brightness profiles of the identified Type-I galaxies with the surface brightness profiles of the Type-II and Type-III galaxies from our sample. We fit single exponential profiles to the Type-I profiles and estimate their values of scale length h and central surface brightness μ_0. We found a median value for the scale length of the Type-I galaxies of $h = 1.69^{+0.42}_{-0.29}$ kpc, and the central surface brightness of $\mu_0 = 18.65^{+0.39}_{-0.14}$ mag arcsec^{-2}. In contrast, the median values for the scale-lengths of Type-II profiles are $h_i = 3.15^{+0.00}_{-0.27}$ kpc and $h_o = 2.23^{+0.09}_{-0.12}$ kpc, and $\mu_{0,i} = 17.92^{+0.96}_{-0.15}$ mag arcsec^{-2}, $\mu_{0,o} = 16.84^{+0.56}_{-0.48}$ mag arcsec^{-2} for the central surface brightness. In the case of Type-III profiles, these values are $h_i = 1.94^{+0.21}_{-0.34}$ kpc and $h_o = 3.31^{+0.13}_{-0.61}$ kpc, and $\mu_{0,i} = 18.19^{+0.20}_{-0.28}$ mag arcsec^{-2}, $\mu_{0,o} = 20.21^{+0.10}_{-0.43}$ mag arcsec^{-2} for the central surface brightness (see Table 2). As before, the median values were estimated by 50.000 1σ bootstrapping + Monte Carlo simulations. In Fig. 11 we show the distribution of the central surface brightness μ_0 vs. scale-length h for each profile type. We have represented the inner and outer profile parameters by separate in the case of Type-II and Type-III galaxies. We found an overall agreement between the distributions of the inner parts from the Type-III profiles and the same parameters from Type-I profiles, which is not observed in the outer Type-III profiles or in the Type-II profile parameters. We conclude that the profiles of the Type-I S0 and E/S0 galaxies in our sample at $0.2 < z < 0.6$ have values for the characteristic parameters more similar to the inner discs of the Type-III galaxies than those of the outer profiles of Type-III galaxies (see Table 2).

3.4. Comparison of anti-truncated discs of S0 galaxies at $0.2 < z < 0.6$ with local analogs

In Fig. 12 we show the distributions of the characteristic parameters of the Type-III surface brightness profiles of our sample of S0 and E/S0 galaxies at $0.2 < z < 0.6$, compared to those of local Type-III S0 galaxies by E08 and G11. This local sample consists

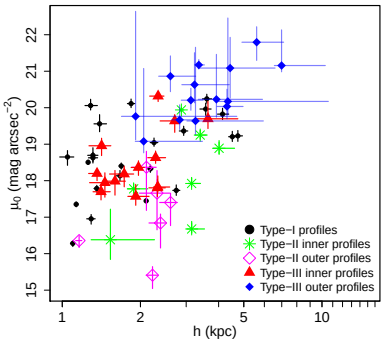

Fig. 11. Central surface brightness μ_0 vs. scale-length h diagram showing the distribution of the Type-I, Type-II and Type-III profile parameters. See the legend for details.

Table 2. Median values of the structural and photometric parameters fitted to Type-III profiles of real S0s.

	Parameter		$z \simeq 0$	$0.2 < z < 0.6$
a)	$\langle R_{break}\rangle$	[kpc]	$7.8^{+1.1}_{-1.1}$	$7.88^{+1.10}_{-0.98}$
b)	$\langle h_i\rangle$	[kpc]	$1.96^{+0.49}_{-0.13}$	$1.94^{+0.21}_{-0.34}$
c)	$\langle h_o\rangle$	[kpc]	$3.58^{+0.21}_{-0.83}$	$3.31^{+0.13}_{-0.61}$
d)	$\langle \mu_{break}\rangle$	[mag arcsec^{-2}]	$24.30^{+0.50}_{-0.10}$	$22.68^{+0.17}_{-0.32}$
e)	$\langle \mu_{0,i}\rangle$	[mag arcsec^{-2}]	$19.59^{+0.52}_{-0.25}$	$18.19^{+0.20}_{-0.28}$
f)	$\langle \mu_{0,o}\rangle$	[mag arcsec^{-2}]	$21.60^{+0.27}_{-0.30}$	$20.21^{+0.10}_{-0.43}$

Notes. *Left column*: values for the samples on the local Universe (E08, G11). *Right column:* Values for the sample at $0.2 < z < 0.6$. *Rows from top to bottom*: a) Break radius R_{break} (kpc); b) inner profile scale length h_i (kpc); c) outer profile scale length h_o (kpc); d) surface brightness at the break radius μ_{break} (mag arcsec^{-2}); e) central surface brightness of the inner profile $\mu_{0,i}$ (mag arcsec^{-2}); f) central surface brightness of the outer profile $\mu_{0,o}$ (mag arcsec $^{-2}$).

20 antitruncated S0 – E/S0 galaxies. Thus the sample size is low but comparable to our own ($N = 14$). The median values of each distribution are shown with solid vertical lines. The top panels represent the distribution of the structural parameters (R_{break}, h_i and h_o), and the lower panels represent the distribution of the photometric parameters (μ_{break}, $\mu_{0,i}$ and $\mu_{0,o}$). The median values of the distributions for each parameter, for both samples, are summarised in Table 2, and were estimated by 50.000 1σ Monte Carlo + bootstrapping simulations.

The distributions of the structural parameters R_{break}, h_i, and h_o in the top panels of Fig. 12 are very similar for the local and our $0.2 < z < 0.6$ sample, showing compatible median values (see also Table 2). We use the Anderson-Darling criterion (Scholz & Stephens 1987) in order to test whether the parameters from both samples arose from a common unspecified distribution function (null hypothesis). The results indicate that there are no noticeable differences between the distributions of the structural parameters (the p-values are $p = 0.463$ for R_{break},

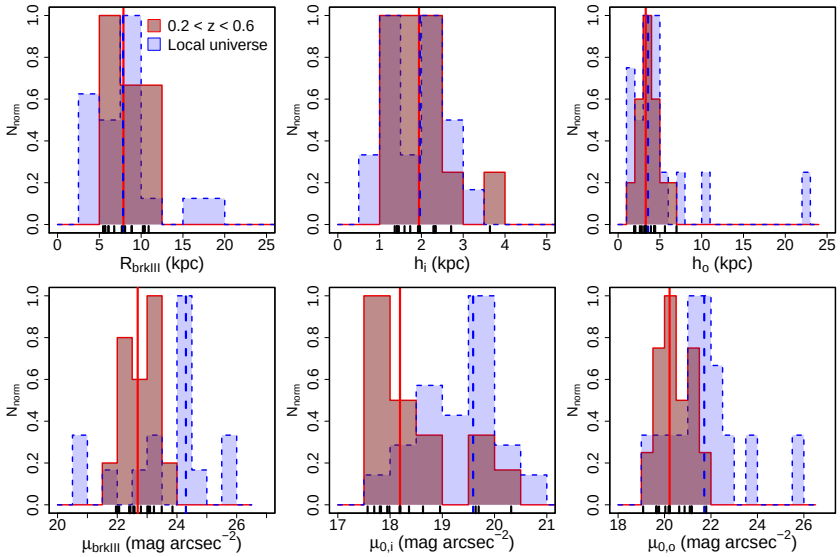

Fig. 12. Normalised distributions of the structural and photometric parameters of the Type-III breaks of the our sample of S0 and E/S0 at $0.2 < z < 0.6$, compared to those from the local universe (E08 and G11). *Upper row, from left to right*: break radius $R_{\rm break}$ (kpc), scale-length of the inner disc profile $h_{\rm i}$ (kpc), scale-length of the outer profile $h_{\rm o}$ (kpc). *Lower row, from left to right*: surface brightness at the break radius $\mu_{\rm break}$ (mag arcsec^{-2}), central surface brightness of the inner disc profile $\mu_{0,\rm i}$ (mag arcsec^{-2}), central surface brightness of the outer profile $\mu_{0,\rm o}$ (mag arcsec^{-2}). The red solid histogram marks our sample of Type-III S0 and E/S0 galaxies at $0.2 < z < 0.6$. The blue dashed histogram represents the distributions found for local universe sample from data by E08 and G11.

$p = 0.243$ for $h_{\rm i}$ and $p = 0.542$ for $h_{\rm o}$). We found that our sample at $0.2 < z < 0.6$ shows lower maximum values of $h_{\rm o}$ (i.e, the largest outer profile scale length in the local sample has a value $h_{\rm o} = 22.26$ kpc, while the maximum of the our higher redshift sample is $h_{\rm o} \sim 7$ kpc). Similarly, the outermost break of the local sample presents a $R_{\rm break} = 18.6$ kpc compared with the maximum value $R_{\rm break} = 10.89^{+3.44}_{-0.44}$ kpc of the sample at $0.2 < z < 0.6$. This could be for two reasons: 1) the local sample contains deeper data than ours at $0.2 < z < 0.6$, and therefore, we could be losing the outermost parts of the corresponding analogs at $z \sim 0.5$; or 2) the profiles of the local sample with such large values of $R_{\rm break}$ and $h_{\rm o}$ could be affected by diffuse PSF tails that were misidentified with real Type-III profiles, because these authors did not correct for PSF effects. Nevertheless, we note that the Anderson-Darling test did not find any noticeable differences between the general distributions of the structural parameters, thus the impact of these effects would require to be tested with larger samples. We also note that the Type-III S0 with the largest $R_{\rm break}$ from the sample at $0.2 < z < 0.6$ is also the only edge-on S0 galaxy with a Type-III profile.

The lower panels of Fig. 12 show the distributions of $\mu_{\rm break}$, $\mu_{0,\rm i}$ and $\mu_{0,\rm o}$. Contrary to the structural parameters, the photometric parameters of the two samples do not give either compatible distributions or median values. We apply again the Anderson-Darling criterion to test whether the parameters from both samples arose from a common parent sample. The p-values are $p = 6.9 \times 10^{-3}$ for $\mu_{\rm break}$, $p = 4.4 \times 10^{-3}$ for $\mu_{0,\rm i}$ and $p = 3.1 \times 10^{-3}$ for $\mu_{0,\rm o}$. The results indicate that there are noticeable differences between the distributions of the photometric parameters of the samples of Type-III S0-E/S0 galaxies at $0.2 < z < 0.6$ when comparing to the local sample. The $\mu_{\rm break}$, $\mu_{0,\rm i}$ and $\mu_{0,\rm o}$ values of the sample at $0.2 < z < 0.6$ are brighter than the local sample by $\sim$1.5 mag arcsec^{-2} ($\Delta\mu_{\rm break} = -1.61^{+0.33}_{-0.53}$ mag arcsec^{-2}, $\Delta\mu_{0,\rm i} = -1.40^{+0.39}_{-0.56}$ mag arcsec^{-2}, $\Delta\mu_{0,\rm o} = -1.49^{+0.46}_{-0.46}$ mag arcsec^{-2}). Deeper surface brightness profiles and a possible PSF contribution could possibly explain this result. But, in any case, we expect a general brightening of the surface brightness profiles of galaxies with increasing z, due to the stellar population evolution, which could also explain this difference (see Bruzual & Charlot 2003; Tapia et al. 2017, and references therein).

3.5. Effects of the PSF on the profiles

In order to test the effects of the scattered light on the surface brightness distribution, we have analysed the profiles of the original images without the PSF correction and compared them with the PSF-corrected profiles. In Fig. 13 we compare the results of

A&A 604, A119 (2017)

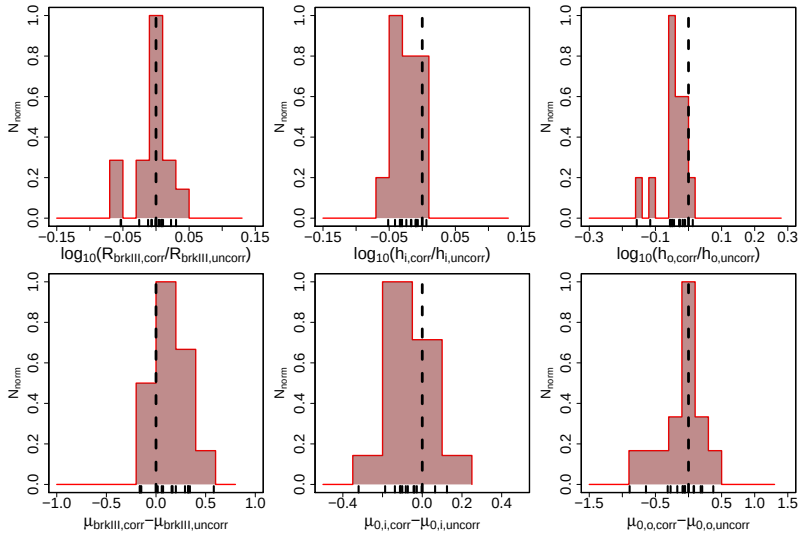

Fig. 13. Comparison between the PSF corrected and non-corrected values of the structural and photometric parameters of the Type-III S0 and E/S0 at $0.2 < z < 0.6$ sample. *Upper row, from left to right:* decimal logarithm of the ratio between the PSF corrected structural parameters and the same parameters measured on the original profile: break radius $R_{\rm break}$ (kpc), scale-length of the inner profile $h_{\rm i}$ (kpc), scale-length of the outer profile $h_{\rm o}$ (kpc). *Lower row, from left to right*: differences between the PSF corrected structural parameters and the same measured on the original profile: surface brightness at the break radius $\mu_{\rm break}$ (mag arcsec^{-2}), central surface brightness of the inner profile $\mu_{0,\rm i}$ (mag arcsec^{-2}), central surface brightness of the outer profile $\mu_{0,\rm o}$ (mag arcsec^{-2}). The black dashed vertical line represents the ratio or difference where the PSF correction would not have any effect.

the structural and photometric parameters of the Type-III profiles in our S0 and E/S0 sample before and after being corrected by PSF contribution. The histograms in the upper row show the decimal logarithm of the ratio of the $R_{\rm break}$, $h_{\rm i}$ and $h_{\rm o}$ values measured on the corrected profiles over those parameters measured on the uncorrected profiles. We plot the value that would result if the PSF did not have any effect on the observed structure. We found that $h_{\rm o}$ can have significantly higher values in the uncorrected profiles than in the PSF-corrected ones ($\Delta h_{\rm o} = h_{\rm o}, corr - h_{\rm o}, uncorr = -0.37^{+0.33}_{-0.37}$ kpc). Thus, the dispersed light can increase systematically the outer profile scale length. This also happens with the distribution of $h_{\rm i}$ ($\Delta h_{\rm i} = -0.105^{+0.082}_{-0.083}$ kpc) although the results are less significant. In contrast, the distribution of ratios of $R_{\rm break}$ does not show any clear bias ($\Delta R_{\rm break} = -0.087^{+0.54}_{-0.55}$ kpc).

In the lower panels of Fig. 13, we represent the differences between the values of $\mu_{\rm break}$, $\mu_{0,\rm i}$ and $\mu_{0,\rm o}$ measured on the profiles corrected for PSF effects and the original (uncorrected) ones. Again, the dashed lines represent the position in a case in which the dispersed light did not have any effect on our profiles. We do not find any systematic effect in their distributions ($\Delta\mu_{\rm break} = 0.16^{+0.23}_{-0.23}$ mag arcsec^{-2}, $\Delta\mu_{0,\rm i} = -0.07^{+0.11}_{-0.11}$ mag arcsec^{-2}, $\Delta\mu_{0,\rm o} = -0.10^{+0.25}_{-0.26}$ mag arcsec^{-2}). In conclusion, the inner and outer disc scale-lengths are the parameters that are most affected by the PSF scattered light.

4. Conclusions

We present the first sample of S0 and E/S0 galaxies with anti-truncated discs obtained beyond the local Universe (at $0.2 < z < 0.6$), on the basis of PSF-corrected surface brightness profiles. We have described in detail the selection procedure and analysis performed to characterise them on a sample of 150 red galaxies at $0.2 < z < 0.6$ on the GOODS-N field, by using both HST/ACS and SHARDS data from the Rainbow database. We have selected a sample of quiescent disc galaxies with visual S0 and E/S0 morphologies, and studied their SFRs, sSFRs, stellar masses and their surface brightness profiles. Additionally, we have corrected for PSF-scattered light in their *F775W* images, to obtain surface brightness profiles unbiased by the light dispersion produced by the PSF of our data.

To estimate the break parameters accurately and perform a quantitative morphological classification of the surface brightness profiles, we have developed `Elbow`, a programme to detect, classify and fit breaks in surface brightness profiles, which we have made publicly available. We identified S0 and E/S0 objects at $0.2 < z < 0.6$, with exponential (Type I), truncated (Type II) and anti-truncated (Type III) profiles and fitted their different disc components with exponential functions. We compared the structural and photometric parameters from the sample of Type-III galaxies in the range $0.2 < z < 0.6$ with the local samples

from previous studies (E08 and G11). Our main results are the following:

1. We report the first sample of Type-III profiles in S0 and E/S0 galaxies at $0.2 < z < 0.6$, corrected for PSF effects. We found that 14 out of 44 S0-E/S0 galaxies at $0.2 < z < 0.6$ after PSF corrections have antitruncated profiles (∼30%). This fraction is similar to the those reported in the local Universe by Laine et al. (2014, 2016).
2. As a result of correcting the profiles for scattered light by the PSF, we found that ∼25−30% of the apparent Type-III S0 discs detected in uncorrected profiles are false positives and can be explained by a combination of pure exponential profiles and scattered light from the inner regions. In two cases, we found significant down-bending breaks (Type-II profile) after the PSF deconvolution.
3. The structural parameters ($R_{\rm break}$, $h_{\rm i}$ and $h_{\rm o}$) of the Type-III profiles at $0.2 < z < 0.6$ present similar distributions to their local counterparts. In contrast, the photometric parameters ($\mu_{\rm break}$, $\mu_{0,\rm i}$ and $\mu_{0,\rm o}$) have values ∼1.5 mag arcsec^{-2} brighter than the local sample from E08 and G11.
4. The PSF-dispersed light tends to increase the scale-lengths of the inner and outer disc profiles ($h_{\rm i}$, $h_{\rm o}$) in our sample of Type-III S0 and E/S0 galaxies, but it does not significantly affect either the central surface brightness values of the inner and outer discs ($\mu_{0,\rm i}$, $\mu_{0,\rm o}$) or the break location, $R_{\rm break}$.
5. The profiles of Type-I of our S0 and E/S0 sample have characteristic values compatible with the inner profiles ($\mu_{0,\rm i}$ and $h_{\rm i}$) of Type-III S0 and E/S0 galaxies, but they are not consistent with the equivalent parameters ($\mu_{0,\rm o}$ and $h_{\rm o}$) of the outer profiles.

The wings of the PSF tend to create an apparent excess of emission in the outskirts of the galaxies. This tends to increase both $h_{\rm i}$ and $h_{\rm o}$ in Type-III profiles. For any study that does not take into account the effects of the PSF on the profiles, this will yield a systematic bias in the results. This applies not only to Type-III profiles, but also to Type-II profiles, as commented above. We also show that the PSF-corrected images recover some Type-II breaks, which were not detectable in the original images. Therefore; in PSF-uncorrected data, an unknown fraction of the real Type-II profiles may be softened to the point of being misclassified as Type-I by the observers.

In this work we have presented `Elbow`[4], a statistically robust and automated method to fit, classify the surface brightness profiles and calculate the likelihood associated with a certain break to exist (Types II and III) or not (Type I). This tool is free and we make it available for the scientific community. The non-linear nature of the surface brightness magnitudes demands a careful treatment of the uncertainties and error propagation, especially when measuring quantities in the low S/N regime. In order to properly account for the uncertainties associated with the surface brightness profiles, `Elbow` calculates the errors using non-parametric statistics, such as the bootstrap resampling and the Monte Carlo method. Future studies may analyse what percentage of the reported surface brightness profiles have been previously misidentified due to the lack of an appropriate statistical method. Moreover, the results from the present and other recent studies (such as Sandin 2014; Trujillo & Fliri 2016, and references in Sect. 1) demonstrate that the PSF corrections are clearly necessary in this sort of studies, especially when working with low surface-brightness Type-III profiles.

[4] `Elbow` is publicly available at GitHub (https://github.com/Borlaff/Elbow)

According to the results presented here, the structure of the Type-III profiles of S0 galaxies at $0.2 < z < 0.6$ appears to be similar to the local ones. Nevertheless, the $\mu_{0,\rm i}$, $\mu_{0,\rm o}$ and $\mu_{\rm break}$ have brighter values than the local sample by −1.5 mag arcsec^{-2}. This could be due to one or several of the following reasons:

1. The difference may be due to the evolution of the stellar populations. This is expected to produce general brightening of the surface brightness profiles of galaxies with increasing z, sufficient to explain the difference between the samples (see Bruzual & Charlot 2003; Tapia et al. 2017, and references therein).
2. Due to the observational depth limit in the surface brightness, we could be biased to the innermost (and thus brighter) Type-III breaks. Nevertheless, we think this effect is negligible in our sample, because the $R_{\rm break}$, $h_{\rm i}$ and $h_{\rm o}$ distributions of our $0.2 < z < 0.6$ S0 and E/S0 galaxies are highly compatible with those of the local sample, and only differ for the high values.
3. The local sample studies traditionally have not corrected for PSF effects. The wings created by the PSF tend to create Type-III profiles with dimmer values of $\mu_{0,\rm o}$ and larger values of $h_{\rm o}$. Still, although the scattered light may introduce systematic biases in the results – especially in the $h_{\rm o}$ values - it is highly unlikely that most Type-III profiles in the current local samples have been dramatically modified (or produced) by the PSF effects alone.

Recent papers have thrown doubt on the real nature of some Type-III profiles, attributing them to central light scattered radially outwards by the PSF of the telescope optics. Here we have carried out a successful detailed procedure to correct this effect from a large sample of objects and get unbiased samples of discs with real breaks in their surface brightness profiles. As a result, we present the first sample of proven Type-III profiles of S0 and E/S0 objects beyond the local Universe, in the range $0.2 < z < 0.6$, and that will be analysed in detail in a forthcoming paper (Borlaff et al., in prep.).

Acknowledgements. We thank the referee very much for comments that have significantly improved the quality of this work. Supported by the Ministerio de Economía y Competitividad del Gobierno de España (MINECO) under project AYA2012-31277 and project P3/86 of the Instituto de Astrofisica de Canarias. PGP-G acknowledges support from MINECO grants AYA2015-70815-ERC and AYA2015-63650-P. This work has made use of the Rainbow Cosmological Surveys Database, which is operated by the Universidad Complutense de Madrid (UCM) partnered with the University of California Observatories at Santa Cruz (UCO/Lick,UCSC). We are deeply grateful to the SHARDS team, since this work would not have been possible without their efforts. Based on observations made with the Gran Telescopio Canarias (GTC) installed at the Spanish Observatorio del Roque de los Muchachos of the Instituto de Astrofísica de Canarias, in the island of La Palma. We thank all the GTC Staff for their support and enthusiasm with the SHARDS project. This work is based on observations taken by the 3D-HST Treasury Program (GO 12177 and 12328) with the NASA/ESA HST, which is operated by the Association of Universities for Research in Astronomy, Inc., under NASA contract NAS5-26555. We acknowledge Dr. Pilar Esquej for describing us the usual procedure followed to identify AGN hosts in our S0 sample. The authors thank David Velilla for his kind technical support, and Ignacio Trujillo for his advice with the PSF correction procedures.

References

Alexander, D. M., Bauer, F. E., Brandt, W. N., et al. 2003, AJ, 126, 539
Amblard, A., Riguccini, L., Temi, P., et al. 2014, ApJ, 783, 135
Barger, A. J., Cowie, L. L., Capak, P., et al. 2003, ApJ, 584, L61
Barro, G., Pérez-González, P. G., Gallego, J., et al. 2011a, ApJS, 193, 13
Barro, G., Pérez-González, P. G., Gallego, J., et al. 2011b, ApJS, 193, 30
Barro, G., Faber, S. M., Pérez-González, P. G., et al. 2013, ApJ, 765, 104
Bauer, F. E., Alexander, D. M., Brandt, W. N., et al. 2004, AJ, 128, 2048

Bell, E. F., & de Jong, R. S. 2001, ApJ, 550, 212
Bell, E. F., McIntosh, D. H., Katz, N., & Weinberg, M. D. 2003, ApJS, 149, 289
Bertin, E., & Arnouts, S. 1996, A&AS, 117, 393
Borlaff, A., Eliche-Moral, M. C., Rodríguez-Pérez, C., et al. 2014, A&A, 570, A103
Brammer, G. B., Whitaker, K. E., van Dokkum, P. G., et al. 2011, ApJ, 739, 24
Bruzual, G., & Charlot, S. 2003, MNRAS, 344, 1000
Caldwell, N., Kennicutt, R., & Schommer, R. 1994, AJ, 108, 1186
Cardamone, C., Schawinski, K., Sarzi, M., et al. 2009, MNRAS, 399, 1191
Cardiel, N., Gorgas, J., Cenarro, J., & Gonzalez, J. J. 1998, A&AS, 127, 597
Ciambur, B. C. 2015, ApJ, 810, 120
Comerón, S., Elmegreen, B. G., Salo, H., et al. 2012, ApJ, 759, 98
de Jong, R. S. 2008, MNRAS, 388, 1521
de Vaucouleurs, G. 1959, Handbuch der Physik, 53, 275
Dickinson, M., Giavalisco, M., & GOODS Team 2003, in The Mass of Galaxies at Low and High Redshift, eds. R. Bender, & A. Renzini, 324
Domínguez Sánchez, H., Pérez-González, P. G., Esquej, P., et al. 2016, MNRAS, 457, 3743
Eliche-Moral, M. C., Borlaff, A., Beckman, J. E., & Gutiérrez, L. 2015, A&A, 580, A33
Elmegreen, B. G., & Hunter, D. A. 2006, ApJ, 636, 712
Erwin, P., Beckman, J. E., & Pohlen, M. 2005, ApJ, 626, L81
Erwin, P., Pohlen, M., & Beckman, J. E. 2008, AJ, 135, 20 (E08)
Erwin, P., Gutiérrez, L., & Beckman, J. E. 2012, ApJ, 744, L11
Fitzpatrick, E. L. 1999, PASP, 111, 63
Freeman, K. C. 1970, ApJ, 160, 811
Georgakakis, A., Rowan-Robinson, M., Babbedge, T. S. R., & Georgantopoulos, I. 2007, MNRAS, 377, 203
Giavalisco, M., Ferguson, H. C., Koekemoer, A. M., et al. 2004, ApJ, 600, L93
Gutiérrez, L., Erwin, P., Aladro, R., & Beckman, J. E. 2011, AJ, 142, 145 (G11)
Herpich, J., Stinson, G. S., Dutton, A. A., et al. 2015, MNRAS, 448, L99
Humason, M. L., Mayall, N. U., & Sandage, A. R. 1956, AJ, 61, 97
Ilyina, M. A., & Sil'chenko, O. K. 2012, Astron. Astrophys. Trans., 27, 313
Indebetouw, R., Mathis, J. S., Babler, B. L., et al. 2005, ApJ, 619, 931
Karabal, E., Duc, P.-A., Kuntschner, H., et al. 2017, A&A, 601, A86
Kazantzidis, S., Zentner, A. R., Kravtsov, A. V., Bullock, J. S., & Debattista, V. P. 2009, ApJ, 700, 1896
Kennicutt, Jr., R. C. 1998, ARA&A, 36, 189
Kennicutt, Jr., R. C., Tamblyn, P., & Congdon, C. E. 1994, ApJ, 435, 22
Kinney, A. L., Calzetti, D., Bohlin, R. C., et al. 1996, ApJ, 467, 38
Kodama, T., Tanaka, I., Kajisawa, M., et al. 2007, MNRAS, 377, 1717
Koekemoer, A. M., Fruchter, A. S., Hook, R. N., & Hack, W. 2003, in HST Calibration Workshop: Hubble after the Installation of the ACS and the NICMOS Cooling System, eds. S. Arribas, A. Koekemoer, & B. Whitmore, 337
Kormendy, J., & Bender, R. 2012, ApJS, 198, 2
Krist, J. E., Hook, R. N., & Stoehr, F. 2011, SPIE Conf. Ser., 8127, 81270J
Kron, R. G. 1980, ApJS, 43, 305
Laine, J., Laurikainen, E., Salo, H., et al. 2014, MNRAS, 441, 1992
Laine, J., Laurikainen, E., & Salo, H. 2016, A&A, 596, A25
Lilly, S. J., Le Fevre, O., Hammer, F., & Crampton, D. 1996, ApJ, 460, L1
Maltby, D. T., Gray, M. E., Aragón-Salamanca, A., et al. 2012, MNRAS, 419, 669
Maltby, D. T., Aragón-Salamanca, A., Gray, M. E., et al. 2015, MNRAS, 447, 1506
Marino, R. A., Gil de Paz, A., Sánchez, S. F., et al. 2016, A&A, 585, A47
Menanteau, F., Jimenez, R., & Matteucci, F. 2001, ApJ, 562, L23
Oke, J. B., & Sandage, A. 1968, ApJ, 154, 21
Pavlovsky, C. M., Mutchler, M. J., & Hack, W. J. 1999, AAS Meeting Abstracts #194, BAAS, 31, 834
Peñarrubia, J., McConnachie, A., & Babul, A. 2006, ApJ, 650, L33
Peng, C. Y., Ho, L. C., Impey, C. D., & Rix, H.-W. 2002, AJ, 124, 266
Pérez-González, P. G., Rieke, G. H., Egami, E., et al. 2005, ApJ, 630, 82
Pérez-González, P. G., Rieke, G. H., Villar, V., et al. 2008, ApJ, 675, 234
Pérez-González, P. G., Cava, A., Barro, G., et al. 2013, ApJ, 762, 46
Pohlen, M., & Trujillo, I. 2006, A&A, 454, 759
Pranger, F., Trujillo, I., Kelvin, L. S., & Cebrián, M. 2017, MNRAS, 467, 2127
Prato, M., Cavicchioli, R., Zanni, L., Boccacci, P., & Bertero, M. 2012, A&A, 539, A133
Ptak, A., Mobasher, B., Hornschemeier, A., Bauer, F., & Norman, C. 2007, ApJ, 667, 826
R Core Team 2016, R: A Language and Environment for Statistical Computing, R Foundation for Statistical Computing, Vienna, Austria, http://www.R-project.org
Roediger, J. C., Courteau, S., Sánchez-Blázquez, P., & McDonald, M. 2012, ApJ, 758, 41
Sandage, A. 1961, The Hubble atlas of galaxies (Washington: Carnegie Institution)
Sandin, C. 2014, A&A, 567, A97
Sandin, C. 2015, A&A, 577, A106
Sansom, A. E., Hibbard, J. E., & Schweizer, F. 2000, AJ, 120, 1946
Schiminovich, D., Ilbert, O., Arnouts, S., et al. 2005, ApJ, 619, L47
Schlegel, D. J., Finkbeiner, D. P., & Davis, M. 1998, ApJ, 500, 525
Scholz, F. W., & Stephens, M. A. 1987, J. Am. Stat. Assoc., 82, 918
Sérsic, J. L. 1963, Boletin de la Asociacion Argentina de Astronomia La Plata Argentina, 6, 41
Sil'chenko, O. K. 2009, in IAU Symp. 254, eds. J. Andersen, J. Bland-Hawthorn, & B. Nordström, 173
Skelton, R. E., Whitaker, K. E., Momcheva, I. G., et al. 2014, ApJS, 214, 24
Spergel, D. N., Bean, R., Doré, O., et al. 2007, ApJS, 170, 377
Tapia, T., Eliche-Moral, M. C., Aceves, H., et al. 2017, A&A, 604, A105
Thronson, Jr., H. A., Tacconi, L., Kenney, J., et al. 1989, ApJ, 344, 747
Treu, T., Ellis, R. S., Liao, T. X., et al. 2005, ApJ, 633, 174
Trujillo, I., & Bakos, J. 2013, MNRAS, 431, 1121
Trujillo, I., & Fliri, J. 2016, ApJ, 823, 123
van Dokkum, P. G., Franx, M., Fabricant, D., Illingworth, G. D., & Kelson, D. D. 2000, ApJ, 541, 95
Wei, L. H., Kannappan, S. J., Vogel, S. N., & Baker, A. J. 2010a, ApJ, 708, 841
Wei, L. H., Vogel, S. N., Kannappan, S. J., et al. 2010b, ApJ, 725, L62
Weijmans, A.-M., de Zeeuw, P. T., Emsellem, E., et al. 2014, MNRAS, 444, 3340
Whitaker, K. E., Labbé, I., van Dokkum, P. G., et al. 2011, ApJ, 735, 86
Whitaker, K. E., van Dokkum, P. G., Brammer, G., & Franx, M. 2012, ApJ, 754, L29
Williams, R. J., Quadri, R. F., Franx, M., van Dokkum, P., & Labbé, I. 2009, ApJ, 691, 1879
Willmer, C. N. A., Faber, S. M., Koo, D. C., et al. 2006, ApJ, 647, 853
Wirth, G. D., Willmer, C. N. A., Amico, P., et al. 2004, AJ, 127, 3121
Young, J. S., & Knezek, P. M. 1989, ApJ, 347, L55
Young, J. S., & Scoville, N. Z. 1991, ARA&A, 29, 581
Younger, J. D., & Bryan, G. L. 2007, ApJ, 666, 647

Important note: Pages from 23 to 71 of the paper presented in this Chapter contain Appendices that have been moved to Chapters A, B, and C in this thesis in the benefit of clarity.

4

Evolution of the anti-truncated stellar profiles of S0 galaxies since $z = 0.6$ in the SHARDS survey II. Structural and photometric evolution

Ex luna, scientia

— Apollo 13 mission badge

In this Chapter we continue the analysis of the Type-III S0-E/S0 galaxies making use of the sample presented in Borlaff et al. (2017, see chapter 3) on the GOODS-N field. The main objective is to compare the properties of the Type-III profiles at $0.2 < z < 0.6$ with those of the local Universe (Erwin et al. 2008; Gutierrez et al. 2011). We study if the correlations found in the structural and photometric diagrams reported on Borlaff et al. (2014) using local galaxies and simulations were present ~ 6 Gyr ago. In addition, we analyse the distribution of the structural ($R_{\rm break}$, $h_{\rm i}$ and $h_{\rm o}$) and photometric ($\mu_{\rm break}$, $\mu_{0,\rm i}$ and $\mu_{0,\rm o}$) parameters as a function of the stellar mass in order to detect possible variations with z. In addition, we study the rest-frame $(B - R)$ colour profiles of the sample of Type-III S0 galaxies. In order to do that, we analysed the bands adjacent to the F775W filter (in which the Type-III surface brightness profiles were detected, see Borlaff et al. 2017), this is the F606W and F850LP bands, correcting them for PSF effects, galactic dust extinction, cosmological dimming and K-correction, as done with the F775W. Finally, we compare if the results are compatible with the predictions of a grid of Single Stellar Population models (SSPs).

We found several interesting results. The structural scaling relations found on Borlaff et al. (2014) in local S0 Type-III galaxies and simulations of S0 galaxies formed through major mergers are also found in Type-III S0-E/S0 galaxies at $0.4 < z < 0.6$. In contrast, the parameters related to the surface brightness ($\mu_{\rm break}$, $\mu_{0,\rm i}$ and $\mu_{0,\rm o}$) do not present compatible distributions when compared to the local sample. Moreover, we found a statistically significant dependence of the surface brightness at the break radius ($\mu_{\rm break}$) with z. The expected $\mu_{\rm break}$ at a constant break radius is $\Delta\mu_{\rm break} \sim 1.5$ mag arcsec^{-2} brighter at $z \sim 0.6$ than in the galaxies from the local Universe. This result is significant even if we correct for inclination or when we remove the objects with large stellar masses from the sample ($\log_{10}(M/M_{\odot}) > 10^{11}$).

In addition, we found no differences between the median colour profiles of the inner and outer parts with respect to the break radius $R_{\rm break}$. In addition, we did not find any significant difference between $R_{\rm break}$ or the scale-lengths of the inner and outer profiles ($h_{\rm i}$ and $h_{\rm o}$) when comparing the objects at $0.4 < z < 0.6$ with those of the local sample, contrasting with the 1.3 ± 0.1 increase of the break radius with cosmic time for Type-II profiles since $z \sim 1$ found by Azzollini et al. (2008b). Finally, we analysed if the apparent dimming of $\Delta\mu_{\rm break} \sim 1.5$ mag arcsec^{-2} in the R band since $z \sim 0.6$ is compatible with the expected evolution of an SSP model. We found that an instantaneous stellar formation burst should not be older than ~ 8 Gyr to decrease its brightness by ~ 1.5 mag arcsec^{-2} from $z = 0.6$ to $z = 0$. This means that, if the dominant population of the Type-III S0 galaxies was formed in a very short period of time, this must have occurred no earlier than $z \sim 1.2$. Otherwise, the SFH of these galaxies must have been be more extended in time than an instantaneous burst.

These results set strong constraints on the models of formation of Type-III S0 galaxies, which have to explain: 1) the presence of antitruncated S0 galaxies at $z \sim 0.6$ at a similar relative fraction to that in the local Universe, 2) the stability of their structure ($R_{\rm break}$, $h_{\rm i}$ and $h_{\rm o}$), and 3) their dimming of $\Delta\mu_{\rm break} \sim 1.5$ mag arcsec^{-2} in the R band since $z \sim 0.6$ when compared to the objects of the same type in the local Universe.

The work presented in this chapter was published in *Astronomy & Astrophysics*, the 5th of July of 2018, in the Volume 615, with article number A26 under the title **"Evolution of the anti-truncated stellar profiles of S0 galaxies since $z = 0.6$ in the SHARDS survey II. Structural and photometric evolution"**.

A&A 615, A26 (2018)
https://doi.org/10.1051/0004-6361/201732090

Astronomy & Astrophysics

Evolution of the anti-truncated stellar profiles of S0 galaxies since z = 0.6 in the SHARDS survey

II. Structural and photometric evolution

Alejandro Borlaff[1,2,3], M. Carmen Eliche-Moral[1,2], John E. Beckman[1,3,4], Alexandre Vazdekis[1,3], Alejandro Lumbreras-Calle[1,3], Bogdan C. Ciambur[5], Pablo G. Pérez-González[2], Nicolás Cardiel[2], Guillermo Barro[6], and Antonio Cava[7]

[1] Instituto de Astrofísica de Canarias, C/ Vía Láctea, 38200 La Laguna, Tenerife, Spain
e-mail: asborlaff@iac.es
[2] Departamento de Astrofísica y CC. de la Atmósfera, Universidad Complutense de Madrid, 28040 Madrid, Spain
[3] Facultad de Física, Universidad de La Laguna, Avda. Astrofísico Fco. Sánchez s/n, 38200 La Laguna, Tenerife, Spain
[4] Consejo Superior de Investigaciones Científicas, Madrid, Spain
[5] Observatoire de Paris, LERMA, PSL Research University, 61 Avenue de l'Observatoire, 75014 Paris, France
[6] University of California, 501 Campbell Hall, Berkeley, Santa Cruz, CA 94720, USA
[7] Observatoire de Genève, Université de Genève, 51 Ch. des Maillettes, 1290 Versoix, Switzerland

Received 11 October 2017 / Accepted 1 March 2018

ABSTRACT

Context. Anti-truncated lenticular galaxies (Type-III S0s) present tight scaling relations between their surface brightness photometric and structural parameters. Although several evolutionary models have been proposed for the formation of these structures, the observations of Type-III S0 galaxies are usually limited to the local Universe.
Aims. We aim to compare the properties of Type-III discs in a sample of S0 galaxies at $0.2 < z < 0.6$ with those of the local Universe. In this paper, we study the evolution of the photometric and structural scaling relations measured in the rest-frame R-band with z and the possible differences between the rest-frame $(B-R)$ colours of the inner and outer disc profiles.
Methods. We make use of a sample of 14 Type-III E/S0–S0 galaxies at $0.2 < z < 0.6$ from the GOODS-N field identified and characterised in a previous paper. We study whether or not the correlations found in local Type-III S0 galaxies were present ∼6 Gyr ago. We analyse the distribution of the surface brightness characteristic parameters ($R_{\rm break}$, $\mu_{\rm break}$, $h_{\rm i}$, $h_{\rm o}$, $\mu_{0,\rm i}$ and $\mu_{0,\rm o}$) as a function of the stellar mass and look to see if there is a significant change with z. We also derive their rest-frame $(B-R)$ colour profiles. Finally, we compare these results with the predictions from a grid of SSP models.
Results. We find that the inner and outer scale-lengths of Type-III S0 galaxies at $0.4 < z < 0.6$ follow compatible trends and scaling relations with those observed in local S0 galaxies as a function of the break radius, $R_{\rm break}$. We do not detect any significant differences between the location of $R_{\rm break}$ between $z \sim 0.6$ and $z \sim 0$ for a fixed stellar mass of the object, whereas the surface brightness at the break radius $\mu_{\rm break}$ is ∼1.5 mag arcsec^{-2} dimmer in the local Universe than at $z \sim 0.6$ for a fixed stellar mass. We find no significant differences in the $(B-R)$ colour between the inner and outer profiles of the Type-III S0 galaxies at $0.2 < z < 0.6$.
Conclusions. In contrast to Type-II (down-bending) profiles, the anti-truncated surface brightness profiles of S0 galaxies present compatible $R_{\rm break}$ values and scaling relations during the last 6 Gyr. This result and the similarity of the colours of the inner and outer discs point to a highly scalable and stable formation process, probably more related to gravitational and dynamical processes than to the evolution of stellar populations.

Key words. galaxies: fundamental parameters – galaxies: elliptical and lenticular, cD – galaxies: structure – galaxies: evolution – galaxies: formation – galaxies: general

1. Introduction

The mechanisms of formation of lenticular (or S0) galaxies are not yet well understood. Although S0 galaxies usually have a prominent disc component, they do not show any signs of star formation or spiral arms on it. They present an intermediate apparent morphology between spiral galaxies (which also show discs but with noticeable arms and star-formation regions) and elliptical galaxies (without any clear signs of a disc or spiral arms and with no star formation). Many authors have claimed that this intermediate position in the well known Tuning Fork diagram (Hubble 1926) was supposed to imply an evolutionary path. Nevertheless, Hubble (1927) warned that the "late/early-type" nomenclature referred to apparent complexity and did not imply any direction of evolution in the morphological classification system (see Baldry 2008, for a detailed discussion about this).

Despite this, there are signs of evolution between the different morphological types. Recent studies such as D'Onofrio et al. (2015) suggest that spiral galaxies have been transforming into S0 galaxies for the last ∼7–8 Gyr (since $z \sim 1$). This is supported by a number of observational facts, such as that the fraction of spiral galaxies at redshift $z \sim 0.5$ was two to three times higher than in the local Universe, while there is an apparent decrease in the fraction of S0 galaxies (Dressler et al. 1997; Abadi et al. 1999). Gunn & Gott (1972) pointed out that this process may have been taking place during the fall of the spirals

A&A 615, A26 (2018)

in the early Universe into the gravitational well of galaxy clusters through ram-pressure stripping. Another process associated to the clusters that could potentially transform spiral galaxies into S0s is galaxy harassment (Moore et al. 1996, 1999; Bialas et al. 2015). In this scenario, high-velocity fly-bys would quench the star formation from spirals, strip stars into the intracluster medium and ultimately transform them into S0s. Galaxy encounters (i.e. mergers) were already suggested by Spitzer & Baade (1951), who considered that galaxy mergers might be responsible for the gas depletion of spiral galaxies, creating a parallel sequence of S0 galaxies.

Although these environmental mechanisms can successfully transform spiral galaxies into S0s, almost ∼50% of S0 galaxies reside in groups and the field, not in clusters. (see Huchra & Geller 1982; Berlind et al. 2006; Crook et al. 2007; Wilman et al. 2009). This implies that the mechanisms leading to the formation of S0s may depend on the environment density and the stellar mass (Barway et al. 2009). Many authors claim that in low-density environments, the most important processes for the formation of S0s are galaxy interactions and the loss of gas from the disc through secular processes. Therefore, secular evolution has been proposed as an important driver of galaxy formation, especially in low-mass S0 galaxies, while the formation of higher mass S0s may have been dominated by mergers (Barway et al. 2007, 2009). This is consistent with the prevalence of pseudobulges in low-luminosity S0s against classical bulges in high-luminosity S0s (Kormendy & Kennicutt 2004; Vaghmare et al. 2013). Given that observational and theoretical studies suggest that massive E-S0 galaxies have undergone at least one major merger during the last ∼9 Gyr regardless of the environment (Eliche-Moral et al. 2010; Prieto et al. 2013), galaxy interactions may have had an important role in low-density environments. It has been suggested that it is in galaxy groups, and not clusters, where the merger rate is higher (Jian et al. 2012). Contrary to popular belief, major mergers can produce well-defined disc remnants (Naab & Burkert 2003; Bournaud et al. 2005; Athanassoula et al. 2016; Rodionov et al. 2017). In fact, many authors find observational evidence of a major-merger origin of many S0s at $z < 1$ (see Peirani et al. 2009; Yang et al. 2009; Hammer et al. 2009a,b, 2012; Tapia et al. 2014; Querejeta et al. 2015a,b). In summary, the existence of multiple evolutionary pathways for the formation of S0 galaxies (Laurikainen et al. 2010; Roche et al. 2010; Wei et al. 2010; Cortesi et al. 2013; Barway et al. 2013), has triggered a heated debate about their origin and evolution.

One of the most common methods to study the origin and evolution of galaxies is the analysis of their surface brightness profiles. The discs of spiral and S0 galaxies show surface brightness profiles that are to first order approximation well-fitted by an exponential function out to a certain radius (Patterson 1940; de 1958; Freeman 1970). This is due to the stellar density decline as a function of galactocentric radius (Sérsic 1963). Nevertheless, many spiral and lenticular galaxies do not follow a purely exponential profile along their whole observable radius (van der Kruit 1979; Pohlen et al. 2000; Pohlen 2002; Kregel et al. 2002; Sil'chenko 2009; Kormendy & Bender 2012; Ilyina & Sil'chenko 2012), although some others do until extremely faint magnitudes (NGC 300, Bland-Hawthorn et al. 2005). Erwin et al. (2005) pointed out that a significant fraction of S0 galaxies present light excesses in the outskirts of the discs, which also show an exponential decline but with a shallower slope than their inner discs (see also Pohlen & Trujillo 2006). Therefore, Pohlen & Trujillo (2006) and Erwin et al. (2008, E08 hereafter) designed a stellar disc classification of galaxies in three main types, according to the profile structure. Type-I discs are well modelled with a single exponential profile. Type-II galaxies present a down-bending profile, that is, the profile of the disc steepens sharply beyond a certain radius with respect to the extrapolated trend of the inner regions (truncation). Type-III discs become shallower outside the break radius than the extrapolation of the exponential trend of the inner parts (anti-truncation, see Pohlen & Trujillo 2006). E08 and Gutiérrez et al. (2011, G11 hereafter) showed that the fraction of anti-truncated discs was higher for S0 galaxies than for any other morphological type, increasing from approximately 10 to 20% in Sc–Sd galaxies and up to ∼20–50% in S0–Sa galaxies (see also Ilyina & Sil'chenko 2012; Maltby et al. 2015). In the present study we focus on S0s with Type-III profiles.

Many mechanisms have been proposed to explain the origin of Type-III profiles, which are sometimes connected to the process responsible for the formation of the S0 galaxy itself. Radially varying profiles of star formation have been proposed as a cause for both Type-II and Type-III profiles (Elmegreen & Hunter 2006). In addition to this, some authors (e.g. Comerón et al. 2012) pointed out that these transitions might be caused by combinations of thin+thick discs with different radial scalelengths. Radial mass redistribution has also been proposed as a cause for the different types of profiles (Herpich et al. 2015, 2017; Ruiz-Lara et al. 2017). In a recent paper, Elmegreen & Struck (2016) found that in galaxy disc simulations, exponential profiles appear from random scattering when there is a slight inward bias in the scatter. They also found that radial variation or thresholds of this bias are able to produce double exponential profiles. Holes and clumps of interstellar gas have been proven to be valid gravitational scattering centres in simulations of dwarf galaxy discs and they were able to generate exponential discs from an initially flat profile in ∼1 Gyr (Struck & Elmegreen 2017). However, most of the proposed mechanisms for the formation of Type-III galaxies are based on some kind of gravitational interaction, such as high-eccentricity fly-bys (Laurikainen & Salo 2001; Peñarrubia et al. 2006), minor mergers (Younger et al. 2007), major mergers (Borlaff et al. 2014), bombardment of the disc by cold dark-matter halos (Kazantzidis et al. 2009) or galaxy harassment (Roediger et al. 2012). Laurikainen & Salo (2001) reported that N-body simulations of M51-like pairs present shallow outer profiles. The authors found out that this was a consequence of the stripping of gas and stars from the galaxies inner discs.

A high fraction of the anti-truncated profiles in spiral galaxies are due entirely to disc structure, although ∼15% might be due to outer stellar haloes (Maltby et al. 2012). In lenticular galaxies, the fraction of anti-truncated profiles caused by the presence of a spherical component (bulge contribution, haloes) may be as high as ∼50% (Maltby et al. 2015), although it is important to note that this is only an upper limit to the real fraction due to the bulge profile used on their analysis. In some cases, transitions between the inner and outer profiles are associated with structural components of the galaxy such as rings or lenses (Laine et al. 2014).

Borlaff et al. (2014, B14 hereafter) tested whether major mergers can produce anti-truncated stellar profiles in S0 galaxies using hydrodynamical N-body simulations. They found that Type-III profiles of S0 remnants can be produced after a major merger event, and that these profiles obey similar scaling relations to those found in real Type-III S0 galaxies. In a later paper, Eliche-Moral et al. (2015) reported that these relations are similar to those found in Type-III spiral galaxies and are independent of the presence of bars, which suggests that fundamental processes must be responsible for the formation of these structures in disc galaxies along the whole Hubble sequence. To

our knowledge, no other study to the date has addressed the possible formation of these tight scaling relations in Type-III profiles through mechanisms other than major mergers.

Previous studies revealed that the break radius of truncated (Type-II) spiral galaxies evolves with time, increasing by a factor of $\sim 1.3 \pm 0.1$ between $z = 1$ and $z = 0$ (Azzollini et al. 2008). However, no study has analysed the properties of anti-truncated S0 and E/S0 galaxies beyond $z \sim 0.2$ to learn about their possible evolution, because cosmological dimming efficiently moves these structures towards even fainter (and prohibitive) surface brightness levels. In order to shed light on the evolution of these structures, we have analysed a sample of Type-III S0 galaxies at $0.2 < z < 0.6$, identified in Borlaff et al. (2017, Paper I hereafter) and compared them to their local analogues from the $z \sim 0$ samples by E08 and G11. We study whether the scaling relations found by B14 in a sample of both local and simulated Type-III S0 galaxies are consistent with those found in Type-III S0 galaxies at $0.2 < z < 0.6$.

The outline of this paper is as follows. The methodology is described in detail in Sect. 2. The results are presented in Sect. 3. We discuss the results in Sect. 4. The final conclusions can be found in Sect. 5. In Appendix A we show the K-corrections applied to the F606W and F850LP band images. We compare the results of the surface brightness profile parameters ($R_{\rm break}$ and $\mu_{\rm break}$) for the F775W and F850LP bands in Appendix B. We summarise all the results of the linear fits applied to the structural, photometric, stellar mass planes and the K-corrections in Appendix C. Finally, we show the surface brightness and colour profiles of our sample of Type-III S0 galaxies at $0.2 < z < 0.6$ in Appendix D. We assume a concordance cosmology ($\Omega_{\rm M} = 0.3, \Omega_{\Lambda} = 0.7, H_0 = 70$ km s^{-1} Mpc^{-1}, see Spergel et al. 2007). All magnitudes are in the AB system (Oke 1971) unless otherwise noted.

2. Methods and data

In this section we describe the available data and the process to obtain surface brightness profiles from the HST/ACS data of the GOODS-N field. We summarise the results from Paper I and describe some novel work performed for the present paper. In Sect. 2.1 we describe the initial sample and the ancillary data from the SHARDS database (SFRs, stellar masses, rest-frame magnitudes) that have been used in Paper I and the present one. We describe the HST imaging data, the PSF and photometric corrections of the images and the attainment of surface brightness profiles of the Type-III S0 galaxies in our sample in Sect. 2.2. In this section we also detail the methods used to analyse, classify and characterise the corrected surface brightness profiles in Paper I. Finally, we extend the analysis in this paper to two additional HST/ACS filters (F606W and F850LP) in Sect. 2.3.

For a full description of the morphological classification, the PSF and photometric corrections of the surface brightness profiles and their analysis for the full sample of S0 galaxies at $0.2 < z < 0.6$, we refer the reader to Paper I.

2.1. SHARDS database

The sample of Type-III S0 – E/S0 galaxies was selected from an initial sample of quiescent galaxies on the GOODS-N field. We restricted the study to this region in order to take advantage of the Survey for High-z Absorption Red and Dead Sources data in this field (SHARDS, Pérez-González et al. 2013). This project is an ESO/GTC Large Program carried out with the OSIRIS instrument on the 10.4 m Gran Telescopio Canarias (GTC). The SHARDS survey obtained data between 5000 Å and 9500 Å for galaxies in the GOODS-N field down to $m < 26.5$ AB magnitudes, in 25 medium band filters (FWHM ~170 Å). SHARDS data are available through the Rainbow Database (Barro et al. 2011a,b). For the GOODS-N field (Barro et al., in prep.) the authors used all the available photometry to build spectral energy distributions (SEDs) from UV (GALEX) to nIR (Herschel). They derived photometric redshifts and estimates of parameters such as the stellar mass, the UV- and IR-based SFRs, the stellar population age and rest-frame magnitudes in different filters from spectral template fitting of the SEDs (Pérez-González et al. 2005, 2008, 2013). The accuracy of the photometric redshifts from SHARDS for the original sample is $\Delta z/(1+z) = 0.0024$. Nevertheless, we used the spectroscopic redshifts when available. We note that all the objects in the final sample of Type-III S0 galaxies at $0.2 < z < 0.6$ presented available spectroscopic redshifts.

We selected all sources from the GOODS-N field in the SHARDS catalogue (excluding those classified as stars or artefacts) which present redshifts in the range $0.2 < z < 0.6$. We used the boundaries on the $(U - V)$ versus $(V - J)$ colour–colour diagram presented in Whitaker et al. (2011, 2012) to select only those objects in the red sequence. The main objective of this was to isolate a sample of potentially quiescent galaxies, which must contain the analogues of local (quiescent) S0s. We excluded those objects with $z < 0.2$ in the catalogue because of the high uncertainties detected in the estimates of the photometric redshifts at these distances (Barro et al. 2011b). After this process, we obtained a sample of 150 red-sequence objects in the range $0.2 < z < 0.6$.

2.2. Surface brightness profiles: data, reduction and corrections

We identified every object in the red-sequence sample in the ACS F435W, F606W, F775W and F850LP mosaics from 3D-HST (HST Cycle 11, programme IDs 9425 and 9583, Giavalisco et al. 2004) available at the 3D-HST project webpage[1] (Skelton et al. 2014). We performed a visual morphological classification based on the ACS images to identify E/S0 and S0 galaxies, supported by the PSF-uncorrected surface brightness profiles in some cases to avoid misclassification of ellipticals as face-on S0s. We classified the objects in seven different morphological types: (1) ellipticals, (2) S0-E/S0 galaxies, (3) spirals, (4) ongoing mergers, (5) compact post-starbursts, (6) green peas and (7) diffuse galaxies. We also analysed the presence of active galactic nucleus (AGN) activity in the selected E/S0-S0 sample to discard AGN hosts, which would have made the PSF corrections uncertain. We checked that the specific star formation rates (sSFR) of the selected E/S0-S0 objects were coherent with being quiescent, accordingly to local S0s. These tests were done as a function of the total stellar mass derived by the SHARDS project.

During this phase, we performed the masking of the background and foreground objects on the F775W images, in order to avoid contamination of the profiles. We refer the reader to Sect. 2.2 on Paper I for details of the morphological classification. After this, we found that 50 objects present

[1] 3D-HST – A Spectroscopic Galaxy Evolution Survey with the *Hubble* Space Telescope: http://3dhst.research.yale.edu/Home.html

A&A 615, A26 (2018)

S0-E/S0 morphologies, all presenting low SFRs, according to local S0s.

Since the main objective of this work was to identify anti-truncated stellar profiles, which appear as light excesses over the inner exponential profile at large radii, it is mandatory to correct the images and the profiles for PSF effects. We did this following a similar methodology to that of Trujillo & Fliri (2016). First, we created a PSF model using two sources: (1) the star-stacked PSF provided by the 3D-HST project for the GOODS-N mosaics of each band (Skelton et al. 2014), and (2) a model of the PSF using the Tiny Tim software (Krist et al. 2011). We combined these to simulate the effect of the dithering pattern and rotation of the camera in the final mosaic (Trujillo & Fliri 2016), because the star-stacked model size is not enough for our purposes (∼4 arcsec in diameter) while, given the apparent size of our object we need at least a ∼25 arcsec diameter PSF to perform any kind of PSF subtraction without the risk of underestimating their effect in the outskirts of the galaxies (Sandin 2014, 2015). After this, we used this PSF model to generate Sérsic bulge + exponential disc models for 44 objects with S0–E/S0 morphologies on the F775W band using `GALFIT3.0` (Peng et al. 2002). We discarded 6 objects from the total 50 S0–E/S0 sample in this step due to their small size and possible contamination from nearby objects in the field of view. The residuals of this PSF-convolved model with respect to the original image were added to the image of the two-dimensional (2D) model before convolution with the PSF.

The final result is a deconvolved image of the selected object (Trujillo & Bakos 2013; Trujillo & Fliri 2016). For further details on the deconvolution procedure, we refer the reader to Sect. 2.3 of Paper I. Subsequently we calculated the surface brightness profiles using the PSF-corrected images. After this, we corrected the profiles for dust extinction, cosmological dimming and K-correction for each S0 and E/S0 object, obtaining the corrected surface brightness profiles in the rest-frame R band, which is the one used in the local samples by E08 and G11 that we use for comparison (see Sect. 2.5, Table A.1 and Fig. 5 in Paper I).

Finally, we performed the identification, characterisation and analysis of the structure of the components in the surface brightness profiles by using a semi-automated method called `Elbow`[2]: a statistically robust method to fit and classify the surface brightness profiles, and calculate the likelihood that a certain break exists (Types II and III) or not (Type I). A detailed explanation of `Elbow` can be found in Sect. 2.6 of Paper I. Finally, we found that 14 S0–E/S0 galaxies present Type-III profiles after PSF corrections (13 at $0.4 < z < 0.6$ and 1 at $z = 0.247$). To our knowledge, this is the first robust sample of anti-truncated S0–E/S0s obtained at $0.2 < z < 0.6$.

2.3. Data for colour profiles

One of the main objectives of the present paper is to look for signs of differences between the stellar populations of the inner and outer profile of our selected Type-III S0s. To do this, we repeat the masking, 2D modelling, photometric corrections (PSF, Galactic extinction, K-correction), surface brightness profile analysis and classification with `Elbow` for the images of the 14 Type-III S0-E/S0 galaxies in the F606W and F850LP bands, following the same procedure previously described (see below). In addition, we have also used the surface brightness profiles in these bands to create colour profiles. We selected the F606W and F850LP bands in order to trace regions of the SED that are as separated as possible in wavelength, but with enough depth in the GOODS-N field to have sufficient emission in the outskirts of the objects. After several tests, the F435W band was discarded because in the vast majority of cases the surface brightness profile reached the limiting magnitude before $R_{\rm break}$. The median limiting magnitudes in our profiles for the selected bands are very similar: $\mu_{\rm F606W,lim} = 27.051^{+0.099}_{-0.058}$ mag arcsec^{-2}, $\mu_{\rm F775W,lim} = 27.092^{+0.024}_{-0.032}$ mag arcsec^{-2} and $\mu_{\rm F850LP,lim} = 26.75^{+0.18}_{-0.17}$ mag arcsec^{-2}. The F606W and F850LP filter images trace $R_{\rm break}$ in all cases, although F606W reaches the limiting magnitude at lower galactocentric radial distances than the F775W and F850LP bands, and thus it dominates the uncertainties in the colour profiles.

We corrected the images in the F606W and F850LP bands for PSF effects using the same procedure as for the F775W images (see Sect. 2.2). We checked that the `GALFIT3.0` models for the F606W and F850LP bands were similar to those calculated for the F775W images. After the PSF correction process, we generate surface brightness profiles from the final images for the 14 Type-III S0 galaxies selected in Paper I at $0.2 < z < 0.6$. We derived the surface brightness profiles by using elliptical concentric apertures with fixed position angle and axis ratio, equal to the mean values obtained with SExtractor (Bertin & Arnouts 1996) in the galaxy disc on the original image, with the limiting threshold set to 1σ. As explained in Paper I, the surface brightness profiles of the edge-on objects were analysed separately, using `ISOFIT` (Ciambur 2015). This program also uses concentric apertures to calculate the surface brightness profile but replaces the angular parameter that defines quasi-elliptical isophotes in polar coordinates with the eccentric anomaly, providing a more accurate modelling of galaxies with high inclinations. We refer the reader to this paper for details on the method and the benefits for the modelling of edge-on galaxies. In this case, the position angle and ellipticity are allowed to vary with radius. We apply this method to the unique edge-on galaxy in our Type-III S0 sample, SHARDS20000827.

Finally, the surface brightness profiles are corrected for Milky Way dust extinction, cosmological dimming and K-correction (see Appendix A). We must remark that although in the present work we have included two additional filters to the analysis, the results from the F606W and F850LP bands are only used for obtaining the colour profiles, while the rest of the analysis is performed with the parameters estimated from the surface brightness profiles in the F775W band in Paper I, K-corrected to rest-frame R band.

3. Results

In this section we analyse the distributions of the characteristic parameters from the surface brightness profiles of Type-III S0–E/S0 galaxies. In Sect. 3.1 we compare the properties of our sample of 14 Type-III S0-E/S0 galaxies at $0.2 < z < 0.6$ with those of a sample of 20 Type-III S0 galaxies in the local Universe from E08 and G11 (local sample, hereafter) and the simulations of Type-III S0 galaxies from major mergers from B14. In Sect. 3.2 we compare the distributions of stellar mass and rest-frame absolute magnitude in the B and K bands from the local and $0.2 < z < 0.6$ samples. We investigate if there is any significant change in the distributions of the structural parameters obtained from the surface brightness profiles with z at a fixed stellar mass, in particular for $R_{\rm break}$ (Sect. 3.3) and $h_{\rm i}$, $h_{\rm o}$ and the ratio $h_{\rm o}/h_{\rm i}$ (Sect. 3.4). We extend the analysis to

[2] `Elbow` is publicly available at GitHub (https://github.com/Borlaff/Elbow)

the photometric parameters $\mu_{0,i}$, $\mu_{0,o}$ and μ_{break} in Sect. 3.5. We study in detail the dependence with z of the μ_{break} vs. R_{break} relation in Sect. 3.6. In addition, we analyse the colour profiles and the median profiles of the $0.4 < z < 0.6$ sample in Sect. 3.7. Finally, we compare the observed distribution of the μ_{break} vs. R_{break} at $z \sim 0$ and $z \sim 0.5$ with the predicted evolution from a grid of single stellar population models (SSP hereafter) just to check whether the measured evolution between these two redshifts could be explained by simple passive evolution or not (see Sect. 3.8). With the exception of the colour profile analysis, where we use the F606W and F850LP bands, we again emphasise that we use the structural and photometric parameters of the antitruncations measured in the F775W band in our sample at $0.2 < z < 0.6$, after being transformed to rest-frame R band, in order to compare with the R-band observations of the local sample (see Sect. 2.2).

3.1. Scaling relations

The left panels of Fig. 1 present the distribution of the inner and outer scale-lengths (h_i and h_o) of the Type-III S0 galaxies in the samples at $0.2 < z < 0.6$ and at the local Universe (E08; G11) as a function of the break radius R_{break}. In addition, we define the characteristic scale R_{23}, which corresponds to the radius at which the surface brightness profile reaches 23 mag arcsec^{-2}. For each diagram, we present another version with the scale-lengths and R_{break} normalised by R_{23} in the right panels of the figure. In order to define an intermediate-redshift sample, we only include in the linear fits of the intermediate redshift sample the objects at $0.4 < z < 0.6$, excluding one and only Type-III S0 galaxy at $0.2 < z < 0.4$ that we found (SHARDS20000593, $z = 0.247$). Therefore, the sample at $0.4 < z < 0.6$ includes 13 S0 – E/S0s with Type-III surface brightness profiles.

As reported in Paper I, h_i, h_o and R_{break} present compatible distributions in the local and $0.4 < z < 0.6$ samples ($h_i \sim$ 1–5 kpc, $h_o \sim$ 1.5–20 kpc and $R_{break} \sim$ 2–20 kpc, see Sect. 3.4 on Paper I for a deeper discussion). The main result in the present work is that Type-III S0 galaxies at $0.4 < z < 0.6$ also present similar correlations and compatible trends to their local analogues in the structural diagrams $\log_{10}(h_i) \propto \log_{10}(R_{break})$, $\log_{10}(h_i/R_{23}) \propto \log_{10}(R_{break}/R_{23})$ and $\log_{10}(h_o) \propto \log_{10}(R_{break})$, first reported in B14. We next quantify these observed correlations and trends between the parameters in each case.

We take into account the uncertainties of the parameters by performing 100 000 Bootstrapping & Monte Carlo simulations of the Spearman correlation test. In order to perform a symmetrical treatment of the variables, we choose the OLS bisector linear regression method (Isobe et al. 1990). Additionally, for each parameter we use the empirical probability density distribution (PDD) that resulted from the analysis performed with `Elbow` of the surface brightness profile of each galaxy as input error (see Section 2.6 in Paper I). By doing this, we take into account any internal correlations between the variables and their uncertainties and thus we generate much more accurate Monte-Carlo simulations than from simply simulating random Gaussian noise around the central point.

We found that the structural diagrams present statistically significant ($p < 0.05$) positive correlations for both local Universe and $0.4 < z < 0.6$ samples (see panels in Fig. 1) with the exception of $\log_{10}(h_o/R_{23}) \propto \log_{10}(R_{break}/R_{23})$ for the local sample, which does not present a significant correlation in the case of the sample at $z = 0$, although it presents a low p-value. In contrast to this, the sample at $0.4 < z < 0.6$ presents a significant correlation. We performed linear fits to the distributions in those planes, which are represented with dashed black (local sample) and solid red lines ($0.4 < z < 0.6$ sample) in the diagrams. The results of the correlation tests and the linear fits are summarised in Table C.1 in Appendix C.

On top of the parameters of the local Universe and $0.2 < z < 0.6$ Type-III S0 galaxies in Fig. 1, we plot the results of the major merger simulations from B14 in purple squares, and the corresponding fitted linear trend with a purple dashed-dotted line. We found that in the diagrams $\log_{10}(h_i) \propto \log_{10}(R_{break})$, $\log_{10}(h_i/R_{23}) \propto \log_{10}(R_{break}/R_{23})$ and $\log_{10}(h_o) \propto \log_{10}(R_{break})$, the parameters of $0.4 < z < 0.6$ and local Type-III S0 galaxies present compatible trends that overlap with the extrapolation towards lower values of those corresponding to the simulated mergers sample. We must remark that the simulations present higher masses ($\sim$1–3 $\times 10^{11}$ $M_\odot$) than the real Type-III S0 galaxies samples. As a consequence, the models present an offset in the non-normalised diagrams. Despite this, the models and the observed Type-III S0 galaxies overlap in the normalised diagrams. We refer the reader to B14 for a detailed discussion on this subject. We conclude that the parameters of $0.4 < z < 0.6$, local and simulated Type-III S0 galaxies present positive correlations and compatible trends in the structural diagrams reported in B14.

In Fig. 2 we present the distribution of the central surface brightness of the inner and outer profiles ($\mu_{0,i}$ and $\mu_{0,o}$) as a function of the break radius R_{break} and the normalised break radius (R_{break}/R_{23}). We report several interesting results. First, in contrast with the structural parameters, the values of $\mu_{0,i}$ and $\mu_{0,o}$ of Type-III S0 galaxies at $0.4 < z < 0.6$ do not show a similar distribution to the objects in the local Universe. The objects at $0.4 < z < 0.6$ tend to show brighter magnitudes than the objects from the sample at $z = 0$ for similar R_{break} values in all the photometric diagrams. When $\mu_{0,i}$ and $\mu_{0,o}$ are plotted against R_{break}/R_{23} (right panels in Fig. 2), the local galaxies still appear at fainter magnitudes than their $0.4 < z < 0.6$ analogues, but in contrast to the non-normalised diagrams, the objects tend to overlap into one trend in the normalised ones (compare with the left panels in the same figure). In the case of the sample at $0.4 < z < 0.6$, we find a significant correlation of the central surface brightness of the outer disc ($\mu_{0,o}$) with the break radius (R_{break}) and with the normalised break radius (R_{break}/R_{23}). The $0.4 < z < 0.6$ sample does not show any significant correlation at the $\mu_{0,i} \propto \log_{10}(R_{break})$ plane (see Table C.1 in Appendix C), whereas it does in the normalised diagram. We also find a higher median of the R_{23} value at $z \sim 0.5$ compared to $z = 0$ ($R_{23} = 8.46^{+0.38}_{-0.51}$ kpc at $0.4 < z < 0.6$, but $R_{23} = 5.89^{+0.46}_{-0.44}$ kpc in the local sample). This may be due to a general brightening of the surface brightness profiles with z (we comment more on this in Sect. 3.6).

Additionally, in Fig. 2 shows the results from the simulations from B14. As reported there, the simulations present compatible trends and positions in the $\mu_{0,i} \propto \log_{10}(R_{break}/R_{23})$ and $\mu_{0,o} \propto \log_{10}(R_{break}/R_{23})$ with the Type-III S0–E/S0 galaxies from the local sample, except that they are located in the extrapolation towards higher R_{break}/R_{23} values. The trends of S0 galaxies at $0.4 < z < 0.6$, although presenting lower R_{break}/R_{23} values, overlap in these normalised diagrams with the global trend drawn by the local sample and the simulations at higher R_{break}/R_{23} values.

In conclusion we find that the structural scaling relations observed in Type-III S0 galaxies at $z \sim 0.5$ are compatible with those observed in their local analogues and in similar systems formed in major mergers simulations. However, our sample of

A&A 615, A26 (2018)

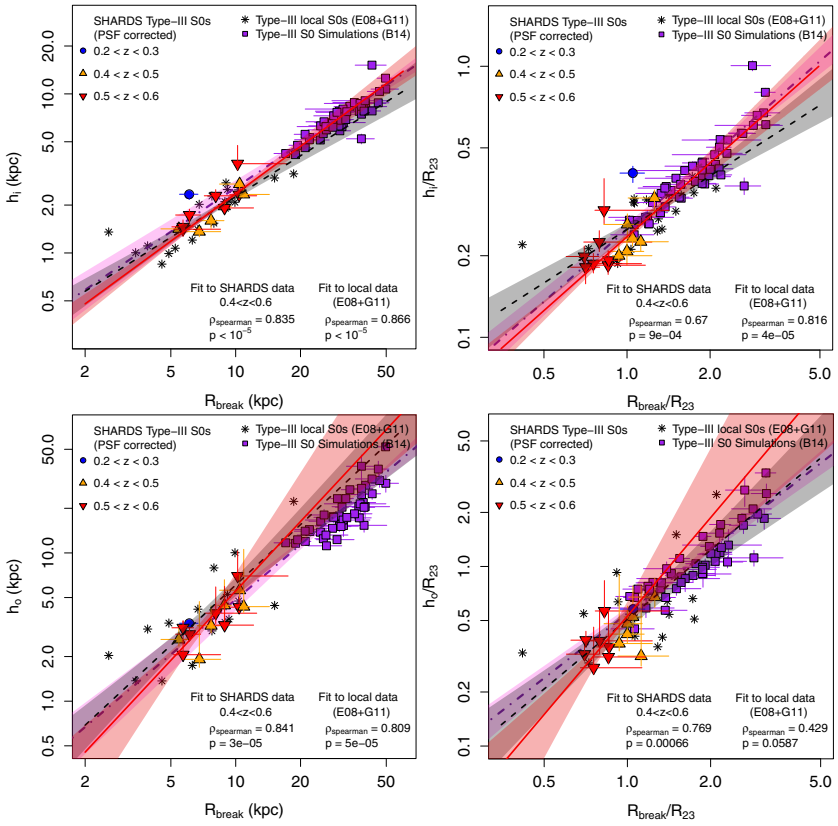

Fig. 1. Distribution of the Type-III S0 galaxies at $0.2 < z < 0.6$ and the local sample from E08 and G11 in the structural diagrams. *Upper left panel*: h_i vs. R_{break}. *Upper right panel*: h_i/R_{23} vs.R_{break}/R_{23}. *Lower left panel*: h_o vs. R_{break}. *Lower right panel*: h_o/R_{23} vs. R_{break}/R_{23}. Solid red line: linear fit to the Type-III S0 galaxies at $0.4 < z < 0.6$. Dashed black line: linear fit to the local Type-III S0 galaxies. Dash-dotted purple line: linear fit to the simulations of Type-III S0 galaxies from B14. Their respective coloured regions represent the 1σ confidence level region of each linear fit. In both cases, the relations fitted were in logarithmic scale in both x and y-axis ($\log_{10}(h_i) \propto \log_{10}(R_{break})$, $\log_{10}(h_i/R_{23}) \propto \log_{10}(R_{break}/R_{23})$, $\log_{10}(h_o) \propto \log_{10}(R_{break})$ and $\log_{10}(h_o/R_{23}) \propto \log_{10}(R_{break}/R_{23})$). We refer to the legend in the figure for the redshift colour classification and correlation tests.

Type-III S0 galaxies at $0.4 < z < 0.6$ present brighter values in the photometric diagrams at the same values of R_{break} or R_{break}/R_{23} when compared with the local Type-III S0s.

3.2. Stellar mass and luminosity in the B and K bands

In Fig. 3 we study if the local Type-III S0 galaxies from E08 and G11 present compatible distributions in stellar mass and in the rest-frame absolute magnitudes in the B and K bands compared to the objects from our sample at $0.4 < z < 0.6$.

The M_B and M_K values for E08 and G11 Type-III S0 galaxies were extracted from the Leda database[3] (Paturel et al. 2003). We use synthetic rest-frame M_B and M_K absolute magnitudes

[3] HyperLeda database for physics of galaxies: http://leda.univ-lyon1.fr

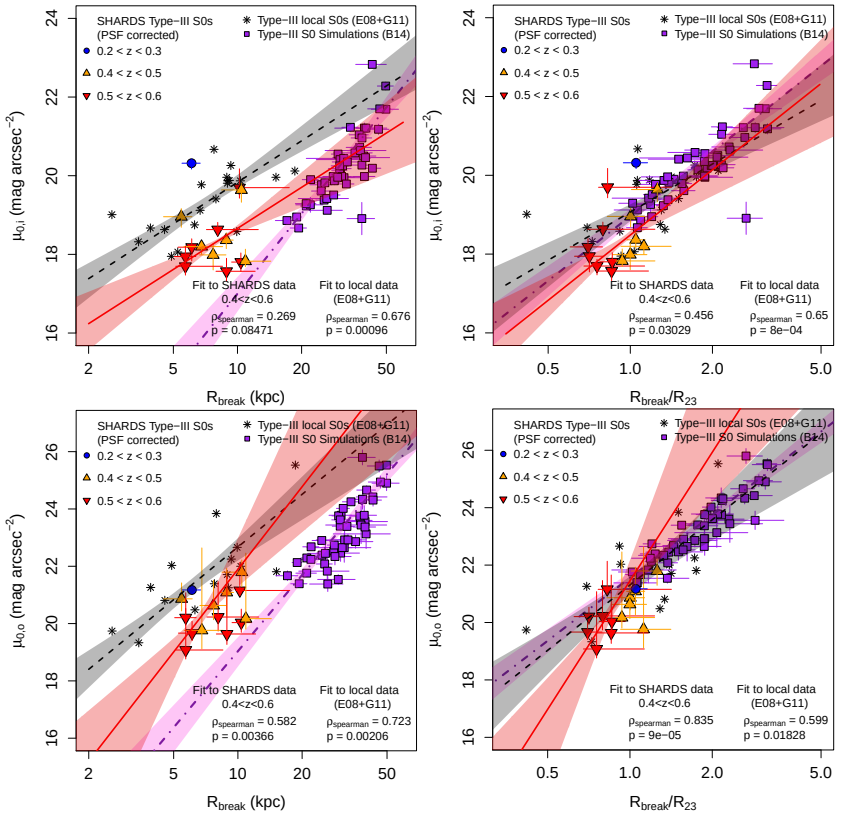

Fig. 2. Distribution of the Type-III S0 galaxies at $0.2 < z < 0.6$ and the local sample from E08 and G11 in the photometric diagrams. *Upper left panel*: $\mu_{0,i}$ vs. $R_{\rm break}$. *Upper right panel*: $\mu_{0,i}$ vs. $R_{\rm break}/R_{23}$. *Lower left panel*: $\mu_{0,o}$ vs. $R_{\rm break}$. *Lower right panel*: $\mu_{0,o}$ vs. $R_{\rm break}/R_{23}$. Solid red line: linear fit to the Type-III S0 galaxies at $0.4 < z < 0.6$. Dashed black line: linear fit to the local Type-III S0 galaxies. Dash-dotted purple line: linear fit to the simulations of Type-III S0 galaxies from B14. Their respective coloured regions represent the 1σ confidence level region of each linear fit. In both cases, the relations fitted were in logarithmic scale for the x-axis ($\mu_{0,i} \propto \log_{10}(R_{\rm break})$, $\mu_{0,i} \propto \log_{10}(R_{\rm break}/R_{23})$, $\mu_{0,o} \propto \log_{10}(R_{\rm break})$ and $\mu_{0,o} \propto \log_{10}(R_{\rm break}/R_{23})$). Consult the legend in the figure for the redshift colour classification and correlation tests.

for the sample at $0.4 < z < 0.6$, available through the Rainbow Database. In the case of the B band, the distribution lies in the range $-18 < M_B < -20.5$ for the sample at $0.2 < z < 0.6$ and $-13 < M_B < -20.5$ for the local Type-III S0s. For the K band, the distribution lies in the range $-20 < M_K < -23$ for the sample at $0.2 < z < 0.6$ and $-15 < M_K < -23$ for the local Type-III S0s.

Total stellar masses are available through the Rainbow Database (Barro et al. 2011a,b) for the sample at $0.4 < z < 0.6$. The stellar masses of 12 objects from the local sample were available from S^{4}G (Muñoz-Mateos et al. 2015), and we found mass estimates for 3 additional ones in (Forbes et al. 2016, NGC 4459 and NGC 7457) and Cano-Díaz et al. (2016, NGC 2880). For comparison, the sample of Type-III S0 galaxies at $z \sim 0$ presents total stellar masses in the range $\log_{10}(M/M_\odot) = [10.0–11.0]$, while the objects from the sample at $0.4 < z < 0.6$ present values in the range $\log_{10}(M/M_\odot) = [9.7–11.2]$. Again, in the case of our intermediate-redshift sample, we only include objects at $0.4 < z < 0.6$, which excludes the object at $z = 0.247$ from our sample.

We show the results for the comparative analysis of the rest-frame absolute magnitudes in the B and K bands and the stellar

A&A 615, A26 (2018)

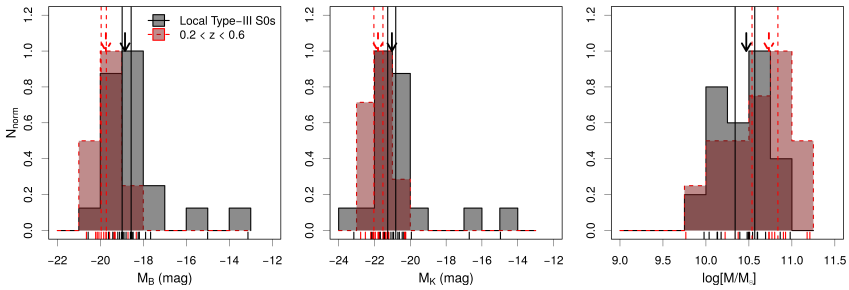

Fig. 3. Normalised distributions of the rest-frame absolute magnitude in the B band (*left panel*), rest-frame absolute magnitude in the K band (*central panel*) and the stellar mass (*right panel*) of our sample of Type-III S0 galaxies at $0.2 < z < 0.6$ compared to those from the local Universe (E08 and G11). Grey histogram with black solid line: Type-III S0 galaxies in the local Universe. Red histogram with dashed line: Type-III S0 galaxies at $0.4 < z < 0.6$ from the SHARDS sample. The red and black arrows represent the median value for the objects at $0.4 < z < 0.6$ and the local sample, respectively. The solid and dashed vertical lines represent the 1σ confidence interval for the median for each sample.

Table 1. Mean rest-frame absolute magnitudes in the B and K bands and mean stellar mass of Type-III S0 galaxies in the local and $0.4 < z < 0.6$ samples.

Parameter		$z \simeq 0$	$0.4 < z < 0.6$	p
(1)		(2)	(3)	(4)
$<M_B>$	[mag]	$-18.85^{+0.28}_{-0.13}$	$-19.74^{+0.02}_{-0.22}$	2.1×10^{-4}
$<M_K>$	[mag]	$-21.02^{+0.21}_{-0.23}$	$-21.80^{+0.27}_{-0.23}$	8.2×10^{-3}
$<\log_{10}(M/M_\odot)>$	[dex]	$10.47^{+0.10}_{-0.13}$	$10.73^{+0.11}_{-0.19}$	6.2×10^{-2}

Notes: Columns: (1) Parameters. (2) Median values for the samples in the local Universe (E08, G11). (3) Median values for the sample at $0.4 < z < 0.6$, with their corresponding 1σ uncertainty intervals. (4) Anderson–Darling test p-value for the null hypothesis of equal parent distributions for the $0.4 < z < 0.6$ and the local Universe samples. Rows from top to bottom: rest-frame absolute magnitudes in the B and K bands and stellar mass.

mass in Table 1 and in Fig. 3. We use the Anderson–Darling criterion (Scholz & Stephens 1987) in order to test whether the parameters from both samples arose from a common unspecified distribution function (null hypothesis). We find that the median values and the distributions of stellar masses are compatible for the objects from the local Universe and our sample at $0.4 < z < 0.6$ ($p > 0.05$ in Table 1, see right panel of Fig. 3). In contrast to that, the rest-frame absolute magnitudes on the B and K bands are significantly brighter at $0.4 < z < 0.6$ when compared to the Type-III S0 galaxies at $z \sim 0$ ($p < 0.05$ in Table 1, see also the corresponding panels in Fig. 3). This result confirms that our sample of Type-III S0 galaxies at $z \sim 0.5$ and the objects from E08 and G11 are comparable in terms of stellar mass and enables us to perform a fair comparison in this sense. However, this analysis also suggests that Type-III S0 galaxies of similar stellar mass were brighter in the past, meaning that they have undergone a significant dimming in the last 6 Gyr. In Sects. 3.5 and 3.6 we study whether this has affected the whole structure or the inner ($\mu_{0,i}$) and outer ($\mu_{0,o}$) profiles in a different way.

3.3. Evolution of R_{break} with z at a fixed stellar mass

With the aim of investigating if the break radius R_{break} presents any signs of evolution with redshift, we follow the method described in Azzollini et al. (2008). In this paper, the authors analysed a sample of Type-II galaxies at several redshift intervals, from the local Universe, up to $z = 1$. In order to compare the break position taking into account the size of each galaxy, the authors estimated the typical value of R_{break} as a function of (1) the Johnson B-band absolute magnitude and (2) the total stellar mass. After this, they compare the expected values for R_{break} at the reference values of $M_B = -20$ and $\log_{10}(M/M_\odot) = 10$ at different redshifts to check whether there is evolution or not. We follow the same procedure to test if there is any noticeable difference in the position of the break (R_{break}) of Type-III S0s between the local universe and our sample at $0.4 < z < 0.6$.

In the left panel of Fig. 4, we show the distribution of R_{break} as a function of the decimal logarithm of the stellar mass $\log_{10}(M/M_\odot)$. We compare the expected values for R_{break} at the reference value of $\log_{10}(M/M_\odot) = 10.50$ at different redshifts to check whether there is evolution or not. This reference value corresponds to the median value for $\log_{10}(M/M_\odot)$ including the Type-III S0 galaxies from E08 and G11 and our sample at $0.2 < z < 0.6$.

In order to do that, we fit a linear model to each sample in the diagram of the left panel of Fig. 4. The uncertainty intervals for each linear fit (i.e. the probability distributions of the intercept and slope) were obtained by performing 100,000 Bootstrapping + Monte Carlo simulations (see Table C.1 in Appendix C). The right column of Fig. 4 presents the normalised probability distributions of R_{break} at the characteristic value of $\log_{10}(M/M_\odot) = 10.50$ for the local Universe sample and the objects at $0.4 < z < 0.6$. These histograms were calculated using the probability distributions of the intercept and slope of each fit for both the local Universe sample and our sample at $0.4 < z < 0.6$ and interpolating each case to the fixed reference value of $\log_{10}(M/M_\odot) = 10.50$.

The main result of this analysis is that we do not find any significant differences between the probability distributions of the break radius R_{break} for Type-III S0 galaxies in the local Universe and their analogues at $0.4 < z < 0.6$ when we take into account

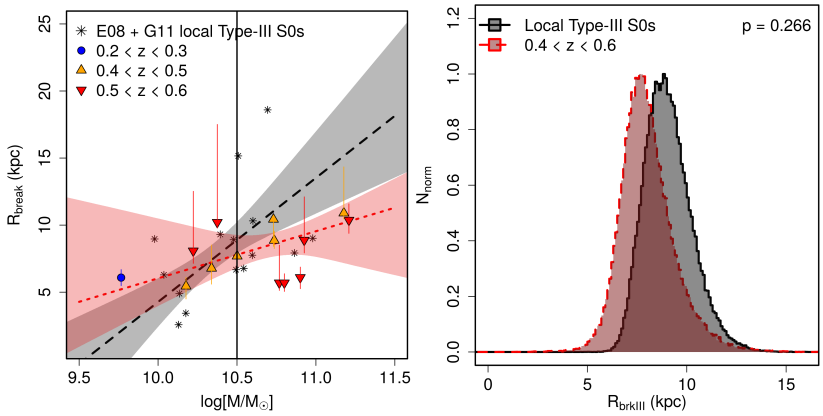

Fig. 4. Position of $R_{\rm break}$ as a function of the stellar mass. *Left panel:* distribution of the break radius $R_{\rm break}$ of Type-III S0 galaxies at $0.4 < z < 0.6$ and at $z \sim 0$ with the stellar mass. The solid vertical black line in the *left panel* represents the fixed value at which we compare the linear fits in the right one. *Right panel*: comparison of the PDDs of the break radius $R_{\rm break}$ at fixed stellar mass $\log_{10}(M/M_\odot) = 10.5$. Grey histogram with black solid line: PDDs for the Type-III S0 galaxies in the local Universe selected from E08 and G11 samples. Red histogram with dashed line: PDDs for the Type-III S0 galaxies at $0.4 < z < 0.6$ from the SHARDS sample. The probability ($p-$value) for both samples to have compatible values of $R_{\rm break}$ at fixed stellar mass of $\log_{10}(M/M_\odot) = 10.5$ is $p = 0.266$ (we refer to the legend in the panels for a key of the different lines and symbols).

the mass of the galaxy. We estimate that the probability of being compatible in $R_{\rm break}$ is $p = 0.260$ when using the stellar mass for the comparison. We have tested whether this result could be dependent on the reference value of the mass that we have chosen. We performed the same test using $\log_{10}(M/M_\odot) = 10.20$ ($p = 0.44$) and 10.80 ($p = 0.08$), finding a similar result: the distributions of $R_{\rm break}$ of S0 galaxies at $0.4 < z < 0.6$ and $z \sim 0$ were statistically compatible even accounting for the mass of the galaxy. Nevertheless, as a consequence of the dispersion in the $R_{\rm break}$ versus $\log_{10}(M/M_\odot)$ diagram and the limited size of both local and $0.4 < z < 0.6$ samples, we cannot rule out variations on the $R_{\rm break}$ lower than $\Delta R_{\rm break} \sim 3$ kpc between $z \sim 0.5$ and $z \sim 0$ for the reference value, which corresponds to the mean range between the 0.025 and 0.975 quantiles of the distributions of $R_{\rm break}$ at the characteristic value of $\log_{10}(M/M_\odot) = 10.50$ (see the left panel of Fig. 4).

Finally, we conclude that we do not find any significant difference between the position of $R_{\rm break}$ of local Universe Type-III S0 galaxies and those at $0.4 < z < 0.6$ for similar masses. This result poses strong constraints on the evolution mechanisms that rule the formation of these structures.

3.4. Evolution of $h_{\rm i}$ and $h_{\rm o}$ with z at a fixed stellar mass

We repeat the previous analysis in order to investigate whether or not there is any significant difference between the scale lengths of the inner and outer profiles ($h_{\rm i}$ and $h_{\rm o}$) between the samples at $z \sim 0.5$ and $z \sim 0$ at a fixed stellar mass. In the left panels of Fig. 5, we show the distributions of $h_{\rm i}$, $h_{\rm o}$ and the ratio $h_{\rm o}/h_{\rm i}$ as a function of the decimal logarithm of the stellar mass $\log_{10}(M/M_\odot)$. Again, we fit a linear model to each sample in the diagrams of the left column of Fig. 5. The results are shown in Table C.1 of Appendix C. The panels of the right column present the normalised probability distributions of $h_{\rm i}$, $h_{\rm o}$ and $h_{\rm o}/h_{\rm i}$ at the characteristic value of $\log_{10}(M/M_\odot) = 10.50$ for the local Universe sample and the objects at $0.4 < z < 0.6$ obtained from the fits performed in the corresponding left panels.

As in the case of $R_{\rm break}$, we do not find any significant differences between the expected values of $h_{\rm i}$, $h_{\rm o}$ or the ratio $h_{\rm o}/h_{\rm i}$ at fixed stellar mass $\log_{10}(M/M_\odot) = 10.50$ between the Type-III S0 galaxies at $z \sim 0$ and our sample at $0.4 < z < 0.6$. We find that the probability that the samples are in $h_{\rm i}$ and $h_{\rm o}$ is $p = 0.397$ and $p = 0.272$, respectively, when using the stellar mass for the comparison. Additionally, we do not find any significant difference between the ratio $h_{\rm o}/h_{\rm i}$ of the samples at $z \sim 0$ and $0.4 < z < 0.6$ either ($p = 0.247$), despite the large $h_{\rm o}/h_{\rm i}$ ratios ($h_{\rm o}/h_{\rm i} > 5$) shown by two of the Type-III S0 galaxies of the local sample (NGC 3900 and NGC 3998).

We conclude that we do not find any significant differences between the general structure of local Type-III S0 galaxies and those of our sample at $0.4 < z < 0.6$ at a fixed stellar mass of $\log_{10}(M/M_\odot) = 10.50$. This result agrees well with the observed similarity of the structural scaling relations of $h_{\rm i}$ and $h_{\rm o}$ with $R_{\rm break}$ and $R_{\rm break}/R_{23}$ (see Fig. 1 on Sect. 3.1).

3.5. Evolution of $\mu_{\rm break}$, $\mu_{0,\rm i}$ and $\mu_{0,\rm o}$ with z at a fixed stellar mass

Finally, we extend the previous analysis to analyse whether or not there is any significant differences between the $\mu_{\rm break}$, $\mu_{0,\rm i}$ and $\mu_{0,\rm o}$ values of the surface brightness profiles of the Type-III S0 galaxies from the local sample and our sample at $0.4 < z < 0.6$, taking into account the stellar mass. In Fig. 6 we present the distributions of $\mu_{\rm break}$, $\mu_{0,\rm i}$ and $\mu_{0,\rm o}$ as functions of the decimal logarithm of the stellar mass $\log_{10}(M/M_\odot)$. We fit a linear model

A&A 615, A26 (2018)

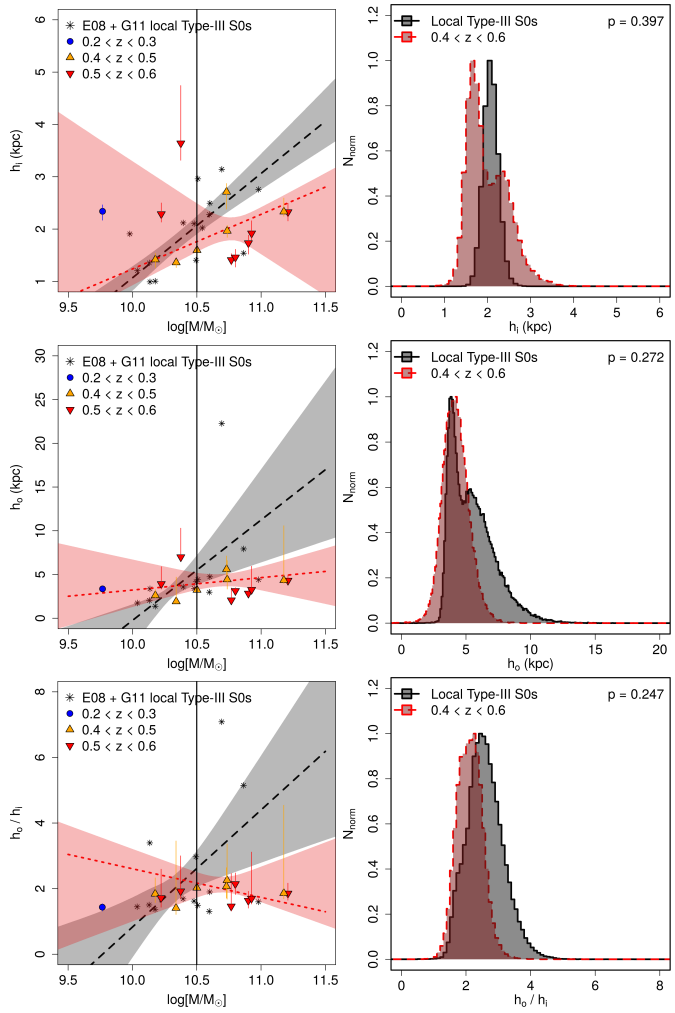

Fig. 5. Scale-lengths of the inner (h_i, top row) and outer profiles (h_o, middle row) and the ratio h_o/h_i (bottom row) as a function of the stellar mass. *Left column:* distribution of h_i, h_o and h_o/h_i of Type-III S0 galaxies at $0.2 < z < 0.6$ and at $z \sim 0$ with the stellar mass. The solid vertical black lines in the *left panel* represent the fixed value at which we compare the linear fits in the right one. *Right column:* comparison of the PDDs of the scale lengths h_i, h_o and the ratio h_o/h_i at fixed stellar mass $\log_{10}(M/M_\odot) = 10.5$. Grey histogram with black solid line: PDDs for the Type-III S0 galaxies in the local Universe selected from E08 and G11 samples. Red histogram with dashed line: PDDs for the Type-III S0 galaxies at $0.4 < z < 0.6$ from the SHARDS sample. The probabilities (p-value) for both samples to have compatible values at fixed stellar mass of $\log_{10}(M/M_\odot) = 10.5$ are $p = 0.397$ (h_i), $p = 0.272$ (h_o) and $p = 0.247$ (h_o/h_i). We refer to the legend in the panels for a key of the different lines and symbols.

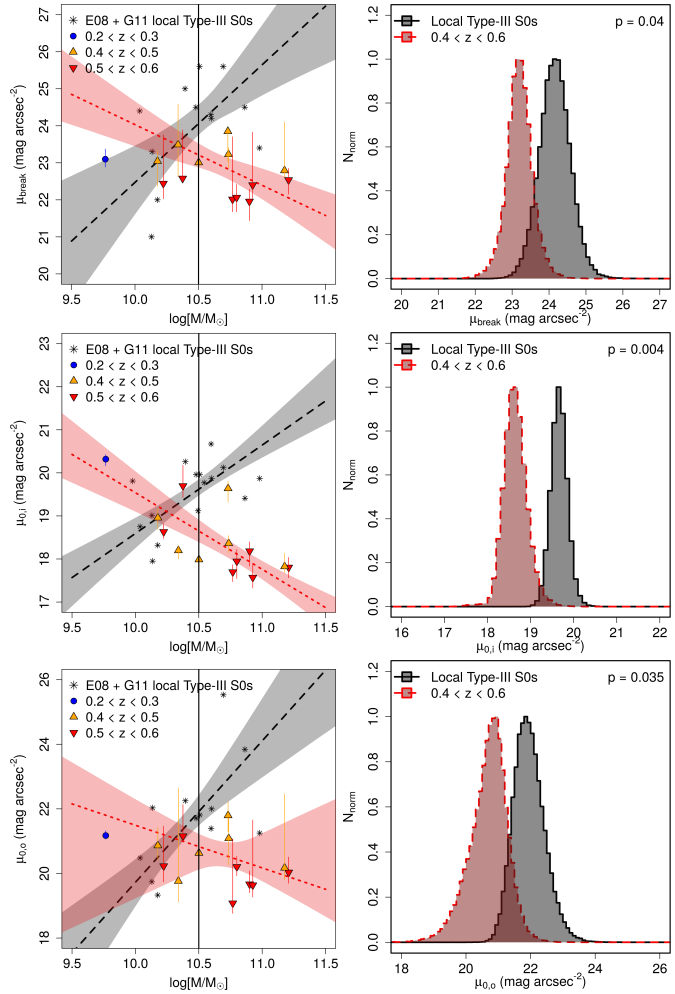

Fig. 6. Surface brightness of the break radius ($\mu_{\rm break}$, top row) and central surface brightness of the inner ($\mu_{0,\rm i}$, central row) and outer profiles ($\mu_{0,\rm o}$, bottom row) as a function of the stellar mass. *Left column:* distribution of $\mu_{\rm break}$, $\mu_{0,\rm i}$ and $\mu_{0,\rm o}$ of Type-III S0 galaxies at $0.2 < z < 0.6$ and at $z \sim 0$ with the stellar mass. The solid vertical black lines in the *left panel* represent the fixed value at which we compare the linear fits in the *right panel*. *Right column:* comparison of the PDDs of $\mu_{\rm break}$, $\mu_{0,\rm i}$ and $\mu_{0,\rm o}$ at fixed stellar mass $\log_{10}(M/M_\odot) = 10.5$. Grey histogram with black solid line: PDDs for the Type-III S0 galaxies in the local Universe selected from E08 and G11 samples. Red histogram with dashed line: PDDs for the Type-III S0 galaxies at $0.4 < z < 0.6$ from the SHARDS sample. The probabilities (p-value) that both samples have compatible values at fixed stellar mass of $\log_{10}(M/M_\odot) = 10.5$ are $p = 0.04$ ($\mu_{\rm break}$), $p = 0.004$ ($\mu_{0,\rm i}$) and $p = 0.035$ ($\mu_{0,\rm o}$). We refer to the legend in the panels for a key of the different lines and symbols.

A&A 615, A26 (2018)

to each sample in the diagrams of the left column of the figure (see Table C.1 in Appendix C). Again, the panels of the right column present the normalised probability distributions of $\mu_{\rm break}$, $\mu_{0,\rm i}$ and $\mu_{0,\rm o}$ at the characteristic value of $\log_{10}(M/M_\odot) = 10.50$ for the local Universe sample and the objects at $0.4 < z < 0.6$ according to the fits performed in the left panels.

We find that the Type-III S0 galaxies from the local Universe and our sample at $0.4 < z < 0.6$ do not present compatible distributions in the diagrams of $\mu_{\rm break}$, $\mu_{0,\rm i}$ and $\mu_{0,\rm o}$ versus $\log_{10}(M/M_\odot)$ for a fixed stellar mass. Interestingly, the linear fits to the local Universe sample present opposite trends to those drawn by our sample at $0.4 < z < 0.6$. The distributions of the surface brightness parameters of the two samples are approximately compatible for the lower stellar mass range ($\log_{10}(M/M_\odot) \sim 10$) but not at higher values of the stellar mass. Nevertheless, this result has to be treated carefully, because we do not have enough objects with ($\log_{10}(M/M_\odot) \leq 10$) to perform any conclusive analysis. In contrast to this, we find that there is a clear separation between the distribution of both samples at the intermediate to high mass range. We quantitatively analyse this in the panels of the left column of Fig. 6. The Type-III S0 galaxies at $0.4 < z < 0.6$ present brighter values for $\mu_{\rm break}$ ($p = 0.04$), $\mu_{0,\rm i}$ ($p = 0.004$) and $\mu_{0,\rm o}$ ($p = 0.035$) by $\sim$1.5 mag arcsec^{-2} for a fixed value of $\log_{10}(M/M_\odot) = 10.5$ than their local analogues. This result is compatible with the lack of agreement between the trends followed by each sample in the diagrams of Fig. 2, and suggests that the dimming observed in Fig. 3 affects similarly to the inner and outer profiles of the disc. Therefore, these galaxies have probably experienced a global dimming in the whole disc structure.

We conclude that the surface brightness profiles from Type-III S0 galaxies at $0.4 < z < 0.6$ are significantly brighter than similar objects in the local Universe at a fixed stellar mass of $\log_{10}(M/M_\odot) = 10.5$.

3.6. Evolution of the $\mu_{\rm break}$ vs. $R_{\rm break}$ relation with z

In Fig. 7 we present $\mu_{\rm break}$ as a function $R_{\rm break}$ for the local sample and our sample at $0.2 < z < 0.6$. Their distributions show a clear separation between the samples at different redshifts. This goes in the sense that objects at higher z tend to present brighter $\mu_{\rm break}$ values than those at lower z. In B14, the authors reported a strong correlation between $\mu_{\rm break}$ and $R_{\rm break}$ for local Type-III S0 galaxies. In this study, we analyse if there is a significant trend with z embedded into the $\mu_{\rm break}$ vs. $R_{\rm break}$ relation.

In the left panel of Fig. 7 we compare the trend followed by Type-III S0s at $z \sim 0$ and $0.4 < z < 0.6$ by fitting the following 3D model to the data:

$$\mu_{\rm break} = 3.68^{+0.79}_{-1.03} \times \log_{10}(R_{\rm break}) - 2.49^{+0.71}_{-0.67} \times z + 20.73^{+0.96}_{-0.72}. \quad (1)$$

We have used the least-squares method to minimise the 3D model, using Bootstrapping and Monte Carlo simulations to estimate the uncertainties of the final fit. Additionally, we use these simulations to estimate the probability for each coefficient of being equal to zero. The coefficients for $R_{\rm break}$ and z have significance levels of $p = 9.9 \times 10^{-4}$ and $p = 4.4 \times 10^{-4}$, respectively. Therefore, there is a statistically significant evolution in surface brightness between the local and $0.2 < z < 0.6$ samples, confirming the results in Fig. 6. This fact would explain why the photometric relations shown in Fig. 2 present a displacement towards brighter magnitudes with respect to those of the local Universe sample. Additionally, note that a global dimming of the Type-III S0 galaxies since $z \sim 0.6$ does not affect the structural relations at different redshifts (see Sect. 3.1 and Fig. 1).

3.6.1. Effect of the limiting magnitude on the measured global dimming

We studied the possibility that the variation in the limiting magnitude as a function of z may systematically bias the $\mu_{\rm break}$ versus z distribution towards brighter values with increasing redshift, creating an apparent correlation. The median limiting magnitude for the F775W profiles is $\mu_{\rm F775W,lim} = 27.092^{+0.024}_{-0.032}$ mag arcsec^{-2} (see Sect. 2.4 on Paper I). Taking into account the K-correction, the Milky Way dust extinction and the cosmological dimming (Sect. 2.5, Paper I), the limiting magnitude in the rest-frame R-band can be approximated as:

$$\mu_{\rm R,lim} = 27.432^{+0.041}_{-0.053} - 1.619^{+0.065}_{-0.072} \times z - 10 \times \log_{10}(1+z). \quad (2)$$

In addition to this, we have to take into account that in order to properly detect a break we need to adequately detect the outer profile. We estimated how many magnitudes brighter a typical Type-III profile must be than the limiting magnitude in order to be detected. We created a simulated surface brightness profile using the median values from the sample of local Type-III S0 galaxies from E08 and G11 (see Table 2 in Paper I). We modified the limiting magnitude from 27 to 24 mag arcsec^{-2}, analysing with `Elbow` the probability in each profile of detecting the Type-III break at a certain limiting magnitude. We find that in order to detect a Type-III break at a 99% confidence level, the surface brightness at the break radius ($\mu_{\rm break}$) must be at least 1.1 ± 0.5 mag arcsec^{-2} brighter than the limiting magnitude of the surface brightness profile. In Fig. 7 we represent with dashed-dotted horizontal segments the limiting magnitude at which we would detect a Type-III profile according to the limiting magnitude of our images and the results from the simulations with `Elbow` ($\mu_{\rm lim,break} = \mu_{\rm lim} - 1.1$). The results show that the Type-III breaks appear to be at least one magnitude brighter than the theoretical limit where we would be able to detect them. This difference is more noticeable for the objects at higher redshift ($0.5 < z < 0.6$). Therefore, our results concerning the global dimming by $\sim$1.5 mag arcsec^{-2} of the whole disc structure of Type-III S0s since $z \sim 0.6$ are not affected by the limiting magnitude of the data.

3.6.2. Effect of the galaxy inclination on the measured global dimming

We tested whether or not the differences between the surface brightness at the break radius $\mu_{\rm break}$ for the sample of Type-III S0 galaxies at $z = 0$ and our sample at $0.2 < z < 0.6$ can be explained as an effect of inclination. Graham (2001) demonstrated that high-inclination galaxies can present central surface brightness values that are significantly greater in the K-band than those of low-inclination galaxies. If the galaxy system is optically thin (transparent) the total magnitude should be the same, regardless of the apparent inclination. Nevertheless, for a disc-like morphology, the projected area decreases with the inclination angle to the observer. Therefore, the surface brightness should increase with the inclination angle. The author presented the following inclination correction model:

$$\mu_{\rm face-on} = \mu_{\rm incl} - 2.5 \cdot C \cdot \log_{10}(b/a), \quad (3)$$

where $\mu_{\rm face-on}$ is the inclination-corrected surface brightness, $\mu_{\rm incl}$ is the measured surface brightness, and C is the optical depth of the system ($C = 1$ for an optically thin galaxy, $C = 0$ for an optically thick galaxy). Lenticular galaxies can be approximated as optically thin systems, because of their lower levels

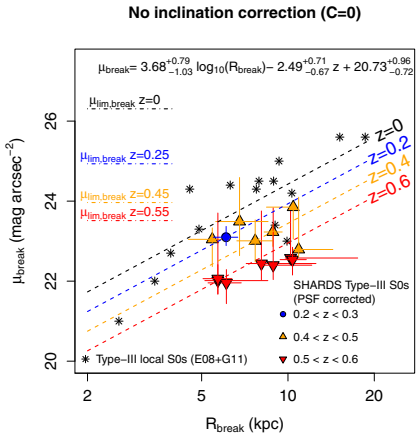

Fig. 7. Distribution of the Type-III S0 galaxies at $0.2 < z < 0.6$ vs. the local sample from E08 and G11 in the $\mu_{\rm break} - R_{\rm break}$ diagram. The relation fitted was in logarithmic scale for the x-axis. The 3D model analysis for the $\mu_{\rm break}$ values without inclination correction is also shown. Dashed lines: contours of equal redshift for the surface brightness at the break radius ($\mu_{\rm break}$) as a function of $R_{\rm break}$ and redshift (from Eq. (1)). Dashed-dotted lines: detection limit for Type-III profiles as a function of redshift. Consult the legend in the figure for the redshift colour classification and 3D fit results.

of gas and intergalactic dust compared to those of spiral galaxies. However, dust lanes have been frequently observed in nearby S0 galaxies (Annibali et al. 2010; Finkelman et al. 2010). As a consequence of this, assuming a uniform and thick optical depth would be an oversimplification of reality, and a blind application of this type of correction may introduce additional uncertainties in the final results. Thus, in order to estimate to what point our results can be affected by the inclination effects, we assume the worst scenario by applying the maximum inclination correction ($C = 1$, see left panel of Fig. 8) and compare the results with the non-inclination-corrected $\mu_{\rm break}$ versus $R_{\rm break}$ diagram in Fig. 7.

We measured the inclination from our Type-III S0 galaxies using `GALFIT3.0`, during the 2D modelling step needed for the PSF-correction. In their papers, E08 and G11 provide the inclination angles for their sample. We transform from inclination angles to axis ratios using the following expression:

$$i = \cos^{-1}\left(\sqrt{\frac{q^2 - q_0^2}{1 - q_0^2}}\right), \quad (4)$$

where q is the minor-to-major axis ratio (b/a) and q_0 is the intrinsic axis ratio. We assume that $q_0 = 0.25$, which is the median value expected for S0 galaxies following the results from Weijmans et al. (2014). In the left panel of Fig. 8 we analyse the variation of $\mu_{\rm break}$ after inclination correction with $R_{\rm break}$ and z. Again, we fit the distribution to a three-dimensional (3D) model, obtaining:

$$\mu_{\rm break} = 4.15^{+0.71}_{-0.93} \times \log_{10}(R_{\rm break}) - 2.26^{+0.72}_{-0.68} \times z + 20.76^{+0.84}_{-0.63}. \quad (5)$$

We find that the coefficients for $R_{\rm break}$ and z have a significance level of $p = 6.4 \times 10^{-4}$ and $p = 4.1 \times 10^{-3}$ respectively. The p-value of the dependence with z is higher than in the case of no inclination correction, therefore, this means that the differences between both samples are partially reduced if we assume the maximum inclination correction, but it is not enough to fully explain the observed trend of $\mu_{\rm break}$ and $R_{\rm break}$ with z, as observed in the right panel of Fig. 7. The 3D model predicts a dimming in brightness of $\Delta\mu_{\rm break} \sim -1.32^{-0.42}_{+0.45}$ mag arcsec^{-2} between $z = 0.6$ and $z = 0$ if we take into account the maximum inclination correction (left panel, Fig. 8) against the $\Delta\mu_{\rm break} \sim -1.49^{-0.37}_{+0.39}$ mag arcsec^{-2} measured dimming of the $\mu_{\rm break}$ without inclination corrections (Fig. 7).

3.6.3. Effect of the objects with higher stellar masses on the measured global dimming

Finally, we tested if the observed variation of $\mu_{\rm break}$ with z could be a bias effect created by the objects from the $0.2 < z < 0.6$ sample with higher masses. We removed SHARDS10009610 ($\log_{10}(M/M_\odot) = 11.209$, $z = 0.557$) and SHARDS20000827 ($\log_{10}(M/M_\odot) = 11.177$, $z = 0.409$) from the $0.2 < z < 0.6$ sample. These are the only two objects that present larger stellar masses than the most massive object from the local sample (NGC 4459, $\log_{10}(M/M_\odot) = 10.98$). We then repeated the 3D fit with this sub-sample. The new $\mu_{\rm break}$ versus $R_{\rm break}$ diagram is presented in the right panel of Fig. 8. We obtained the following results from the 3D fit analysis:

$$\mu_{\rm break} = 3.98^{+0.74}_{-0.98} \times \log_{10}(R_{\rm break}) - 2.25^{+0.63}_{-0.67} \times z + 20.47^{+0.91}_{-0.68}. \quad (6)$$

We find that the coefficients for $R_{\rm break}$ and z have a significance level of $p = 1.2 \times 10^{-3}$ and $p = 1.8 \times 10^{-3}$, respectively. In a similar way as done with the inclination correction test, both p-values of the dependence with z and $R_{\rm break}$ are higher than in the full sample case without inclination correction, but still significant. The 3D model predicts a dimming in brightness of $\Delta\mu_{\rm break} \sim -1.35^{-0.37}_{+0.40}$ mag arcsec^{-2} between $z = 0.6$ and $z = 0$, which is lower than in the case with the full sample but compatible within errors. Therefore, the presence of objects with higher stellar masses is not enough to fully explain the observed trend of $\mu_{\rm break}$ and $R_{\rm break}$ with z. We conclude that there is a significative dimming trend in the $\mu_{\rm break}$ versus $R_{\rm break}$ diagram with z, independently of inclination effects and the limiting magnitude of the data. Considering that there is no significant evolution in $R_{\rm break}$ between $z = 0.6$ and $z = 0$ (see Sect. 3.3), Type-III S0 galaxies in the local Universe are ~1.5 mag arcsec^{-2} dimmer than analogous objects at $z = 0.6$.

In addition to this, the central surface brightnesses $\mu_{0,\rm i}$ and $\mu_{0,\rm o}$ of Type-III S0s at $z \sim 0.5$ are also brighter by ~1.5 mag arcsec^{-2} than their local analogues (see Figs. 2 and 6), while they present similar $h_{\rm i}$ and $h_{\rm o}$ values (see Figs. 2 and 6). Therefore, the dimming seems to affect the whole disc structure of these Type-III S0s (i.e., both the inner and outer profiles). Nevertheless, we note that our sample size is small, and therefore these results must be interpreted with care. Deeper and more complete observations are necessary to confirm this evolution in brightness for Type-III S0 galaxies since $z = 0.6$. We analyse the possible consequences of a general dimming of 1.5 mag arcsec^{-2} of the surface brightness profiles of these galaxies between $z = 0.6$ and $z = 0$ in Sect. 3.8.

A&A 615, A26 (2018)

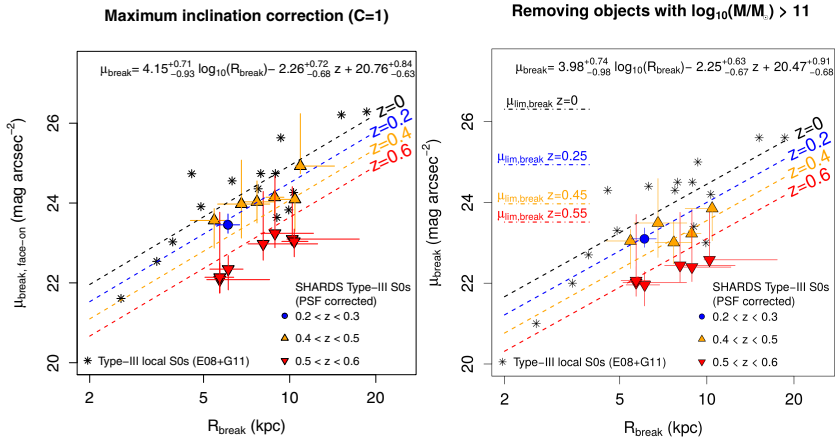

Fig. 8. Distribution of the Type-III S0 galaxies at $0.2 < z < 0.6$ vs. the local sample from E08 and G11 in the $\mu_{\rm break} - R_{\rm break}$ diagram. The relation fitted was in logarithmic scale for the x-axis. *Left panel*: diagram and 2D model analysis for the $\mu_{\rm break}$ values with maximum inclination correction ($C = 1$, optically transparent). *Right panel*: diagram and 2D model analysis for the $\mu_{\rm break}$ values without inclination correction, removing the objects with stellar masses larger than the local sample (SHARDS10009610 and SHARDS20000827). Dashed lines: contours of equal redshift for the surface brightness at the break radius ($\mu_{\rm break}$) as a function of $R_{\rm break}$ and redshift (from Eq. 1). Dashed-dotted lines: detection limit for Type-III profiles as a function of redshift. Consult the legend in the figure for the redshift colour classification and 3D fit results.

3.7. Colour profiles

In Fig. 9 we show the median profiles in the corrected (i.e. corrected for galactic dust, cosmological dimming and K-correction) rest-frame B and R bands and the median $(B - R)$ colour profiles of the Type-III S0 galaxies at $0.2 < z < 0.6$. We present the surface brightness profiles as a function of the galactocentric radius normalised by the break radius ($R/R_{\rm break}$). The upper row of Fig. 9 presents the median surface brightness profile in the rest-frame R band obtained by two different methods: one using the F775W data and another using F850LP data. The agreement between both profiles is excellent, and they confirm two major assumptions in Paper I and the present work: (1) we can apply a K-correction across $0.2 < z < 0.6$ as a function of redshift for any E/S0 and S0 object as computed in Paper I, and (2) the structure of the surface brightness profiles of the galaxies does not change drastically within these filters. In order to ensure the validity of our results, we also analysed the surface brightness profiles using the F850LP corrected band and compared the results to the values of the F775W band. We present the results in Fig. B.1 (see Appendix B). We conclude that the results are compatible between both bands with a median dispersion of $\Delta R_{\rm break} \sim 25\%$ and $\Delta\mu_{\rm break} \sim 0.525$ mag arcsec^{-2}.

In the lower row of Fig. 9, we present the B-band and the $(B - R)$ median profiles. For all bands, the break is clearly visible in the median surface brightness profiles. This ensures that we have enough signal in the outer parts of the objects to analyse their colour profile. In addition to this result, we found that there is not a clear difference between the inner and outer colour profile in the mean $(B - R)$ profile. The median values for the colour $(B - R)$ are $1.310^{+0.077}_{-0.040}$ mag arcsec^{-2} in the inner region and $1.208^{+0.029}_{-0.017}$ mag arcsec^{-2} in the outer region. This difference of $\Delta(B - R) \sim 0.1$ between the colours of the inner and outer regions of Type-III S0 galaxies in our sample is significant at a level of $p \sim 0.039$. Thus, we do not find any strong differences between the inner and outer median profiles of Type-III S0–E/S0 galaxies.

The results from Bakos et al. (2008) in Type-III spiral galaxies show that these initially appear slightly blue at the inner regions followed by a reddening toward the break radius. Nevertheless, the amplitude of this colour change is $\Delta(g' - r') \simeq 0.1$. This blue-to-red trend is not observed in our median $(B - R)$ profile, which appears to be mostly flat (bottom-right panel in Fig. 9). This result can be interpreted as a consequence of the low SFR values of S0 galaxies along their whole disc compared to the spirals. These latter cases are expected to produce more complex colour profiles due to the different star formation levels in their discs.

Nevertheless, we find some objects with significant differences between the inner and outer parts of their individual colour profiles. The surface brightness profiles in the B and R bands, as well as the rest-frame colour profiles are available in Appendix D. Some of them present bluer colours in their outskirts (SHARDS10000840, SHARDS10002942, SHARDS10003647 and SHARDS20000827), while others appear to present a reddening of their outer parts when compared to the inner regions (SHARDS10000327 and SHARDS10002730). The rest of the cases present mostly flat colour profiles. In no cases are the differences between the inner and outer profiles of the individual galaxies larger than 0.35 mag arcsec^{-2}. We conclude that although there are significant differences between some regions of individual galaxies in

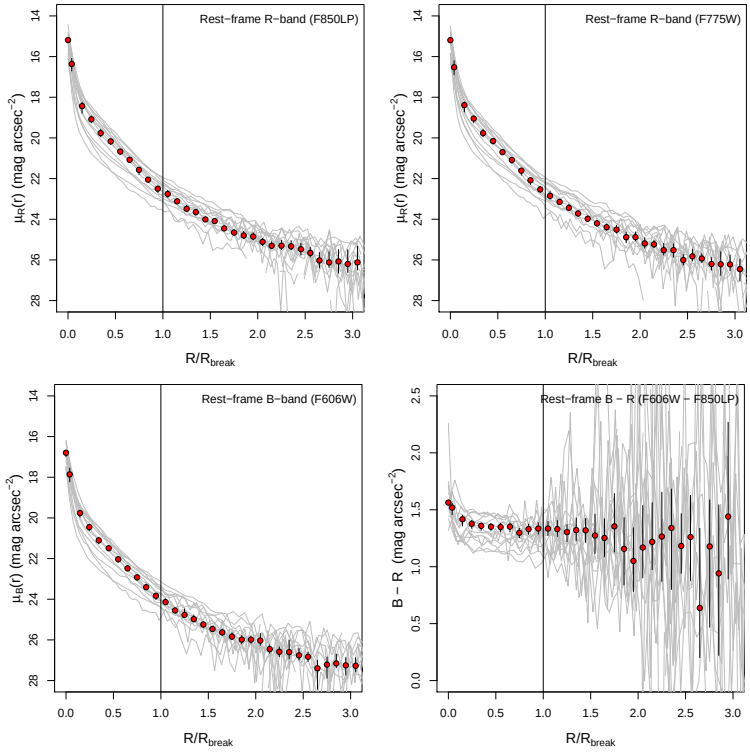

Fig. 9. Median profiles for the sample of Type-III S0–E/S0 galaxies at $0.2 < z < 0.6$, as a function of the normalised radius ($R/R_{\rm break}$). *Top left panel*: median surface brightness profile in the R band, obtained from the F850LP band of HST/ACS. *Top right panel*: median surface brightness profile in the R band, obtained from the F775W band of HST/ACS. *Bottom left panel:* median surface brightness profile on the B band, obtained from the F606W band of HST/ACS. *Bottom right panel*: median $(B - R)$ colour profile. The vertical solid lines represent the break radius for all the profiles ($R/R_{\rm break} = 1$). Red dots represent the median profiles in each case. The grey lines represent the individual profiles for each object.

their colour profiles, in general, there is no difference between the inner and outer median profiles of Type-III S0–E/S0 galaxies at $0.2 < z < 0.6$.

3.8. Stellar population evolution analysis

Finally we analyse if a decay of $\Delta\mu = -1.5$ mag arcsec^{-2} from $z \sim 0.6$ to $z = 0$ is compatible with the passive evolution expected for several SSP models. In order to do so, we take advantage of the E-MILES[4] stellar population synthesis models (Vazdekis et al. 2016). We simulate the magnitude in the R band of an SSP burst with different ages (from 0 to 14 Gyr) and metallicities ($[M/H] = -0.96, -0.35, -0.25, +0.06$ and $+0.15$). We assume a Kroupa universal initial mass function (IMF, Kroupa 2001) with a slope of 1.3 and a BaSTI isocrone (Pietrinferni et al. 2004) transformed to the observational plane, following empirical relations (Alonso et al. 1996, 1999).

The results are shown in Fig. 10. The top panel shows the estimated dimming in surface brightness of an SSP burst between $z = 0$ and $z = 0.6$ as a function of the lookback time of the redshift at which the burst takes place for several metallicities. Given that we want to compare with the observed dimming since $z = 0.6$ in $\mu_{\rm break}$, we set the minimum limit for the start of the SSP burst in lookback time to ~5.7 Gyr. The results show that a SSP burst would present a surface brightness magnitude ~1.5 mag arcsec^{-2} brighter at $z = 0.6$ than at $z = 0$ if the burst took place at $z \sim 0.8$–0.9.

[4] E-MILES is available at the MILES/IAC project website http://www.iac.es/proyecto/miles/

A&A 615, A26 (2018)

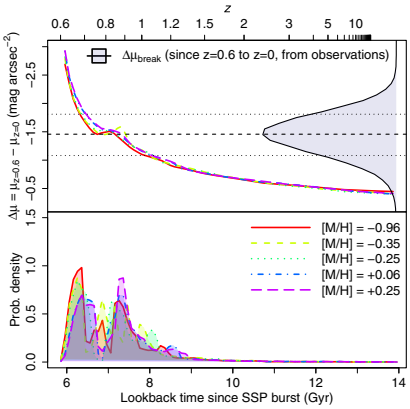

Fig. 10. Analysis of the surface brightness dimming with SSP EMILES models. *Top*: surface brightness magnitude dimming between $z = 0.6$ and $z = 0$ as a function of the age of the SSP model. The five different lines cover a range in metallicities from −0.96 to +0.25. The black vertical histogram represents the probability density of the observed dimming in the surface brightness at the break radius ($\Delta\mu_{\rm break}$) since $z = 0.6$ according to our observational data. *Bottom*: projected probability distributions for the lookback time to the SSP burst, assuming the different SSP models and the observed dimming in $\mu_{\rm break}$. We refer to the legend in the panels for a key of the different lines.

Additionally in the same panel, we represent in a vertical black histogram the PDD of the observed $\mu_{\rm break}$ difference between $z = 0$ and $z = 0.6$ according to Eq. (1). We find that the central regions of the PDD for $\Delta\mu_{\rm break}$ correspond to an age for the SSP burst of ∼ 7 Gyr. In the lower panel of Fig. 10 we present the projected probability for the age of an SSP burst assuming different metallicities and the observed distribution of $\Delta\mu_{\rm break}$ between $z = 0.6$ and $z = 0$. We find that the results for the different metallicities are very similar. The PDDs for the lookback time since an SSP burst present two peaks for most metallicities, one at $z \sim 0.65$–0.7 and a second one at $z \sim 0.9$. This is caused by the low variation of $\Delta\mu$ between $z = 0$ and $z = 0.6$ expected for the SSP models at a lookback time since the SSP burst of ∼7 Gyr.

The upper uncertainty interval of the observed $\Delta\mu_{\rm break}$ is high enough to impede a reasonable determination of the lower limit age of the SSP burst. Nevertheless, we find that the SSP models cannot explain the observed change in surface brightness if the SSP started before $z \sim 1.2$, that is, if the dominating component of the stellar emission is older than ∼ 8 Gyr. Although this result points to a strong constraint in the stellar formation models, we must remark that this is an over-simplified interpretation of the real evolution and formation mechanisms of S0 galaxies. In a forthcoming paper we will perform a deep analysis of the SEDs of these objects with more complex star formation history (SFH) models such as several SSPs and exponentially declining SFHs.

In Fig. 11 we study whether or not the predicted colours from the SSP models are compatible with those obtained from observations in Fig. 9). Again, we represent with different lines the colours of several SSP bursts as a function of their age, as they would be observed at $z = 0.45$ (left panel) and $z = 0.55$ (right panel). The figure shows that the dependence of the colour with the SSP burst metallicity is stronger than in the case of the analysis of the surface brightness dimming in Fig. 10. Additionally, we observe that the uncertainties in the observed colour distributions (0.7–1 mag) for the inner and outer profiles are compatible with the predicted colour at each redshift for a wide range of metallicities and ages, impeding a similar analysis for the age of the SSP burst as done with the surface brightness dimming. For most metallicities, we find SSP models that can reproduce the colour of the profiles of our Type-III S0s at $z \sim 0.5$ if the burst took place at $z > 0.6$. Therefore, we cannot restrict an upper limit to the age of the SSP model simply by analysing the median colours of the discs of Type-III S0s at $z \sim 0.5$. We conclude that the observed distributions of (F606W–F850LP) in Sect. 3.7 of the inner and outer profiles are compatible with the predicted (F606W-F850LP) colours from SSP models with ages >6–7 Gyr, especially with those with intermediate metallicities.

4. Discussion

Any hypothetical formation scenario of Type-III S0 galaxies has to be able to explain several observations presented in this study:

1. The presence of Type-III S0 galaxies since $z \sim 0.6$
2. The small variation (compatible with no significant variation) of $R_{\rm break}$ during the past ∼6 Gyr and the structural stability of its correlation with the inner and outer scale lengths ($h_{\rm i}$ and $h_{\rm o}$).
3. The observed dimming of ∼1.5 mag arcsec^{-2} in surface brightness of Type-III S0 galaxies since $z \sim 0.6$ when comparing to the objects of the same type at $z = 0$ at the same break radius.

Although there is no current agreement with the formation of Type-III galaxies (see Sect. 1), we can summarise all the possible scenarios that have been proposed in three different classes:

1. Spiral galaxies form Type-III profiles in their disc structure and they fade afterwards by secular evolution into S0 galaxies.
2. Type-III profiles form in S0 galaxies after being transformed from spiral galaxies by secular evolution.
3. Type-III profiles form in S0 galaxies that did not evolve passively from spirals, but through gravitational interactions (i.e., mergers).

The latter scenario has previously been studied by Younger et al. (2007) and Borlaff et al. (2014). In these papers the authors demonstrated that Type-III galaxies can be formed through minor and major mergers. Nevertheless, the fact that there are no significant differences between the structural and photometric parameters of spiral and S0 Type-III galaxies at $z = 0$ (Eliche-Moral et al. 2015) suggests that the Type-III profiles may be highly stable structures that can survive passive evolution from spirals into S0 galaxies, preserving their properties. This indicates that Type-III profiles may not be due to transitions between different stellar formation rates or populations, but created by the stellar mass profile of the galaxy, as observed in Bakos et al. (2008). In addition to this, the observed dimming of ∼1.5 mag arcsec^{-2} in the surface brightness profiles of Type-III S0 galaxies between $z = 0.6$ and $z = 0$ without any noticeable change in $R_{\rm break}$ is compatible with a passive evolution of these objects for the last ∼6 Gyr. However, the comparison of this result with SSP models from E-MILES allows us to reject the hypothesis that Type-III S0 galaxies formed preferentially through monolithic collapse before $z = 1.2$, evolving passively since then. If Type-III S0 galaxies are older, they should have

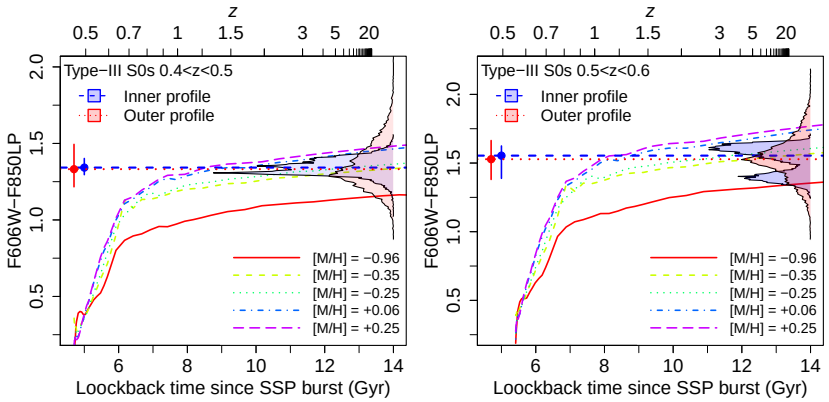

Fig. 11. Analysis of the (F606W – F850LP) colours with SSP EMILES models. *Left panel*: observed (F606W-F850LP) colour at $z = 0.45$ for an SSP burst as a function of the age of the SSP model. *Right panel*: observed (F606W-F850LP) colour at $z = 0.55$ for an SSP burst as a function of the age of the SSP model. The five different lines cover a range in metallicities from −0.96 to +0.25. The blue and red vertical histograms represent the probability density of the observed F606W-F850LP colour in the real Type-III S0 galaxies at $0.4 < z < 0.5$ (left) and $0.5 < z < 0.6$ (right), for the inner and the outer regions with respect to the $R_{\rm break}$. The horizontal dashed and dotted lines represent the median (F606W-F850LP) values of the inner and outer profiles of our data, respectively. We refer to the legend in the panels for a key of the different lines.

more complex SFHs than an SSP (e.g. extended SFHs, gas infall, minor/major mergers, etc.). Finally, radial migration mechanisms (see Herpich et al. 2015, 2017; Ruiz-Lara et al. 2017) should be able to explain why the general structure of the Type-III profiles remain stable after ∼6 Gyr. Nevertheless, there has not yet been a test of whether a Type-III profile caused by radial migration in a barred spiral galaxy would remain stable long enough to survive a secular process of transformation from spirals to S0 galaxies. We conclude that the observed stability of the break radius and the inner and outer scale-lengths since $z \sim 0.6$, as well as the observed dimming of 1.5 mag arcsec^{-2} in the surface brightness profiles since $z \sim 0.6$ to $z = 0$ pose important constraints on the proposed formation mechanisms of Type-III S0 galaxies.

5. Conclusions

We have studied the structural and photometric properties of a sample of Type-III S0–E/S0 galaxies at $0.2 < z < 0.6$ from the GOODS-N field, and compared them to a sample of galaxies of the same type in the local Universe. In order to do that, we have used a sample of Type-III S0-E/S0 galaxies identified by using the F775W band of HST/ACS in a previous paper (Paper I, see Sect. 2). The images of these objects were morphologically classified and corrected for PSF effects. Additionally, their surface brightness profiles were analysed and classified as a function of their shape. In this paper, we also analysed the corresponding images in the adjacent bands F606W and F850LP, in order to study the differences of their colour profiles in the inner and outer regions of the break. Furthermore, we analysed if the surface brightness profile parameters of the Type-III S0 galaxies at $0.4 < z < 0.6$ ($R_{\rm break}$, $\mu_{\rm break}$, $h_{\rm i}$, $h_{\rm o}$, $\mu_{0,{\rm i}}$ and $\mu_{0,{\rm o}}$) present a different distribution to the Type-III S0 galaxies in the local Universe, taking into account the stellar mass of the galaxy. Finally, we studied whether or not there is a significant variation of the surface brightness at the break radius ($\mu_{\rm break}$) with z and compared it with the expected evolution in brightness from a small grid of SSP models.

We found several interesting results. First, we report that several structural scaling relations from those reported in B14 in local S0 Type-III galaxies are also found in Type-III S0–E/S0 galaxies at $0.4 < z < 0.6$ (Sect. 3.1). The structural relations of $h_{\rm i}$ and $h_{\rm o}$ with $R_{\rm break}$ and the normalised break radius ($R_{\rm break}/R_{23}$) of both samples are also compatible with the simulations of Type-III S0 galaxies from B14, and present similar correlations, despite the observational limitations. We have found that the photometric scaling relations (those involving $\mu_{0,{\rm i}}$ and $\mu_{0,{\rm o}}$ as well as $\mu_{\rm break}$) do not present distributions that are compatible with those from the local sample or the simulations. This is due to a general dimming in surface brightness from $z \sim 0.6$ to $z = 0$, which is also visible in the normalised structural diagrams. We found no significant differences between the rest-frame ($B - R$) colours of the inner and outer parts with respect to the break radius $R_{\rm break}$.

Furthermore, we found that there are no significant differences between the positions of the break ($R_{\rm break}$) or the scale-lengths ($h_{\rm i}$ and $h_{\rm o}$) in local Universe Type-III S0 galaxies and our sample at $0.4 < z < 0.6$, taking into account the stellar mass of the galaxy. This strongly contrasts with the results found by Azzollini et al. (2008) in Type-II spiral galaxies, where the authors report that the break radius has increased with time by a factor of 1.3 ± 0.1 since $z \sim 1$ to $z = 0$, in agreement with the inside-out formation scenario of disc galaxies. For Type-III profiles, the stability of the structural scaling relations and the break radius as well as the lack of differences in the rest-frame colours contrast with the evolution of Type-II spiral galaxies, and suggests gravitational and dynamical formation scenarios rather than the evolution of stellar populations. Nevertheless, our

sample is limited to S0 galaxies and a similar study would be necessary to analyse a possible evolution of the break radius in Type-III spiral galaxies.

We find that the distributions of $\mu_{\rm break}$, $\mu_{0,i}$ and $\mu_{0,o}$ from Type-III S0 galaxies at $0.4 < z < 0.6$ are not compatible with those of the local Universe sample. Furthermore, there is a significant dependency of $\mu_{\rm break}$ not only on $R_{\rm break}$ but also on z (see Sect. 3.6). The $\mu_{\rm break}$ of Type-III S0 galaxies at $z \sim 0.6$ appears to be $\sim$1.5 mag arcsec^{-2} brighter than the objects of the same type at $z = 0$ at the same break radius. The cause of this seems to be a general dimming of the whole structure of Type-III S0 galaxies from $z \sim 0.6$ to $z = 0$. In this paper we investigate whether or not a single stellar population (SSP) model can predict a dimming of $\sim$1.5 mag arcsec^{-2} from $z = 0.6$ to $z = 0$ ($\sim$6 Gyr). An instantaneous stellar formation burst should not be older than $\sim$8 Gyr in order to fit the observed change in surface brightness; that is, if the dominant population of Type-III S0 galaxies were formed in a short star formation period, this should have occurred after $z \sim 1.2$. This poses a strong constraint on the proposed formation scenarios of Type-III S0 galaxies. If confirmed, the presence of relatively young stellar populations ($z \lesssim 1.2$) or more extended SFHs during the formation of Type-III S0 galaxies would be favoured over monolithic collapse at high redshift ($z > 2$–3). Nevertheless, this study is strongly limited by the size of the sample. Deeper and more complete observations are required to confirm or reject these results. In a forthcoming paper we intend to present a detailed analysis of the SED and SFH of each object with more complex models and multiple populations to provide more clues to the origin of these structures.

Acknowledgements. We thank the anonymous referee for their detailed comments and suggestions to the original version of this manuscript, which helped to improve it considerably. Supported by the Ministerio de Economía y Competitividad del Gobierno de España (MINECO) under project AYA2012-31277 and project P3/86 of the Instituto de Astrofisica de Canarias. PGP-G acknowledges support from MINECO grants AYA2015-70815-ERC and AYA2015-63650-P. NCL acknowledges support from MINECO grants AYA2013-46724-P and AYA2016-75808-R. This work has made use of the Rainbow Cosmological Surveys Database, which is operated by the Universidad Complutense de Madrid (UCM) partnered with the University of California Observatories at Santa Cruz (UCO/Lick,UCSC). We are deeply grateful to the SHARDS team, since this work would not have been possible without their efforts. Based on observations made with the Gran Telescopio Canarias (GTC) installed at the Spanish Observatorio del Roque de los Muchachos of the Instituto de Astrofísica de Canarias, in the island of La Palma. This paper made use of R: A language and environment for statistical computing (R Core Team 2017, `https://www.R-project.org/`) and Astropy, a community-developed core Python package for Astronomy (Astropy Collaboration et al. 2013, 2018). We thank all the GTC Staff for their support and enthusiasm with the SHARDS project. This work is based on observations taken by the 3D-HST Treasury Program (GO 12177 and 12328) with the NASA/ESA HST, which is operated by the Association of Universities for Research in Astronomy, Inc., under NASA contract NAS5-26555.

References

Abadi, M. G., Moore, B., & Bower, R. G. 1999, MNRAS, 308, 947
Alonso, A., Arribas, S., & Martinez-Roger, C. 1996, A&A, 313, 873
Alonso, A., Arribas, S., & Martínez-Roger, C. 1999, A&AS, 140, 261
Annibali, F., Bressan, A., Rampazzo, R., et al. 2010, A&A, 519, A40
Astropy Collaboration, Robitaille, T. P., Tollerud, E. J., et al. 2013, A&A, 558, A33
Astropy Collaboration, Price-Whelan, A. M., Sipőcz, B. M, et al. 2018, ArXiv e-prints [arXiv:1801.02634]
Athanassoula, E., Rodionov, S. A., Peschken, N., & Lambert, J. C. 2016, ApJ, 821, 90
Azzollini, R., Trujillo, I., & Beckman, J. E. 2008, ApJ, 684, 1026
Bakos, J., Trujillo, I., & Pohlen, M. 2008, ApJ, 683, L103
Baldry, I. K. 2008, Astron. Geophys., 49, 5.25
Barro, G., Pérez-González, P. G., Gallego, J., et al. 2011a, ApJS, 193, 13
Barro, G., Pérez-González, P. G., Gallego, J., et al. 2011b, ApJS, 193, 30
Barway, S., Kembhavi, A., Wadadekar, Y., Ravikumar, C. D., & Mayya, Y. D. 2007, ApJ, 661, L37
Barway, S., Wadadekar, Y., Kembhavi, A. K., & Mayya, Y. D. 2009, MNRAS, 394, 1991
Barway, S., Wadadekar, Y., Vaghmare, K., & Kembhavi, A. K. 2013, MNRAS, 432, 430
Berlind, A. A., Frieman, J., Weinberg, D. H., et al. 2006, ApJS, 167, 1
Bertin, E. & Arnouts, S. 1996, A&AS, 117, 393
Bialas, D., Lisker, T., Olczak, C., Spurzem, R., & Kotulla, R. 2015, A&A, 576, A103
Bland-Hawthorn, J., Vlajić, M., Freeman, K. C., & Draine, B. T. 2005, ApJ, 629, 239
Borlaff, A., Eliche-Moral, M. C., Rodríguez-Pérez, C., et al. 2014, A&A, 570, A103
Borlaff, A., Eliche-Moral, M. C., Beckman, J. E., et al. 2017, A&A, 604, A119
Bournaud, F., Jog, C. J., & Combes, F. 2005, A&A, 437, 69
Cano-Díaz, M., Sánchez, S. F., Zibetti, S., et al. 2016, ApJ, 821, L26
Ciambur, B. C. 2015, ApJ, 810, 120
Comerón, S., Elmegreen, B. G., Salo, H., et al. 2012, ApJ, 759, 98
Cortesi, A., Merrifield, M. R., Coccato, L., et al. 2013, MNRAS, 432, 1010
Crook, A. C., Huchra, J. P., Martimbeau, N., et al. 2007, ApJ, 655, 790
de Vaucouleurs G. 1958, ApJ, 128, 465
D'Onofrio, M., Marziani, P., & Buson, L. 2015, Front. Astron. Space Sci., 2, 4
Dressler, A., Oemler, Jr. A., Couch, W. J., et al. 1997, ApJ, 490, 577
Eliche-Moral, M. C., Borlaff, A., Beckman, J. E., & Gutiérrez, L. 2015, A&A, 580, A33
Eliche-Moral, M. C., Prieto, M., Gallego, J., et al. 2010, A&A, 519, A55
Elmegreen, B. G., & Hunter, D. A. 2006, ApJ, 636, 712
Elmegreen, B. G., & Struck, C. 2016, ApJ, 830, 115
Erwin, P., Beckman, J. E., & Pohlen, M. 2005, ApJ, 626, L81
Erwin, P., Pohlen, M., & Beckman, J. E. 2008, AJ, 135, 20
Finkelman, I., Brosch, N., Funes, J. G., Kniazev, A. Y., & Väisänen, P. 2010, MNRAS, 407, 2475
Forbes, D. A., Sinpetru, L., Savorgnan, G., et al. 2016, MNRAS, 464, 4611
Freeman, K. C. 1970, ApJ, 160, 811
Giavalisco, M., Ferguson, H. C., Koekemoer, A. M., et al. 2004, ApJ, 600, L93
Graham, A. W. 2001, MNRAS, 326, 543
Gunn, J. E., & Gott, III, J. R. 1972, ApJ, 176, 1
Gutiérrez, L., Erwin, P., Aladro, R., & Beckman, J. E. 2011, AJ, 142, 145
Hammer, F., Flores, H., Puech, M., et al. 2009a, A&A, 507, 1313
Hammer, F., Flores, H., Yang, Y. B., et al. 2009b, A&A, 496, 381
Hammer, F., Yang, Y., Flores, H., & Puech, M. 2012, Mod. Phys. Lett. A, 27, 30034
Herpich, J., Stinson, G. S., Dutton, A. A., et al. 2015, MNRAS, 448, L99
Herpich, J., Stinson, G. S., Rix, H.-W., Martig, M., & Dutton, A. A. 2017, MNRAS, 470, 4941
Hubble, E. P. 1926, ApJ, 64, 321
Hubble, E. P. 1927, Observatory, 50, 276
Huchra, J. P. & Geller, M. J. 1982, ApJ, 257, 423
Ilyina, M. A. & Sil'chenko, O. K. 2012, Astronom. Astrophys. Trans., 27, 313
Isobe, T., Feigelson, E. D., Akritas, M. G., & Babu, G. J. 1990, ApJ, 364, 104
Jian, H.-Y., Lin, L., & Chiueh, T. 2012, ApJ, 754, 26
Kazantzidis, S., Zentner, A. R., Kravtsov, A. V., Bullock, J. S., & Debattista, V. P. 2009, ApJ, 700, 1896
Kormendy, J., & Kennicutt Jr., R. C. 2004, ARA&A, 42, 603
Kormendy, J. & Bender, R. 2012, ApJS, 198, 2
Kregel, M., van der Kruit, P. C., & de Grijs R. 2002, MNRAS, 334, 646
Krist, J. E., Hook, R. N., & Stoehr, F. 2011, in Society of Photo-Optical Instrumentation Engineers SPIE Conf. Ser. 81270J, 8127
Kroupa, P. 2001, MNRAS, 322, 231
Laine, J., Laurikainen, E., Salo, H., et al. 2014, MNRAS, 441, 1992
Laurikainen, E. & Salo, H. 2001, MNRAS, 324, 685
Laurikainen, E., Salo, H., Buta, R., Knapen, J. H., & Comerón, S. 2010, MNRAS, 405, 1089
Maltby, D. T., Gray, M. E., Aragón-Salamanca, A., et al. 2012, MNRAS, 419, 669
Maltby, D. T., Aragón-Salamanca, A., Gray, M. E., et al. 2015, MNRAS, 447, 1506
Moore, B., Katz, N., Lake, G., Dressler, A., & Oemler, A. 1996, Nature, 379, 613
Moore, B., Lake, G., Quinn, T., & Stadel, J. 1999, MNRAS, 304, 465
Muñoz-Mateos, J. C., Sheth, K., Regan, M., et al. 2015, ApJS, 219, 3
Naab, T., & Burkert, A. 2003, ApJ, 597, 893
Oke, J. B. 1971, ApJ, 170, 193
Patterson, F. S. 1940, Harvard College Observatory Bulletin, Vol. 914, 9
Paturel, G., Petit, C., Prugniel, P., et al. 2003, A&A, 412, 45

Peñarrubia, J., McConnachie, A., & Babul, A. 2006, ApJ, 650, L33
Peirani, S., Hammer, F., Flores, H., Yang, Y., & Athanassoula, E. 2009, A&A, 496, 51
Peng, C. Y., Ho, L. C., Impey, C. D., & Rix, H.-W. 2002, AJ, 124, 266
Pérez-González, P. G., Rieke, G. H., Egami, E., et al. 2005, ApJ, 630, 82
Pérez-González, P. G., Rieke, G. H., Villar, V., et al. 2008, ApJ, 675, 234
Pérez-González, P. G., Cava, A., Barro, G., et al. 2013, ApJ, 762, 46
Pietrinferni, A., Cassisi, S., Salaris, M., & Castelli, F. 2004, ApJ, 612, 168
Pohlen, M. 2002, Ph.D. thesis, Bochum, Germany
Pohlen, M. & Trujillo, I. 2006, A&A, 454, 759
Pohlen, M., Dettmar, R.-J., & Lütticke, R. 2000, A&A, 357, L1
Prieto, M., Eliche-Moral, M. C., Balcells, M., et al. 2013, MNRAS, 428, 999
Querejeta, M., Eliche-Moral, M. C., Tapia, T., et al. 2015a, A&A, 573, A78
Querejeta, M., Eliche-Moral, M. C., Tapia, T., et al. 2015b, A&A, 579, L2
R Core Team 2017, R: A Language and Environment for Statistical Computing (Vienna, Austria: R Foundation for Statistical Computing)
Roche, N., Bernardi, M., & Hyde, J. 2010, MNRAS, 407, 1231
Rodionov, S. A., Athanassoula, E., & Peschken, N. 2017, A&A, 600, A25
Roediger, J. C., Courteau, S., Sánchez-Blázquez, P., & McDonald, M. 2012, ApJ, 758, 41
Ruiz-Lara, T., Few, C. G., Florido, E., et al. 2017, A&A, 608, A126
Sandin, C. 2014, A&A, 567, A97
Sandin, C. 2015, A&A, 577, A106
Scholz, F. W. & Stephens, M. A. 1987, J. Am. Stat. Assoc., 82, 918
Sérsic, J. L. 1963, Boletin de la Asociacion Argentina de Astronomia La Plata Argentina, 6, 41
Sil'chenko, O. K. 2009, in IAU Symp., Vol. 254, eds. J., Andersen, Nordströara, B. m., & J., Bland-Hawthorn, 173
Skelton, R. E., Whitaker, K. E., Momcheva, I. G., et al. 2014, ApJS, 214, 24
Spergel, D. N., Bean, R., Doré, O., et al. 2007, ApJS, 170, 377
Spitzer Jr. L., & Baade, W. 1951, ApJ, 113, 413
Struck, C. & Elmegreen, B. G. 2017, MNRAS, 469, 1157
Tapia, T., Eliche-Moral, M. C., Querejeta, M., et al. 2014, A&A, 565, A31
Trujillo, I., & Bakos, J. 2013, MNRAS, 431, 1121
Trujillo, I., & Fliri, J. 2016, ApJ, 823, 123
Vaghmare, K., Barway, S., & Kembhavi, A. 2013, ApJ, 767, L33
van der Kruit, P. C. 1979, A&AS, 38, 15
Vazdekis, A., Koleva, M., Ricciardelli, E., Röck, B., & Falcón-Barroso, J. 2016, MNRAS, 463, 3409
Wei, L. H., Kannappan, S. J., Vogel, S. N., & Baker, A. J. 2010, ApJ, 708, 841
Weijmans, A.-M., de Zeeuw, P. T., Emsellem, E., et al. 2014, MNRAS, 444, 3340
Whitaker, K. E., Labbé, I., van Dokkum, P. G., et al. 2011, ApJ, 735, 86
Whitaker, K. E., van Dokkum, P. G., Brammer, G., & Franx, M. 2012, ApJ, 754, L29
Wilman, D. J., Oemler Jr., A., Mulchaey, J. S., et al. 2009, ApJ, 692, 298
Yang, Y., Hammer, F., Flores, H., Puech, M., & Rodrigues, M. 2009, A&A, 501, 437
Younger, J. D., Cox, T. J., Seth, A. C., & Hernquist, L. 2007, ApJ, 670, 269

A&A 615, A26 (2018)

Appendix A: K-correction

In this appendix we represent the K-correction diagrams used to transform between the HST/ACS F606W and F850LP bands and the *B* and *R* rest-frame bands. The K-correction fit results are detailed in Table C.1.

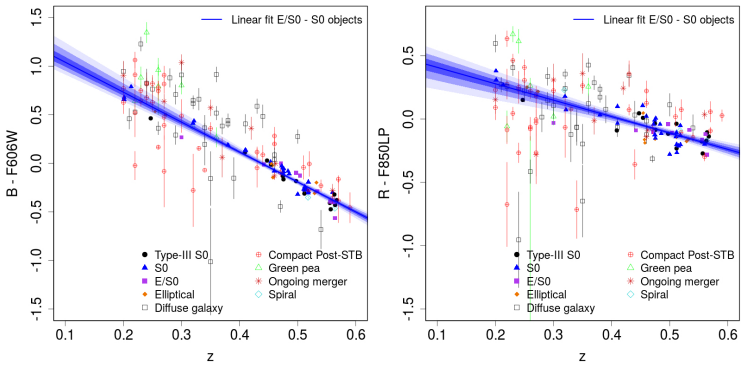

Fig. A.1. *Left panel*: estimated K-correction for the F606W filters to the *B* band as a function of *z*. *Right panel*: estimated K-correction for the F850LP filters to the *R* band as a function of *z*. The linear fit applies to the observed correlation of the S0 and E/S0 galaxies of the sample. The intensity levels of the linear fit represent the 1, 2 and 3σ confidence regions of the fit. We refer to Paper I for more information about the morphological classification of the objects. See the legend in the figure for identification of symbols.

Appendix B: F775W vs. F850LP surface brightness profile parameters

In this appendix we compare the main parameters of the surface brightness profile analysis in the rest-frame *R* band obtained from the F775W and F850LP bands. Fig. B.1 shows that the results obtained from the rest-frame *R*-band profiles obtained from both bands concerning $R_{\rm break}$ and $\mu_{\rm break}$ are quite compatible, with a median dispersion of $\Delta R_{\rm break} \sim 25\%$ and $\Delta\mu_{\rm break} \sim 0.525$ mag arcsec^{-2}.

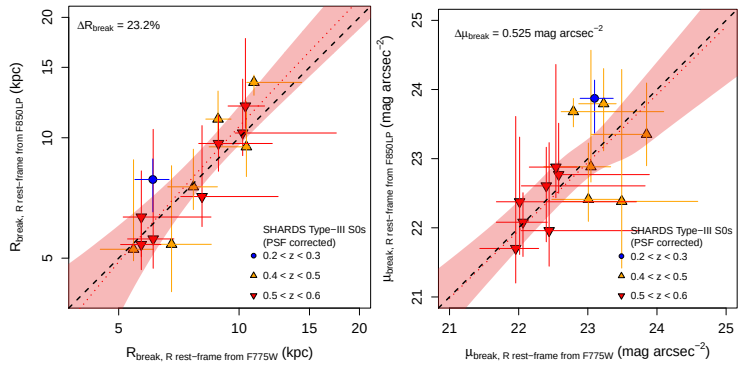

Fig. B.1. *Left panel*: $R_{\rm break}$ measured in the F850LP profile as a function of the $R_{\rm break}$ measured in the F775W profile, both after correction to the rest-frame *R*-band. *Right panel:* $\mu_{\rm break}$ measured in the F850LP profile as a function of the $\mu_{\rm break}$ obtained from the F775W profile, both after correction to the rest-frame *R*-band. The dashed black line represents the values that the parameters should have if they were identical. The red dotted line is the linear fit performed to the data in each panel. The colour contour of the linear fit represents the 1σ confidence region of the fit. We refer to Paper I for more information about the morphological classification of the objects. Consult the legend in the figure.

Appendix C: Linear fits to the trends in structural, photometric, and stellar mass planes of Type-III S0–E/S0 galaxies at $z = 0$ and $0.4 < z < 0.6$

Table C.1. Linear fits to the trends in several photometric planes of Type-III S0–E/S0 galaxies at $z = 0$ and $0.4 < z < 0.6$, to the K-corrections for the F606W and F850LP filters, and to the trends of the anti-truncation parameters with the logarithm of the stellar mass.

		Type-III S0s at $0.4 < z < 0.6$				Local Universe Type-III S0s			
No. (1)	Photometric relation (2)	a (3)	b (4)	$\rho_{\rm Spearman}$ (5)	p-value (6)	a (7)	b (8)	$\rho_{\rm Spearman}$ (9)	p-value (10)
1	$\log_{10}(h_{\rm i})$ vs. $\log_{10}(R_{\rm break})$	$0.990^{+0.108}_{-0.095}$	$-0.618^{+0.091}_{-0.100}$	0.835	$< 10^{-5}$	$0.852^{+0.142}_{-0.115}$	$-0.50^{+0.11}_{-0.13}$	0.866	$< 10^{-5}$
2	$\log_{10}(h_{\rm o})$ vs. $\log_{10}(R_{\rm break})$	$1.56^{+0.71}_{-0.32}$	$-0.81^{+0.28}_{-0.60}$	0.841	$3 \cdot 10^{-5}$	$1.35^{+0.25}_{-0.25}$	$-0.57^{+0.21}_{-0.23}$	0.809	$5 \cdot 10^{-5}$
3	$\mu_{0,\rm i}$ vs. $\log_{10}(R_{\rm break})$	$3.5^{+1.0}_{-1.3}$	$15.19^{+1.21}_{-0.99}$	0.269	0.085	$3.51^{+0.82}_{-0.61}$	$16.32^{+0.57}_{-0.73}$	0.676	0.001
4	$\mu_{0,\rm o}$ vs. $\log_{10}(R_{\rm break})$	$9.6^{+6.6}_{-3.3}$	$12.3^{+2.8}_{-5.6}$	0.582	$3.7 \cdot 10^{-3}$	$6.1^{+1.1}_{-1.5}$	$16.56^{+1.10}_{-0.96}$	0.723	$2.1 \cdot 10^{-3}$
5	$\mu_{\rm break}$ vs. $\log_{10}(R_{\rm break})$	$5.13^{+0.75}_{-0.70}$	$18.19^{+0.62}_{-0.67}$	0.626	$8.9 \cdot 10^{-4}$	$5.27^{+0.48}_{-0.64}$	$19.33^{+0.65}_{-0.42}$	0.702	$8.8 \cdot 10^{-3}$
6	$\log_{10}(h_{\rm i}/R_{23})$ vs. $\log_{10}(R_{\rm break}/R_{23})$	$0.90^{+0.13}_{-0.12}$	$-0.629^{+0.014}_{-0.012}$	0.670	$9 \cdot 10^{-4}$	$0.66^{+0.17}_{-0.12}$	$-0.602^{+0.022}_{-0.025}$	0.816	$4 \cdot 10^{-5}$
7	$\log_{10}(h_{\rm o}/R_{23})$ vs. $\log_{10}(R_{\rm break}/R_{23})$	$1.82^{+1.04}_{-0.48}$	$-0.276^{+0.080}_{-0.047}$	0.769	$6.7 \cdot 10^{-4}$	$1.29^{+0.35}_{-0.27}$	$-0.296^{+0.054}_{-0.057}$	0.429	0.059
8	$\mu_{0,\rm i}$ vs. $\log_{10}(R_{\rm break}/R_{23})$	$5.5^{+1.5}_{-2.1}$	$18.484^{+0.108}_{-0.089}$	0.456	0.03	$4.056^{+1.58}_{-0.94}$	$19.066^{+0.20}_{-0.23}$	0.651	$8 \cdot 10^{-4}$
9	$\mu_{0,\rm o}$ vs. $\log_{10}(R_{\rm break}/R_{23})$	$14.9^{+10.8}_{-4.7}$	$21.45^{+0.72}_{-0.40}$	0.835	$9 \cdot 10^{-5}$	$7.5^{+2.2}_{-2.2}$	$21.30^{+0.30}_{-0.33}$	0.598	0.018
10	$\mu_{\rm break}$ vs. $\log_{10}(R_{\rm break}/R_{23})$	$7.74^{+0.56}_{-0.56}$	$23.086^{+0.057}_{-0.058}$	0.967	$< 10^{-5}$	$7.01^{+0.55}_{-0.38}$	$23.468^{+0.087}_{-0.092}$	0.968	$< 10^{-5}$
11	B - F606W vs. z	$-3.08^{+0.14}_{-0.12}$	$1.350^{+0.059}_{-0.069}$	-0.962	$< 10^{-5}$	–	–	–	–
12	R - F850LP vs. z	$-1.30^{+0.11}_{-0.12}$	$0.639^{+0.060}_{-0.052}$	0.799	$< 10^{-5}$	–	–	–	–
13	$R_{\rm break}$ vs. $\log_{10}(M/M_\odot)$	$3.5^{+2.6}_{-6.2}$	-29^{+66}_{-28}	0.252	0.257	$9.2^{+4.9}_{-4.0}$	-88^{+41}_{-51}	0.513	$2.8 \cdot 10^{-2}$
14	$h_{\rm i}$ vs. $\log_{10}(M/M_\odot)$	$1.04^{+0.33}_{-2.7}$	$-9.2^{+29.0}_{-3.4}$	0.234	0.247	$1.99^{+0.53}_{-0.43}$	$-18.9^{+4.6}_{-5.5}$	0.633	$8.3 \cdot 10^{-3}$
15	$h_{\rm o}$ vs. $\log_{10}(M/M_\odot)$	$1.4^{+2.9}_{-4.7}$	-10^{+50}_{-31}	0.125	0.370	$11.5^{+8.6}_{-6.6}$	-115^{+68}_{-89}	0.746	$3.8 \cdot 10^{-3}$
16	$h_{\rm o}/h_{\rm i}$ vs. $\log_{10}(M/M_\odot)$	$-0.87^{+2.40}_{-0.59}$	$11.34^{+6.5}_{-25.6}$	-0.073	0.433	$3.6^{+2.5}_{-2.3}$	-35^{+24}_{-25}	0.347	0.148
17	$\mu_{\rm break}$ vs. $\log_{10}(M/M_\odot)$	$-1.64^{+0.59}_{-0.83}$	$40.4^{+8.9}_{-6.2}$	-0.373	0.161	$3.17^{+1.75}_{-1.63}$	$-9.2^{+17.2}_{-18.3}$	0.384	0.127
18	$\mu_{0,\rm i}$ vs. $\log_{10}(M/M_\odot)$	$-1.78^{+0.47}_{-0.58}$	$37.3^{+6.3}_{-5.1}$	-0.546	$3.6 \cdot 10^{-2}$	$2.05^{+0.70}_{-0.56}$	$-1.9^{+5.9}_{-7.2}$	0.493	$3.9 \cdot 10^{-2}$
19	$\mu_{0,\rm o}$ vs. $\log_{10}(M/M_\odot)$	$-1.3^{+3.2}_{-1.1}$	35^{+11}_{-34}	-0.204	0.311	$4.4^{+1.9}_{-1.7}$	-24^{+17}_{-19}	0.456	0.102

Notes: Columns: (1) ID number of the relation. (2) Fitted relation. (3) Slope of the linear fit to the Type-III S0 galaxies at $0.4 < z < 0.6$. (4) Y-intercept of the linear fit to the Type-III S0 galaxies at $0.4 < z < 0.6$. (5) Spearman ρ correlation test statistic for the Type-III S0 galaxies at $0.4 < z < 0.6$. (6) Spearman correlation test p-value for the Type-III S0 galaxies at $0.4 < z < 0.6$. (7–10) The same as columns 3–6, but for the linear fits performed to the local samples.

A&A 615, A26 (2018)

Appendix D: Surface brightness and colour profiles

Here we represent the surface brightness and colour profiles of the Type-III S0 and E/S0 objects within our sample, accounting for their PSF-corrected photometric profiles.

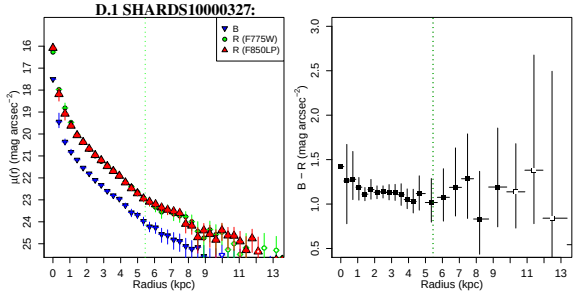

Fig. D.1. *Left panel*: surface brightness profiles corrected for dust extinction, cosmological dimming and K-correction to the rest-frame FORS *B* band and the Steidel *R* band. We represent the *R* band profile calculated with both F775W and the F850LP HST/ACS bands (green and red, see the legend for details). *Right panel*: $(B - R)$ colour profile corrected for dust extinction, cosmological dimming and K-correction to the rest-frame FORS *B* band and the Steidel *R* band. Filled symbols present a probability higher than 99.5% to be over the sky-level. In the case of colour profiles, the limiting radius corresponds to the lower radius of the limiting magnitudes of the *B* and *R* bands. The vertical green dotted line represents the break radius $R_{\rm break}$ for the F775W band (see Paper I).

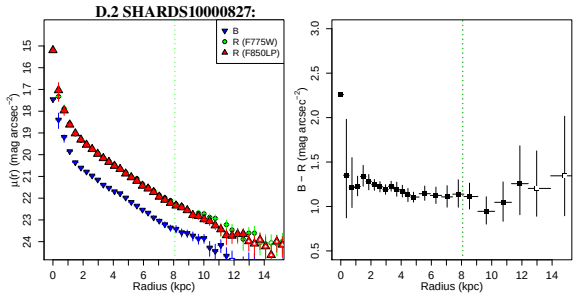

Fig. D.2. See caption of Fig. D.1.

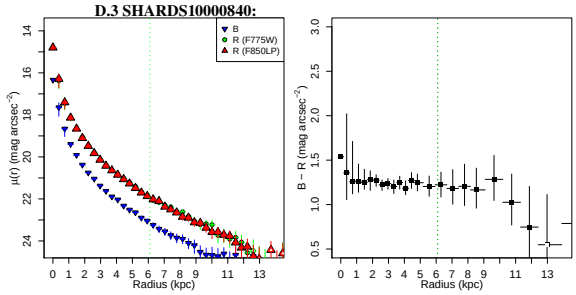

Fig. D.3. See caption of Fig. D.1.

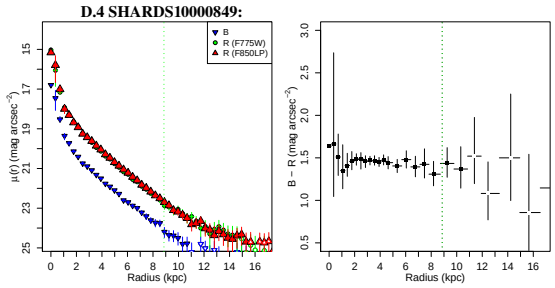

Fig. D.4. See caption of Fig. D.1.

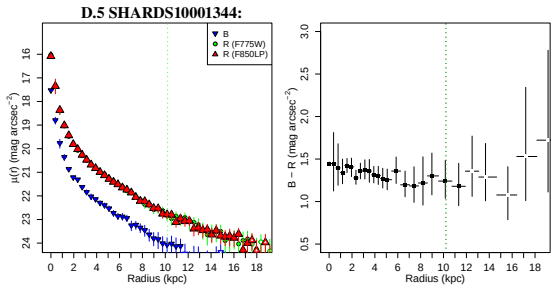

Fig. D.5. See caption of Fig. D.1.

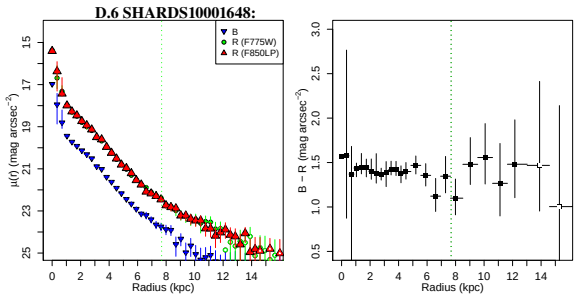

Fig. D.6. See caption of Fig. D.1.

A&A 615, A26 (2018)

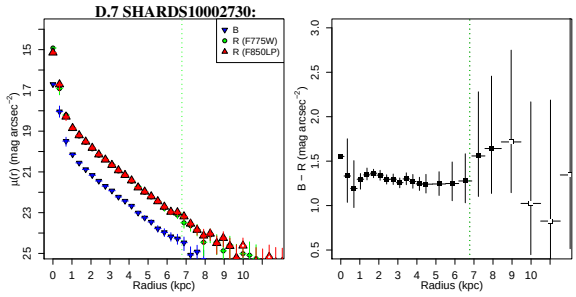

Fig. D.7. See caption of Fig. D.1.

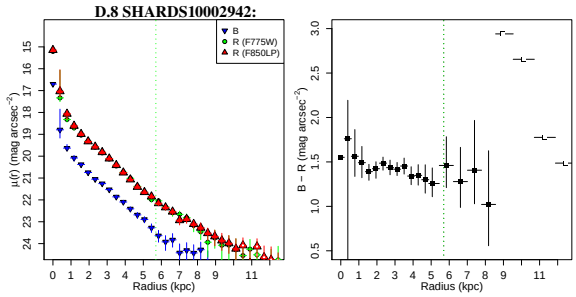

Fig. D.8. See caption of Fig. D.1.

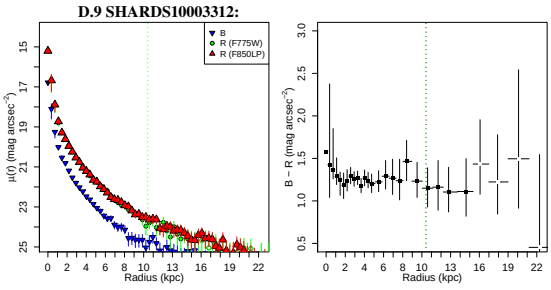

Fig. D.9. See caption of Fig. D.1.

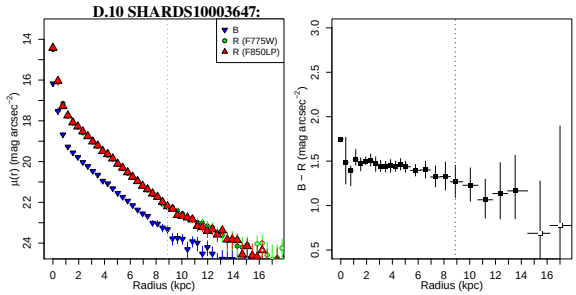

Fig. D.10. See caption of Fig. D.1.

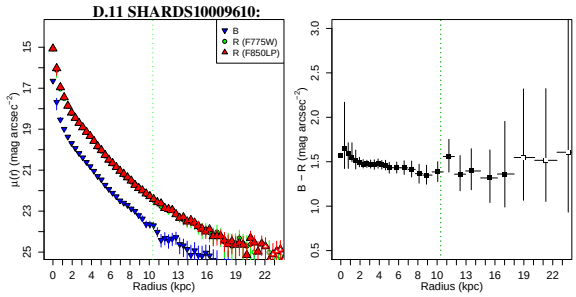

Fig. D.11. See caption of Fig. D.1.

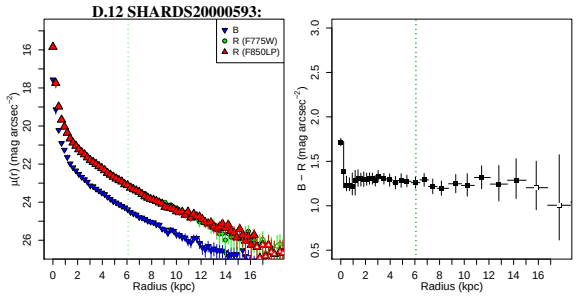

Fig. D.12. See caption of Fig. D.1.

A&A 615, A26 (2018)

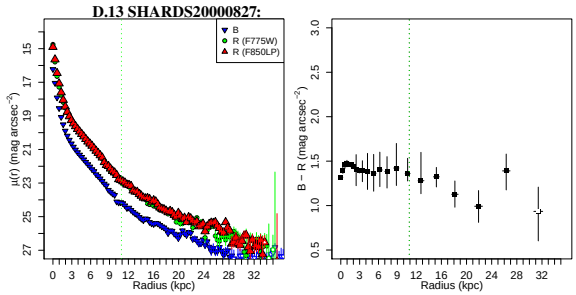

Fig. D.13. See caption of Fig. D.1.

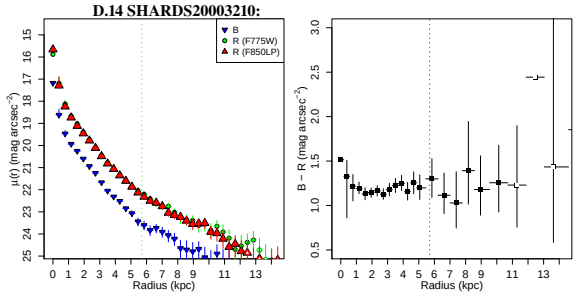

Fig. D.14. See caption of Fig. D.1.

5

The missing light of the Hubble Ultra Deep Field

The most terrifying fact about the Universe is not that it is hostile but that it is indifferent. [...] However vast the darkness, we must supply our own light.

— Stanley Kubrick

In the fifth chapter of this PhD thesis we focus on obtaining accurate imaging data to analyse the surface brightness profiles of galaxies beyond $z \sim 0.6$. As explained in Section 1.5 of Chapter 1, deep imaging is not only necessary to study the dimmest parts of local galaxies, but because of the cosmological dimming (Tolman 1930, 1934, see Fig. 1.9), it is critical if we want to study the evolution of such structures at high-z. Moreover, NIR observations become necessary to study the structures at rest-frame wavelengths similar to those observed in the local Universe. As a consequence of this, there is an increasing need for space-based observations and the improvement of NIR reduction techniques.

The Hubble Ultra Deep Field (HUDF, α=3h 32m 39.0s, $\delta = -27;47;29.1$, J2000, Beckwith et al. 2006) is the deepest cosmological field ever observed. With more than 220 hours of observation time based on the observations of HUDF09 (Bouwens et al. 2011), HUDF12 (Koekemoer et al. 2012) and the XDF projects (Illingworth et al. 2013) in four bands of the WFC3/IR instrument (F105W, F125W, F140W, and F160W), and a considerable number of photometric and spectroscopic follow-up observations from gamma-rays to radio, it allows us in principle to study the surface brightness profile of galaxies down to $\mu_{lim} \sim 31$ mag arcsec^{-2} (Buitrago et al. 2017), and is therefore the ideal field to continue the analysis presented in the previous chapters of this PhD thesis towards higher-z ranges.

However, the primary objective of the HST observations on the HUDF was the study of high-z galaxies (up to $z \sim 9-10$). Such objects present very small angular sizes and are usually unresolved even in space-based high-resolution observations. In addition, the presence of artificial gradients due to flat-field residuals and sky background contamination forced the observers to fit and remove two-dimensional sky background gradients in order to avoid residuals in the final mosaics. Although this is a valid technique to prevent biases in the analysis of small angular size objects, it can fit and oversubtract the outskirts of the largest galaxies in the field, destroying any signatures of low surface brightness structures at high galactocentric radii. This effect is specially visible around the outskirts of objects with the largest angular sizes in the XDF (Illingworth et al. 2013), which are usually surrounded of a valley of negative flux relative to the sky background level.

Due to this, Buitrago et al. (2017) used the mosaics of the HUDF12 version of the WFC3/IR HUDF instead of the XDF for the study of the stellar halos at $z \sim 0.6-1$, despite the fact that the HUDF12 mosaics did not include all the available data. However, we will demonstrate that the HUDF12 mosaics are also significantly affected by sky over-subtraction. Therefore, none of the currently available reductions of the WFC3/IR HUDF is suitable for the study of the low surface brightness limits of the objects at $z \sim 1$, because no single reduction simultaneously includes all the available data and carefully preserves the properties of the low surface brightness limits. It is for this reason that we focus the last part of this PhD thesis on the creation of a dedicated version of the WFC3/IR HUDF mosaics for the study of extended low surface brightness features. In order to do that, we focused on four major points: 1) the creation of an accurate sky flat-field for each filter using images of the same epoch, 2) dedicated analysis of the persistence effects in the detector, 3) careful sky-subtraction, correction of the time-dependent sky-background and final residual gradients removal, and 4) robust combination of the individual exposures and estimation of the uncertainties of the final mosaics. We made the final mosaics publicly available in the web page of the project, for the benefit of all the scientific community[1].

The work presented in this Chapter was submitted to *Astronomy & Astrophysics*, the 24th of September of 2018, under the title **"The missing light of the Hubble Ultra Deep Field"**.

[1] ABYSS Hubble Ultra Deep Field is available at http://www.iac.es/proyecto/abyss/

Astronomy & Astrophysics manuscript no. output
September 25, 2018

The missing light of the Hubble Ultra Deep Field

Alejandro Borlaff[1,2], Ignacio Trujillo[1,2], Javier Román[1,2], John E. Beckman[1,2,3], M. Carmen Eliche-Moral[1], Raúl Infante-Saínz[1,2], Alejandro Lumbreras[1,2], Rodrigo Takuro Sato Martín de Almagro[4], Carlos Gómez-Guijarro[5], María Cebrián[1,2], Antonio Dorta[1,2], Nicolás Cardiel[6], Mohammad Akhlaghi[7], Cristina Martínez-Lombilla[1,2]

[1] Instituto de Astrofísica de Canarias, C/ Vía Láctea, E-38200 La Laguna, Tenerife, Spain
e-mail: asborlaff@iac.es
[2] Facultad de Física, Universidad de La Laguna, Avda. Astrofísico Fco. Sánchez s/n, 38200, La Laguna, Tenerife, Spain
[3] Consejo Superior de Investigaciones Científicas, Spain
[4] Instituto de Ciencias Matemáticas, Consejo Superior de Investigaciones Científicas, Madrid, Spain
[5] Cosmic Dawn Center (DAWN), Niels Bohr Institute, University of Copenhagen, Copenhagen, Denmark
[6] Departamento de Astrofísica y CC. de la Atmósfera, Universidad Complutense de Madrid, E-28040 Madrid, Spain
[7] Univ. Lyon, Univ. Lyon1, ENS de Lyon, CNRS, Centre de Recherche Astrophysique de Lyon UMR5574, 69230 Saint-Genis-Laval, France

September 25, 2018

ABSTRACT

Context. The Hubble Ultra Deep field (HUDF) is the deepest region ever observed with the *Hubble Space Telescope*. With the main objective of unveiling the nature of galaxies up to $z \sim 7-8$, the observing and reduction strategy have focused on the properties of small and unresolved objects, rather than the outskirts of the largest objects, which are usually over-subtracted.
Aims. We aim to create a new set of WFC3/IR mosaics of the HUDF using novel techniques to preserve the properties of the low surface brightness regions.
Methods. We created ABYSS: a pipeline that optimises the estimate and modelling of low-level systematic effects to obtain a robust background subtraction. We have improved four key points in the reduction: 1) creation of new absolute sky flat fields, 2) extended persistence models, 3) dedicated sky background subtraction and 4) robust co-adding.
Results. The new mosaics successfully recover the low surface brightness structure removed on the previous HUDF published reductions. The amount of light recovered with a mean surface brightness dimmer than $\overline{\mu} = 26$ mag arcsec^{-2} is equivalent to a $m = 19$ mag source when compared to the XDF and a $m = 20$ mag compared to the HUDF12.
Conclusions. We present a set of techniques to reduce ultra-deep images ($\mu > 32.5$ mag arcsec^{-2}, 3σ in 10×10 arcsec boxes), that successfully allow to detect the low surface brightness structure of extended sources on ultra deep surveys. The developed procedures are applicable to HST, JWST, EUCLID and many other space and ground-based observatories. We made the final ABYSS WFC3/IR HUDF mosaics publicly available for the benefit of the astronomical community.

Key words. Techniques: image processing, techniques: photometric, methods: observational, galaxies: evolution, galaxies: structure, galaxies: high-redshift

1. Introduction

The Hubble Ultra Deep field is a 11 arcmin^2 region of the sky located in the Southern hemisphere (α=3h 32m 39.0s, δ = −27°47′29.1″, J2000), in the Fornax Constellation. Included inside the Chandra Deep Field South (Giacconi et al. 2002) and the GOODS-South Field (Giavalisco et al. 2003), it was observed by Beckwith et al. (2006) during 10^6s of the Hubble Space Telescope Director's Discretionary Time with the Advanced Camera for Surveys (ACS), becoming the deepest image of the sky ever obtained. The authors divided the exposure time between the available filters (F435W, F606W, F775W and F850LP) with the main objective of creating a robust sample of galaxies between $4 < z < 7$ by using the Lyman break dropout method (Steidel & Hamilton 1992; Steidel et al. 1996a,b).

Since then, an increasingly number of follow up projects with different telescopes has continued the observations of this field, including observation at radio wavelengths (VLA, Rujopakarn et al. 2016; ALMA, Dunlop et al. 2016; Aravena et al. 2016a,b; Walter et al. 2016), in the infrared (Spitzer/IRAC, Labbe et al. 2015), optical and near-infrared (near IR) spectroscopy (VLT/MUSE, Bacon et al. 2017), ultraviolet (WFC3/UVIS, Teplitz et al. 2013), and X-rays (Chandra, Xue et al. 2011; Luo et al. 2016; XMM-Newton, Comastri et al. 2011). In addition to these, the replacement in 2009 of the Wide Field and Planetary Camera 2 by the Wide Field Camera 3 (WFC3) during the Hubble Space Telescope Servicing Mission 4 (STS-125) allowed astronomers to continue the exploration of this field with a deep, high-resolution survey in near IR. With the main objective of finding the earliest sources in the Universe, HUDF09 (Oesch et al. 2009; Bouwens et al. 2009) and the Hubble Ultra Deep Field 2012 (HUDF12 hereafter, Koekemoer et al. 2012) have increased the number of filters and exposure time in the HUDF. In addition, the eXtreme deep field (XDF hereafter, Illingworth et al. 2013), reprocessed all the HST/ACS and WFC3/IR available data in the HUDF. The addition of four new bands in WFC3/IR (F105W, F125W, F140W and F160W) has permitted the detection of galaxies out to $z \sim 9-10$. Additionally, the extraordinary depth of the HUDF12 allows the study

A&A proofs: manuscript no. output

of galaxy stellar halos with surface brightness profiles down to $\mu_{lim} \sim 31$ mag arcsec^{-2} (Buitrago et al. 2016).

Detecting extended sources in the low-surface brightness regime is an extremely challenging task. Systematic effects such as sky background, persistence, or the PSF may dominate the light distribution of the science images. Aggressive sky background subtraction may be a tempting solution to get rid of the diffuse light, whether it is caused by real astronomical sources or by artificial sky background gradients. Nevertheless, such approach have a major setback. It removes the possibility of using the sciences mosaics to study the outskirts of the largest objects, distorting the photometry of the structures up to $2-3$ mag arcsec^{-2} brighter than the limiting magnitude. Due to this, is common to find over-subtracted zones with negative fluxes around large galaxies in the majority of the surveys (i.e, see the Hyper Suprime-Cam survey[1], Aihara et al. 2018). It is for this reason that careful sky-subtraction is a crucial step to preserve the properties of the low-surface brightness features of extended sources. This effect is clearly visible around the largest objects of the XDF mosaics (Illingworth et al. 2013). We must note that the main objective of the XDF project was not the study of the stellar haloes of the nearest galaxies of the HUDF ($z < 1$) but to identify unresolved sources across a redshift range from $z \sim 4$ to $z \sim 12$ with aperture photometry. Nonetheless, the over subtraction of the diffuse outskirts of nearby galaxies (which cover a large fraction of the total field-of-view) can significantly affect the photometry of the background high-z objects.

In order to overcome the increasing challenge of studying the low surface brightness Universe, a number of recent observational studies has shown the way to reach and surpass the frontier of $\mu_{lim} \sim$ 30 mag arcsec^{-2} (see Trujillo & Fliri 2016). The variety of systematic problems that significantly affect the background level of the images depends on the required imaging depth, such as fringing (Wong 2010), ghosts (Yang et al. 2002), gain differences between chip amplifiers, scattered light (Fowler et al. 2017) and even the effect of the point-spread function (PSF, Sandin 2014, 2015). As a consequence of this, the use of robust statistical tools for the study of the outskirts of galaxies is mandatory for these scientific objectives.

The low surface brightness Universe is one of the key fields for cosmology and to unveil the origin and evolution of galaxies. In particular, the processes that give rise to the galaxy discs are not completely clear. Apparent exponential discs (Type-I) on first inspection may on closer examination suffer from a number of deviations such as truncations and down-bending profiles (Type-II) or the opposite phenomenon: anti-truncations (Type-III discs, Erwin et al. 2005; Pohlen & Trujillo 2006; Erwin et al. 2007; Gutierrez et al. 2011). There are various scenarios which entail a variety of possible mechanisms probing the variety of galactic discs, such as different types of mergers and gravitational interactions (Laurikainen & Salo 2001; Penarrubia et al. 2006; Younger et al. 2007; Kazantzidis et al. 2009; Borlaff et al. 2014), internal and stellar formation related processes (Roškar et al. 2007; Herpich et al. 2015a,b; Elmegreen & Struck 2016; Struck & Elmegreen 2016, 2017) or the presence of different components on the structure of disc galaxies (Comerón et al. 2012; Comerón et al. 2014). Until now, there have been few studies that have tried to study the detailed shape of galaxy discs along significant cosmological times (Azzollini et al. 2008a,b; Trujillo & Bakos 2013; Maltby et al. 2014; Borlaff et al. 2017; Borlaff et al. 2018). The main reason for this is that PSF-effects and cosmological dimming make difficult to study the outskirts of galaxies at increasing redshifts, where these effects become critical (Sandin 2014, 2015; Trujillo & Fliri 2016; Borlaff et al. 2017). Moreover, while near IR imaging allows us to explore higher z ranges, it includes additional problems such as the high sky background variability or persistence effects, which may contaminate the science images. Consequently, there is an increasing need for very deep observations and surveys as redshift increases.

The outskirts of some nearest galaxies show traces of their formation mechanisms, such as tidal tails, haloes, plumes and satellites. Simulation-based studies predict that a hypothetical survey with a limiting magnitude fainter than ~ 30 mag arcsec^{-2} would detect up to a dozen of accretion features around Milky Way-type galaxies (Johnston et al. 2008; Cooper et al. 2009). Apparently isolated galaxies show large tidal tails, warped discs and other asymmetric features in sufficiently deep images, as well as large numbers of satellites (Schweizer & Seitzer 1990; Martinez-Delgado et al. 2008b,a; Chonis et al. 2011). In fact, volume-limited samples of nearby galaxies detect that almost 14% of the galaxies present diffuse features compatible with minor merger events at a limiting magnitude of 28 mag arcsec^{-2} (Morales et al. 2018). An increasing number of low surface brightness explorations have been performed on individual galaxies and deep fields, but there is an increasing need for telescope-dedicated large-scale low surface brightness surveys (Horton et al. 2016; Valls-Gabaud & Collaboration 2016, see The Australian Space Eye and The MESSIER surveyor). Direct imaging of the stellar haloes and their structure is one of the major test for ΛCDM scenario of galaxy formation (Abadi et al. 2005; Bullock & Johnston 2005). Although the study of the streams of the stellar haloes has been tested for a limited sample of galaxies in the Local Group using star counts (Ibata et al. 2009; McConnachie et al. 2009; Tanaka et al. 2011; Ibata et al. 2013; Peacock et al. 2014), this method is limited to a maximum distance of 16 Mpc with HST (Zackrisson et al. 2012).

It is for these reasons that the main objective for this paper is to explore the capabilities of HST performing a specific reduction that intends to optimise the limiting depth around extended objects and pave the way for the exploration of the outskirts of galaxies, discs, satellites, tidal streams and their stellar haloes. The proposed techniques are directly applicable to its successor in the infrared – the James Webb Space Telescope (JWST) – and similar missions such as EUCLID, for deep integrated photometry of extended sources beyond the Local Universe.

The paper is structured as follows. The full methodology used for the reduction is described in detail in Sect. 2. The results are presented and discussed in Sect. 3. The final conclusions can be found in Sect. 4. We assume a concordance cosmology ($\Omega_M = 0.3, \Omega_\Lambda = 0.7, H_0 = 70$ km s^{-1} Mpc^{-1}, see Spergel et al. 2006). All magnitudes are in the AB system (Oke 1971) unless otherwise noted.

2. Methods

In this section we provide an outline of the reduction process that we have followed to create a version of the HUDF WFC3/IR mosaics optimized for the study of the low surface brightness Universe (the ABYSS[2] pipeline, hereafter). The full process (represented in the flowchart of Fig. 1) can be divided into three main branches:

[1] Hyper Suprime-Cam Subaru Data Release 1: https://hsc-release.mtk.nao.ac.jp/doc/index.php/known-problems-in-dr1/

[2] ABYSS: a low surface brightness dedicated reduction for the HUDF WFC3/IR mosaics: http://www.iac.es/proyecto/abyss/